A framework for polydisperse pulp phase modelling in flotation

Gaurav Bhutani[a,b,c,*], Pablo R. Brito-Parada[b,c]

[a]*Multiphase Flow Research Lab, School of Engineering, Indian Institute of Technology Mandi, Kamand 175005, India*
[b]*Advanced Mineral Processing Research Group, Department of Earth Science and Engineering, Imperial College London, South Kensington Campus, London SW7 2AZ, United Kingdom*
[c]*Applied Modelling and Computation Group, Department of Earth Science and Engineering, Imperial College London, South Kensington Campus, London SW7 2AZ, United Kingdom*

Abstract

Froth flotation is one of the most widely-used mineral processing operations. The pulp zone in flotation tanks is polydisperse in general and serves as a medium for the interaction between the solid particles and the gas bubbles in a liquid continuum, leading to particle–bubble attachment/detachment and bubble coalescence/breakage phenomena. To better predict the hydrodynamics and inform the design of efficient flotation equipment, it is therefore important to accurately model and simulate the evolution of the size distribution of the dispersed phases. This has created an urgent need for a framework that can model the pulp phase in an efficient manner, which is not currently available in the literature. The available software products are not efficient enough to allow for a tractable modelling of industrial-scale flotation cells and in some cases they cannot model the polydispersity of the dispersed phase at all. This work presents an efficient numerical framework for the macroscale simulation of the polydisperse pulp phase in froth flotation in an open-source finite element computational fluid dynamics (CFD) code that provides an efficient solution method using mesh adaptivity and code parallelisation. A (hybrid finite element–control volume) finite element framework for modelling the pulp phase has been presented for the first time in this work. An Eulerian–Eulerian turbulent flow model was implemented in this work including a transport equation for attached and free solid particles. Special care was taken to model the settling velocity of the free solids and the modification of the liquid viscosity due to the presence of these particles. Bubble polydispersity was modelled using the population balance equation (PBE), which was solved using the direct quadrature method of moments (DQMOM). Appropriate functions for bubble coalescence and breakage were chosen in the PBE. Mesh adaptivity was applied to the current problem to produce fully-unstructured anisotropic meshes, which improved the solution efficiency, while all simulations were executed on a multicore architecture. The model was validated for 2D simulations of a bubble column against experimental results available in the literature. After successful validation, the model was applied to the simulation of the pulp phase in a flotation column for monodisperse and polydisperse solids. Polydispersity of the solids was modelled for the first time in this work using three separate solid size classes. A clear dependence of the flotation rate on the particle size was noticed and the monodisperse solids simulations were shown to over-predict the flotation rate. Other than flotation, this open-source framework can be used for the simulation of a variety of polydisperse multiphase flow problems in the process industry.

Keywords: CFD, mesh adaptivity, polydisperse flow, population balance modelling, pulp phase

1. Introduction

Froth flotation is one of the most widely used mineral processing operations, used to selectively separate the valuable mineral particles from the unwanted waste particles. Other than mineral processing, flotation is also used for deinking in wastepaper recycling, wastewater treatment, and oil separation applications. Air is injected into a tank containing a slurry of crushed ore; and mixing generated in the pulp zone causes the hydrophobic mineral particles to collide and attach to the air bubbles that rise to the top into the froth zone, which overflows as concentrate. The pulp zone in flotation is a multi-scale, turbulent, three-phase, and polydisperse system that serves as a medium for the interaction between the solid particles and the gas bubbles in a liquid continuum. It is therefore important to accurately model the physics (particularly the hydrodynamics) in the pulp zone for the development of efficient flotation equipment.

Computational fluid dynamics (CFD) has emerged as a popular technique for the numerical modelling and simulation of multiphase flow systems. This can be attributed to continuous improvements in computational power and development of improved numerical algorithms for the modelling of multiphase flows. CFD therefore offers a promising possibility for the modelling of the complex physics occurring in the pulp zone in froth flotation. The pulp physics, however, are considerably challenging compared to the typical multiphase flow systems discussed in the literature, and the available CFD software products either cannot handle all the above complexi-

*Corresponding author
Email addresses: gaurav@iitmandi.ac.in (Gaurav Bhutani), p.brito-parada@imperial.ac.uk (Pablo R. Brito-Parada)

ties or are not tractable enough to allow for the modelling of industrial-scale flotation devices. An efficient CFD framework that can model the hydrodynamics in the pulp phase is therefore needed.

Gaudin (1932) and Garcia-Zuñiga (1935) were the first to study the effect of flow properties on flotation recovery, realising the importance of the hydrodynamics in the pulp zone on flotation. The flotation recovery was found to be sensitive to flow parameters and the need to understand the physics of the processes occurring in the pulp zone was identified. There have been studies that model the hydrodynamics of the pulp phase in froth flotation (Bloom and Heindel, 2002, 2003), however Koh et al. (2000) were the first to simulate the pulp phase in a flotation tank using CFD modelling. Consistently improving their pulp phase models over time (Koh and Schwarz, 2003, 2006, 2007), the above researchers were able to model the fluids (liquid and gas) using two-phase unsteady flow equations and the solids using separate transport equations for free and attached particles. Please note that 'particles' in this paper refers to the solid particles, unless clarified otherwise. The Eulerian–Eulerian (E–E) method coupled to the k-ε turbulence model was used for modelling the fluid phases, and the equations were solved using the CFX-4 code for a fixed bubble size. Karimi et al. (2014a) and Karimi et al. (2014b) solved a similar pulp phase model in ANSYS Fluent.

The importance of including a good estimate for the bubble size distribution (BSD) in the models for pulp hydrodynamcs has been known (Gorain et al., 1995; Grevskott et al., 1996), and Evans et al. (2008) and Koh and Schwarz (2008b) were the first to include the population balance equation (PBE), which models the effects of bubble coalescence and breakage, for modelling the BSD in a flotation pulp. The method of classes (CM) implementation of ANSYS was used to solve the PBE in the CFX software in both studies, and the latter reported a significant effect of modelling the BSD on the flotation rate prediction. Others have also used the CM to model the BSD in flotation systems (Basavarajappa et al., 2017; Sarhan et al., 2017, 2018). Recently, Schwarz et al. (2016) have summarised the importance of the need of more efficient methods—the quadrature-based moment methods (QBMMs)—for solving the PBE in the flotation pulp, since these methods are computationally economical than their counterparts. The use of quadrature method of moments (QMOM), a type of QBMM, to solve the PBE for modelling the BSD in a flotation cell geometry has been reported in the literature recently (Basavarajappa and Miskovic, 2015), however this work considered gas-liquid flows only (without solids).

QBMMs, such as QMOM and direct quadrature method of moments (DQMOM), have proven to be very efficient when coupled to the E–E fluid flow equations for modelling industrial-scale polydisperse multiphase systems (Marchisio et al., 2003b). Although there are a few studies available that model the pulp phase containing a model for the BSD evolution as discussed above, there is a need for a framework that allows for the modelling of the BSD using a QBMM in the pulp phase. Sarhan et al. (2016, 2017, 2018) have recently proposed a CM-based pulp phase modelling framework that models all three phases as Eulerian phases and handles one class of solid particles. Additionally, the solids feed entering the flotation tank is in the form of a particle size distribution and the framework should also be able to consider this polydispersity of the solids for an accurate modelling of the overall process. Current literature is confined to models that deal with monodisperse solids in the pulp and there remains a need for a framework that can model the polydispersity of the solids in the feed, along with the polydispersity of the gas phase. The overall multiphase turbulent CFD model becomes highly complex when the polydispersity of the dispersed phases is considered. The available software products are not efficient enough to allow for a tractable modelling of industrial scale flotation devices, if at all they can model the polydispersity of the dispersed phases.

To address the above limitations, this work presents an efficient numerical framework for the macroscale simulation of the three-phase polydisperse pulp. This framework, known as Fluidity, is an open-source finite element code that provides an efficient solution method through its fully-unstructured mesh adaptivity feature that can produce highly-anisotropic meshes. Moreover, Fluidity is highly-parallelised, which, along with its other features, makes the solution method highly tractable.

This paper is organised as follows: Section 2 discusses the modelling framework that was developed in this work, including details of the multiphase model equations for the three phases in flotation. Brief details of finite element discretisations and adaptive mesh refinement are also presented in this section. Section 3 describes the flotation problem (geometry and operating conditions) that was solved using the present framework. Section 4 presents model validation for a two-phase bubble column, followed by results for a pulp phase simulation in a flotation column-like geometry. Finally the conclusions and the scope for future work are presented in Section 5.

2. Modelling framework

A set of coupled partial differential equations (PDEs) was used to model the polydisperse pulp phase in this study, and these equations were solved using the adaptive-mesh finite element framework—Fluidity. Fluidity permitted the modelling of the polydisperse phases in an efficient way, which is currently missing in the literature.

Figure 1 shows the complete set of equations and the coupling between them that was used to model the pulp phase inside a flotation column. Separate momentum equations were solved for the air and the liquid (or slurry) phases, assuming the flow to be incompressible (due to low Mach flow). The momentum equations for these two Eulerian phases were coupled to each other through a common pressure field, phase volume fractions and the interphase interaction force, as shown in the figure. In addition, a population balance equation for the air bubbles was

solved to predict the change in the bubble size distribution due to coalescence and breakage processes. The bubble diameter field estimated using the PBE was used for the improved prediction of the interphase interaction force, which depends on the bubble size and can sometimes have a significant effect on the hydrodynamics.

A two-equation k-ε Reynolds-averaged Navier–Stokes (RANS) turbulence model was solved for the turbulent liquid phase. The turbulence kinetic energy (per unit mass), k, and the turbulence dissipation rate (per unit mass), ε, calculated in this turbulence model were used as inputs in the other models such as: the time-averaged liquid phase momentum equation for the calculation of the eddy viscosity, the breakage and coalescence functions in the PBE for air bubbles, and the attachment and detachment terms in the model for solids.

The solid scalar transport equations, coupled to each other through the attachment and detachment source terms, are shown on the left in Figure 1. Although more than one solid class was used in this work, only one has been shown in the figure for illustration. The free (or unattached) solids equations are coupled to the liquid phase momentum equation through the mean (or time-averaged) liquid velocity $\mathbf{U}_c$ and the modified liquid viscosity $\mu_{\text{molecular}}$. The attached solids transport equations are coupled to the gas phase momentum equation through the gas phase velocity field. The PBE supplies the bubble diameter and the bubble concentration for the attachment and detachment rate expressions.

In the present model the bubble size distribution is not affected by attached solids. The breakage and coalescence rate expressions for the bubble population balance equation should ideally include the physics of particle attachment affecting stability of bubbles. The present breakage and coalescence terms only include the liquid phase turbulence, which is affected by the free solids concentration only. Similarly, the gas holdup, which gets modified with the change in bubble size distribution, also doesn't get affected by attached solids in this work. There is no work in the literature that presents an empirical relation for the effect of particle attachment on bubble stability. The effects of adding reagents (collectors, frothers, activators and depressants) in the pulp phase have not been modelled in the present work.

This framework is unique allowing a strong coupling between the different phases (as shown in Figure 1). The highly-parallelised nature of Fluidity along with the ability to handle fully-unstructured adaptive meshes makes it specially suitable to simulate industrial scale flotation pulp. At the present stage there is no other commercial or freely available software product that allows this kind of modelling capability. A detailed description of the modelling equations is presented in the subsections that follow.

2.1. Flow equations

An incompressible E–E model was chosen in this work over the other options available—mixture model and Eulerian–Lagrangian model—as it provides a good balance between accuracy and complexity.

As described in Ishii and Hibiki (2010), the RANS equation for the two phases in this work can be written as:

$$\alpha_i\rho_i\frac{\partial \mathbf{U}_i}{\partial t}+\alpha_i\rho_i\mathbf{U}_i\cdot\nabla\mathbf{U}_i = -\alpha_i\nabla P+\alpha_i\rho_i\mathbf{g}+\nabla\cdot[\alpha_i(\bar{\bar{\tau}}_i+\bar{\bar{\tau}}_i^R)]+\mathbf{f}_i, \quad (1)$$

where the subscript i can be c or d, denoting the continuous (liquid) and the dispersed (gas) phases, respectively. In the above equation, α is the phase volume fraction, ρ is the phase density, $\mathbf{U}$ is the mean phase velocity, P is the mean static pressure, $\mathbf{g}$ is the acceleration due to gravity, $\bar{\bar{\tau}}$ is the mean shear stress tensor, $\bar{\bar{\tau}}^R$ represents the Reynolds stress tensor, and $\mathbf{f}_i$ is the sum of all interphase forces acting on the ith phase due to the other phase.

Ishii and Hibiki (2010) derived the above equation using Reynolds time averaging performed at a point location in space, unlike the usual spatial averaging approach. Their approach defines a phase density function M_i which is equal to one for the phase i and zero otherwise; the volume fraction therefore results from the Reynolds time averaging of M_i at a point location. Weight average of a function F, $\langle wF\rangle/\langle w\rangle$, leads to the definition of *phase average* (weight $w = M_i$) and *mass weighted average* ($w = \rho$). In Equation (1), the mean velocity is a mass-weighted average, and mean pressure and shear stress are phase-averaged quantities. This kind of averaging prevents any statistics of the volume fraction from appearing in the mean equations. The fluctuations in the physical quantities were defined with respect to the above definitions of the mean values. In the present work turbulence was only modelled for the continuous phase and the dispersed phase was considered laminar (same as Pfleger and Becker (2001) and Bhole et al. (2008)), due to the gas phase eddy viscosity 2–3 orders smaller than the liquid phase; i.e. $\mathbf{U}_d = \mathbf{u}_d$ and $\bar{\bar{\tau}}_d^R = 0$ in Equation (1), where $\mathbf{u}$ denotes the actual velocity field.

The mean shear stress term in Equation (1) was modelled as $\bar{\bar{\tau}}_i = \mu_d\left(\nabla\mathbf{U}_i + \nabla(\mathbf{U}_i)^T\right) + \mathbb{D}_{\text{interf}}$, which is obtained from the constitutive equation for an isotropic linear viscous fluid with dynamic viscosity μ_d. $\mathbb{D}_{\text{interf}}$ is the interfacial extra deformation tensor ($\sim \nabla\alpha_c$), also known as the bubble-induced turbulence (BIT) term (Ishii and Hibiki, 2010), which contains the contribution of the bubble wake to the turbulence in the liquid phase. There are two major ways to include the contribution of the bubble wake on liquid velocity fluctuations (and hence the liquid viscous shear stress)—through the inclusion of a modified liquid viscosity (Sato and Sekoguchi, 1975) and through the modification of production terms in turbulence kinetic energy and turbulence dissipation rate equations (Pfleger and Becker, 2001; Bannari et al., 2008). The literature contains works comparing the two approaches and there is no consensus on the superiority of one model over the other. While a few prefer the use of modified viscosity (Pfleger et al., 1999; Ojima et al., 2014), many found the use of modified production better (Olmos et al., 2003), and a few simply found the inclusion of BIT

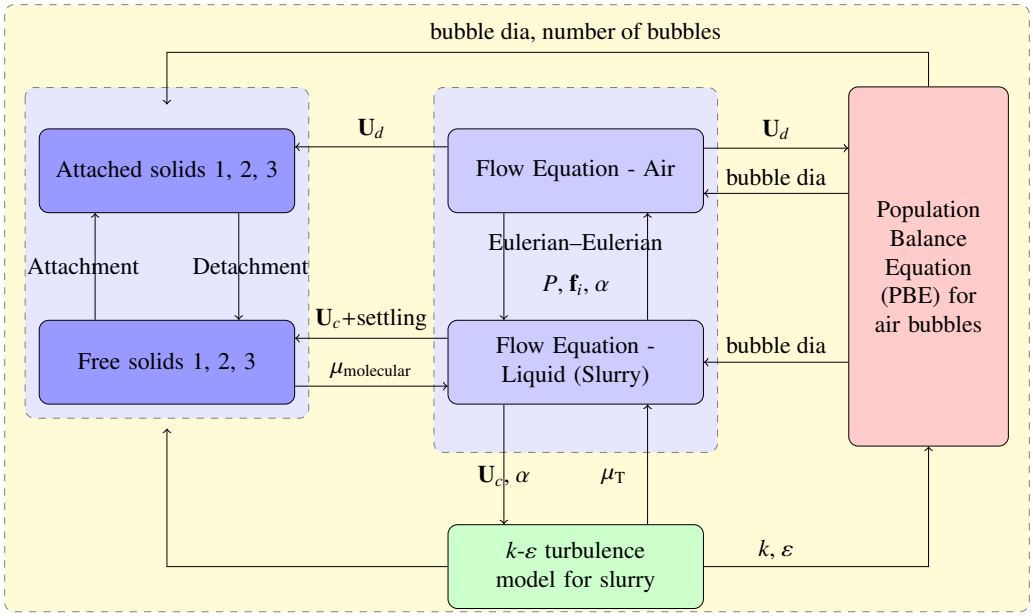

Figure 1: Coupling of the model equations used for modelling the three-phase pulp phase in a flotation column.

model detrimental to validation (Pfleger and Becker, 2001). A study by Zaruba et al. (2005) experimentally showed the contribution of BIT an order or magnitude smaller than the shear-induced turbulence in a thin rectangular bubble column, similar to the geometry employed in the present work. The BIT model was excluded from the present model due to its mixed acceptance in the literature.

A common pressure field was considered for the two Eulerian phases (Bhutani et al., 2016), which required that only one (common) continuity equation had to be solved. The common continuity equation is given as (Ishii and Hibiki, 2010):

$$\nabla \cdot (\alpha_d \mathbf{U}_d) + \nabla \cdot (\alpha_c \mathbf{U}_c) = 0, \tag{2}$$

In polydisperse flow modelling, the interphase interaction force $\mathbf{f}_i$, which includes the drag and non-drag forces, is responsible for coupling the dispersed phase particle size to the model momentum equations. The drag force, which is the most significant of all interphase forces, consists of both the pressure and the viscous drag on the body, and can be written as:

$$\mathbf{f}_i = \pm \frac{3\alpha_c \alpha_d C_D \rho_c (\mathbf{U}_c - \mathbf{U}_d)|\mathbf{U}_c - \mathbf{U}_d|}{4d}, \tag{3}$$

where C_D is the drag coefficient and d is the dispersed phase diameter. In the present work the Schiller–Naumann drag force correlation was used to obtain the drag coefficient (Schiller and Naumann, 1935). This coefficient models the drag well for viscous and Newton's flow regimes (Ishii and Hibiki, 2010), which were prominent in the present situation. Many others have also used the Schiller–Naumann correlation to model drag in bubbly flows (Buwa and Ranade, 2002; Chen et al., 2005). It is given as:

$$C_D = \begin{cases} \dfrac{24}{Re_d}\left(1 + 0.15 {Re_d}^{0.687}\right) & \text{if } Re_d < 1000, \\ 0.44 & \text{otherwise,} \end{cases} \tag{4}$$

where Re_d, the dispersed phase Reynolds number, is defined as:

$$Re_d = \frac{\rho_c d|\mathbf{U}_c - \mathbf{U}_d|}{\mu_c}. \tag{5}$$

Equation (4) clearly shows the two flow regimes—the viscous flow regime with a strong dependence of the drag coefficient on Re_d and the Newton's regime with C_D independent of Re_d. The non-drag force includes the lift and virtual mass forces, plus other forces such as the Basset force, the Brownian force and the thermophoretic force. These forces, however, were neglected in the present model as their effect on the flow is negligible (Chen et al., 2004; Tabib et al., 2008; Díaz et al., 2008a). Reynolds-averaging of the discontinuities in the phases, which results in the interphase interaction force term discussed above, also gives rise to additional terms such as the interfacial pressure term and the interfacial shear stress terms ($\sim \nabla\alpha_i$), both of which were neglected in the present formulation (Bhutani, 2016). The turbulent dispersion force term, which originates from the continuous phase velocity fluctuations and affects bubble motion was neglected in the present model due to its disputed nature (Ishii and Hibiki, 2010).

The dispersed phase volume fraction, α_d, was obtained from the solution to:

$$\frac{\partial \alpha_d}{\partial t} + \nabla \cdot (\alpha_d \mathbf{U}_d) = 0 \tag{6}$$

and the conservation equation

$$\alpha_d + \alpha_c = 1 \tag{7}$$

was used to obtain continuous phase volume fraction α_c.

The Reynolds stress, $\bar{\bar{\tau}}_c^R$, is a result of the Reynolds-averaging of the non-linear convective term in the momentum equation and is responsible for applying the effect of turbulent fluctuations on the mean flow. Since turbulence was only modelled for the continuous phase, the subscript c has been omitted in the subsequent discussion on turbulence modelling. The turbulent viscosity hypothesis introduced by Boussinesq was used to close the Reynolds stress term, given as:

$$\bar{\bar{\tau}}^R = -\rho\langle \mathbf{u}'\mathbf{u}'\rangle = \mu_T\left(\nabla\mathbf{U} + (\nabla\mathbf{U})^T\right) - \frac{2}{3}k\rho\bar{\bar{I}}. \tag{8}$$

In the above equation, $\mathbf{u}'$ is the fluctuating component of the liquid velocity and μ_T is the (isotropic) eddy viscosity. The eddy viscosity in the k-ε model, which is the simplest complete model for turbulence, is defined as:

$$\mu_T = \rho C_\mu \frac{k^2}{\varepsilon}, \tag{9}$$

where C_μ is a model constant. The turbulent kinetic energy, $k = \frac{1}{2}\langle \mathbf{u}' \cdot \mathbf{u}'\rangle$, is the mean kinetic energy per unit mass in the fluctuating velocity, and the turbulent dissipation rate, $\varepsilon = \frac{2\mu}{\rho}\langle \bar{\bar{s}} \cdot \bar{\bar{s}}\rangle$ ($\bar{\bar{s}}$ being the fluctuating rate of deformation tensor), quantifies the dissipation of turbulent kinetic energy at small scales. Standard form of the transport equations for k and ε (Jones and Launder, 1973) were solved; the equations are given as:

$$\alpha\rho\frac{\partial k}{\partial t} + \alpha\rho\mathbf{U}\cdot\nabla k = \nabla\cdot\left(\alpha\left(\mu + \frac{\mu_T}{\sigma_k}\right)\nabla k\right) + \alpha\bar{\bar{\tau}}_R : \nabla\mathbf{U} - \alpha\rho\varepsilon \tag{10}$$

and

$$\alpha\rho\frac{\partial \varepsilon}{\partial t} + \alpha\rho\mathbf{U}\cdot\nabla\varepsilon = \nabla\cdot\left(\left(\alpha\mu + \frac{\mu_T}{\sigma_\varepsilon}\right)\nabla\varepsilon\right) + C_{\varepsilon 1}\left(\frac{\varepsilon_i}{k}\right)\left(\alpha\bar{\bar{\tau}}_R : \nabla\mathbf{U}\right) - C_{\varepsilon 2}\alpha\rho\frac{\varepsilon^2}{k}. \tag{11}$$

The RHS terms in both equations consist of the diffusion, the production from mean shear, and the destruction term. Interphase interaction terms appearing in the k and ε equations were neglected here, as did Ranade (1997) and Buwa and Ranade (2002). Model constants suggested by Launder and Sharma (1974) were used in this study (Table 1). σ is the turbulence Schmidt number here.

Table 1
Model constants in the standard k-ε model given by Launder and Sharma (1974).

C_μ	0.09
$C_{\varepsilon 1}$	1.44
$C_{\varepsilon 2}$	1.92
σ_k	1.0
σ_ε	1.3

Koh and Schwarz (2007) incorporated the effect of attached particles on the gas bubble weight through a body force term in the gas momentum equation. Further, they also presented the effect of modifying the buoyancy term on the prediction of flotation rate. The present model does not include the buoyancy modification term.

2.2. Population balance equation

The population balance equation is a mesoscale integro-differential equation that can be used to model the evolution of the size distribution of polydisperse particles (Ramkrishna, 2000; Marchisio and Fox, 2013). In this study, the PBE was used to model the evolution of the size distribution of the bubbles only. The polydispersity of the solids was modelled using three separate classes, which will be discussed later in Section 3. The moving bubbles in a flotation system coalesce and break, which results in the spatial and temporal evolution of their distribution.

The PBE can be written as:

$$\frac{\partial n(\xi, \mathbf{x}, t)}{\partial t} + \nabla\cdot\left(\langle \mathbf{u}|\xi\rangle\, n\right) = S_\xi(\xi, \mathbf{x}, t), \tag{12}$$

where $n(\xi, \mathbf{x}, t)$ is the dispersed phase number density function (NDF), ξ is the internal coordinate (representing the dispersed phase size), and $\mathbf{x}$ is the external (or spatial) coordinate. $\langle \mathbf{u}|\xi\rangle$ is the mean dispersed phase velocity conditional to the bubble size and is responsible for convecting the bubbles in the physical space. However this dependence on the dispersed phase size was not considered in the present study and the air velocity field computed using Equation (1) was used in the PBE. Only one internal variable—the bubble size—was of interest in this work, however multivariate PBE containing more than one internal variable has also been discussed in the literature (Buffo and Alopaeus, 2016).

S_ξ, the source term in Equation (12), includes all terms containing derivatives or integrals with respect to the dispersed phase size ξ. It can be used to model dispersed phase growth, diffusion in the internal space, and the birth and death functions due to dispersed phase breakage and coalescence. Growth and internal diffusion terms did not arise in the present model and were not included in Equation (12).

As discussed previously, the PBE in this work was used to estimate the bubble size in the flotation system to accurately model the drag force term in momentum equations (Equations (1) and (1)). The PBE was also used to calculate the bubble concentration, which was needed in the bubble–particle attachment and detachment models.

Breakage and coalescence are discontinuous events that lead to the birth and death of bubbles in a very short time. The contribution to the source term S_ξ from birth and death functions due to bubble breakage and coalescence is given as:

$$S_\xi = B_B + B_C - D_B - D_C. \tag{13}$$

The birth and death functions due to breakage are given as:

$$B_B(\xi) = \int_{\xi}^{\infty} \nu(\xi_1) a(\xi_1) b(\xi|\xi_1) n(\xi_1)\, \mathrm{d}\xi_1 \tag{14}$$

and

$$D_B(\xi) = a(\xi) n(\xi), \tag{15}$$

respectively. Here, $\nu(\xi)$, $a(\xi)$ and $b(\xi|\xi_1)$ are the breakage kernels that define the number of bubbles formed after breakage, the breakage frequency, and the daughter distribution function, respectively. Note that the spatial and temporal dependence of the NDF has been suppressed here for compactness.

Coalescence is described in terms of a coalescence frequency $\beta(\xi', \xi)$ for bubbles of sizes ξ' and ξ. If there is no statistical correlation between the colliding bubbles, the bubble pairs can be defined as the product of two individual number densities, and the birth and death functions due to coalescence are given as:

$$B_C = \frac{1}{\tilde{\delta}} \int_0^{\xi} \left(\frac{\xi^2}{\xi'^2} \right) \beta(\xi', \xi_1) n(\xi') n(\xi_1)\, \mathrm{d}\xi_1 \tag{16}$$

and

$$D_C = \int_0^{\infty} \beta(\xi, \xi_1) n(\xi) n(\xi_1)\, \mathrm{d}\xi_1, \tag{17}$$

respectively. $\tilde{\delta}$ in the above equation represents the number of bubbles coalescing to form a larger bubble. In Equation (16), ξ' is given as $\xi'^3 = \xi^3 - \xi_1^3$, i.e. the volume of the resulting bubble class (ξ) is the sum of the volumes from the contributing size classes (ξ' and ξ_1).

The internal coordinate presents the major challenge in the numerical solution of the PBE. Most methods eliminate the internal coordinate from the PBE to bring it in a form that can be solved numerically using established methods. The popular numerical solution methods for the PBE can be grouped into two general categories—the method of classes and the method of moments. The CM discretises the internal coordinate in the NDF, giving rise to various classes (Marchal et al., 1988). The PBE transforms to a set of advection–diffusion equations for the discretised NDF corresponding to each class. A large number of classes are needed for a reasonable accuracy when the PBE is coupled to the multiphase flow equations, which makes the solution of a normal engineering system extremely expensive. For instance, Sarhan et al. (2017) used 10 classes for the bubble NDF in their flotation column model, which equates to solving 10 extra advection–diffusion equations in addition to the multiphase flow equations. The size distribution can change significantly in a very short time due to the discontinuous nature of the breakage and coalescence events, and therefore a large number of classes must be considered to factor this possibility.

The method of moments (MOMs), as the name suggests, solves for the evolution of the moments of the NDF instead; k^{th} moment of the NDF can be written as $m_k = \int_0^{\infty} \xi^k n(\xi)\, \mathrm{d}\xi$. The internal coordinate gets integrated when the moments of the NDF are evaluated in the PBE, but in the process various unclosed terms are generated. The various methods of moments available in the literature are differentiated based on the closure method used. Quadrature-based moment methods are popular as they are simple and robust, and the mathematical closure in the QBMM can be applied to any problem without an understanding of its physics. In this method, the higher-order unclosed moments are written in terms of the lower-order moments, which are transported. QMOM and DQMOM are two popular QBMMs used in the literature. QMOM approximates the integrals in terms of weights and abscissas (McGraw, 1997), whereas DQMOM uses a quadrature approximation for the NDF itself (Marchisio and Fox, 2005), given by:

$$n(\xi, \mathbf{x}, t) = \sum_{j=1}^{N} w_j(\mathbf{x}, t)\, \delta\left[\xi - \langle\xi\rangle_j(\mathbf{x}, t)\right], \tag{18}$$

where δ is the Dirac delta function, N is the total number of quadrature points, and w_j and $\langle\xi\rangle_j$ are the weights and abscissas in the DQMOM approximation, respectively. DQMOM was chosen to solve the PBE in this work because each weight and abscissa can be defined as a function of space, which makes the implementation of the method in a CFD code straightforward. Also, very few abscissas are needed to accurately model the NDF due to the adaptive quadrature approach of DQMOM.

The DQMOM approximation to the NDF when substituted into the PBE (Equation (12)) results in the following set of transport equations (Marchisio and Fox, 2005):

$$\frac{\partial w_j}{\partial t} + \nabla \cdot \left(\mathbf{u}\, w_j\right) = g_j \tag{19}$$

and

$$\frac{\partial \varsigma_j}{\partial t} + \nabla \cdot \left(\mathbf{u}\, \varsigma_j\right) = h_j, \tag{20}$$

where $j = 1, 2, ..., N$. The source terms g_j and h_j are obtained from the solution of the linear system

$$(1-k) \sum_{j=1}^{N} \langle\xi\rangle_j^k g_j + k \sum_{j=1}^{N} \langle\xi\rangle_j^{k-1} h_j = \overline{S}_k^{(N)}, \tag{21}$$

which is obtained by computing the k^{th} moment of the PBE; here $k = 1, 2, ..., 2N$. The above set of equations were solved for the weights w_j and the weighted abscissas ς_j, which were then used to calculate the moments and eventually the Sauter mean diameter ($d_{32} = m_3/m_2$). The bubble surface area flux is an important parameter that is used to characterise flotation and since the Sauter mean diameter (SMD) includes the effect of the total surface area of the bubbles (through m_2) it was used as an estimate for the bubble diameter in this study. $\overline{S}_k^{(N)}$ is the k^{th} moment of the source term in the PBE and the DQMOM approximation to the NDF provides a convenient closure for this source term. It is given as:

$$\begin{aligned} \overline{S}_k^{(N)} = &\sum_{j=1}^{N} \overline{b}_j^{(k)} a_j w_j - \sum_{j=1}^{N} \langle\xi\rangle_j^k a_j w_j \\ &+ \frac{1}{2} \sum_{j=1}^{N} \sum_{i=1}^{N} \left(\langle\xi\rangle_j^3 + \langle\xi\rangle_i^3 \right)^{k/3} \beta_{ji} w_j w_i - \sum_{j=1}^{N} \sum_{i=1}^{N} \langle\xi\rangle_j^k \beta_{ji} w_j w_i, \end{aligned} \tag{22}$$

where the term $\overline{b}_j^{(k)}$ is given as:

$$\overline{b}_j^{(k)} = \int_0^\infty \xi^k b(\xi|\langle\xi\rangle_j)d\xi. \quad (23)$$

In the above equation, $b(\xi|\langle\xi\rangle_j) = 0$ for $\xi > \langle\xi\rangle_j$, which restricts the daughter bubble size to be smaller than the parent. The breakage kernel $\nu(\xi)$ is usually absorbed in the daughter distribution function $b(\xi|\xi_1)$ (Marchisio et al., 2003b,a) and has been omitted from Equation (22).

Compared to the CM, DQMOM requires a fewer number of equations that need to be solved to get a good estimate of the BSD. For instance, Marchisio et al. (2003b) stated that 4–6 equations in DQMOM (i.e., N=2–3) provide similar accuracy as 50–200 classes in the CM. Two quadrature points were used in the DQMOM approximation in this study.

The problem of moment corruption (i.e., the moment-set becoming invalid or unrealisable) has been reported with the use of the MOMs in the literature (Petitti et al., 2010). However, it has been established that the first-order upwind convective scheme in the finite volume discretisation, which was used for the PBE transport equations in this work, always leads to realisable moments for $N \leq 3$ (Desjardins et al., 2008; Mazzei et al., 2012). The details of the implementation of DQMOM in Fluidity and its verification have been presented in a previous publication by the authors (Bhutani et al., 2016).

2.2.1. Kernels

The breakage and coalescence kernels are chosen based on the physics of the problem under consideration. The most widely accepted theory for bubble breakage states that the bubble breakage phenomenon is characterised by a balance between the forces in the liquid trying to deform the bubble (the turbulent fluctuations) and the restoring force due to interfacial tension (Andersson and Andersson, 2006). On the same lines, the breakage rate proposed by Laakkonen et al. (2006) was used for modelling bubble breakage in this work. It is given as:

$$a(\xi) = C_1\varepsilon^{1/3}\mathrm{erfc}\left(\sqrt{C_2\frac{\sigma}{\rho_c\varepsilon^{2/3}\xi^{5/3}} + C_3\frac{\mu_c}{\sqrt{\rho_c\rho_d}\varepsilon^{1/3}\xi^{4/3}}}\right), \quad (24)$$

where σ is the gas–liquid interfacial tension, and C_1, C_2 and C_3 are empirical model constants with C_1 having dimensions of $\mathrm{L}^{-2/3}$. The stabilising effect of viscous stresses was also considered along with the interfacial tension effects in the above breakage rate kernel. Other popular choices for the breakage kernels are the ones proposed by Coulaloglou and Tavlarides (1977), Luo and Svendsen (1996) and Prince and Blanch (1990).

Binary breakage was assumed in this work ($\nu(\xi) = 2$), and the daughter distribution function proposed by Laakkonen et al. (2007) was employed in this study. It is given as:

$$b(\xi_1|\xi_2) = \frac{1}{2}(C_4{+}1)(C_4{+}2)(C_4{+}3)(C_4{+}4)\left(\frac{{\xi_1}^2}{{\xi_2}^3}\right)\left(\frac{{\xi_1}^3}{{\xi_2}^3}\right)^2\left(1-\frac{{\xi_1}^3}{{\xi_2}^3}\right)^{C_4}. \quad (25)$$

The above expression does not take the effect of turbulence or any other parameter, other than the bubble size, into account. It is mathematically well-posed and numerically more stable than the other expressions (Luo and Svendsen, 1996). C_4 is a constant that can be calculated using the normalisation property of daughter distribution function.

Bubble coalescence is considered more complex than breakage because it not only involves the interaction between bubbles and liquid, as in breakage, but also between different bubbles. The coalescence rate kernel is written as a product of the collision frequency and the coalescence efficiency. It is the turbulence in the continuous phase that is responsible for the collision between the bubbles in the pulp zone. The coalescence efficiency is modelled by comparing the film drainage time with the bubble interaction time. Assuming the coalescing bubble interfaces to be immobile, Laakkonen et al. (2006) obtained the following expression for the coalescence efficiency:

$$\eta(\xi_1,\xi_2) = \exp\left[-C_6\frac{\mu_c\rho_c\varepsilon}{\sigma^2}\left(\frac{\xi_1\xi_2}{\xi_1+\xi_2}\right)^4\right]. \quad (26)$$

The coalescence rate was therefore given as:

$$\beta(\xi_1,\xi_2) = C_5\varepsilon^{1/3}\left(\xi_1+\xi_2\right)^2\left({\xi_1}^{2/3}+{\xi_2}^{2/3}\right)^{1/2}\eta(\xi_1,\xi_2), \quad (27)$$

and the same was used in the present study. Binary collision was assumed here ($\tilde{\delta} = 2$). For more details on the theory of bubble breakage and coalescence and the choice of kernels, see Bhutani (2016).

Evans et al. (2008) proposed their own kernels for breakage and coalescence, whereas Koh and Schwarz (2008b) used the breakage and coalescence kernels of Luo and Svendsen (1996) and Prince and Blanch (1990), respectively, to model flotation. Buffo et al. (2013) reported promising results for modelling bubble columns through the use of the breakage and coalescence kernels of Laakkonen et al. (2006); the same kernels were used in this work. Although the coalescence and breakage kernels of Laakkonen et al. (2006, 2007) used in this work have been derived for pure liquid and bubble systems, Koh and Schwarz (2008b) used similar liquid–gas expressions in their flotation simulations reporting a reasonable match with the experiments. However, it will be ideal to include kernels that can account for the the effect of solids and surfactants, which, to the best knowledge of the authors, do not exist in the literature currently.

2.3. Solids

2.3.1. Transport equations for solids

Transport equations for the free and attached solids in the pulp were solved. The total solid concentration inside the column, n_{tot}, can be given as:

$$n_{\mathrm{tot}}(\mathbf{x},t) = n_f(\mathbf{x},t) + n_a(\mathbf{x},t), \quad (28)$$

where n_f and n_a are the concentrations of the free and attached particles, respectively, in number per unit volume ($\#/m^3$).

Transport equations that were solved for $n_f(\mathbf{x}, t)$ and $n_a(\mathbf{x}, t)$ can be written as:

$$\frac{\partial n_f}{\partial t} + (\mathbf{U}_c + \mathbf{u}_{\text{settling}}) \cdot \nabla n_f = -\psi_a + \psi_d, \tag{29a}$$

$$\frac{\partial n_a}{\partial t} + \mathbf{U}_d \cdot \nabla n_a = \psi_a - \psi_d. \tag{29b}$$

Here, ψ_a is the rate of particle–bubble attachment and ψ_d is the rate of detachment. A settling velocity $\mathbf{u}_{\text{settling}}$ was added to the continuous phase velocity to get the advection velocity of the free particles, as seen in Equation (29a). The attached particles advect with the dispersed phase velocity $\mathbf{U}_d$

2.3.2. Attachment rate

The particle attachment rate was modelled as a product of the number of collisions between free particles and available bubbles and the probability of successful attachment. Is is given as:

$$\psi_a = Z_1 n_f n_b^A P_c P_a P_s, \tag{30}$$

where Z_1 is the collision rate factor (m^3s^{-1}), n_b^A is the concentration of bubbles available for attachment, and P_c, P_a and P_s are the probabilities of collision, adhesion and stabilisation, respectively.

Collision rate factor

Abrahamson (1975) was the first to derive the collision rate factor between particles in a highly turbulent fluid. The same expression was later used by Koh et al. (2000) and Bloom and Heindel (2002) to estimate the collision rate between particles and bubbles in flotation. Based on the previous studies the same collision rate factor was used in the present work, given as:

$$Z_1 = 5.0 \left(\frac{d_s + d_b}{2}\right)^2 (u_{t,s}^2 + u_{t,b}^2)^{1/2}, \tag{31}$$

where d_b is the bubble diameter, d_s is the particle diameter, $u_{t,s}$ is the RMS fluctuating velocity for the particles and $u_{t,b}$ is the RMS fluctuating velocity for the bubbles.

For large colliding particles and/or high intensity turbulence the particles do not follow the fluid streamlines and the particle velocities can be assumed to be distributed independently (in magnitude and direction). The particle velocity distribution in the above model is assumed to be Gaussian and the velocity fluctuations are represented in terms of the turbulent dissipation rate as (Koh and Schwarz, 2006; Bloom and Heindel, 2002):

$$u_{t,i} = \frac{0.4\varepsilon^{4/9}\rho_l^{1/3} d_i^{7/9}}{\mu_l^{1/3}} \left(\frac{\rho_i - \rho_l}{\rho_l}\right)^{2/3}, \tag{32}$$

where the subscript i refers to solid and gas (bubble) phases. Colliding species—particles and bubbles—are collectively referred to as 'particles' in this section in the interest of simplicity.

Equation (31) was also used by Koh and Schwarz (2006) in their pulp phase CFD model for uncorrelated solid particle and bubble velocities. The solid particle and bubble velocities remain uncorrelated as long as turbulence in the fluid is isotropic at the scale of colliding particles (which may be true even when the large-scale motion is statistically anisotropic) and the two colliding particles are moving in independent fluid elements. Velocities for the fluid elements close to each other in space will be correlated, but if the particle inertia is sufficiently larger than the drag on the particle due to these correlated elements the independence of particle velocities can be assumed. The above condition is quantified by comparing the particle relaxation time to the characteristic time for velocity fluctuation at a distance over which the fluid velocities are correlated. This results in a critical particle diameter expression, given as:

$$d_{\text{crit}} = \sqrt{\frac{15\mu_l u_{t,l}^2}{\rho_i \varepsilon}}. \tag{33}$$

For a typical flotation situation d_{crit} is 1 mm for air bubbles and 0.5 mm for solid particles (of density $2500\,\text{kgm}^{-3}$). However, the value may change depending the intensity of turbulence at a given location. Since the diameter of the bubbles introduced into the column was 5 mm Abrahamson's collision rate factor was applicable in such cases. Abrahamson's collision rate factor (Equation (31)) is therefore applicable when the solid particle or bubble diameter is greater than the above critical diameter (Koh and Schwarz, 2006). Here, $u_{t,l}$ is the RMS fluctuating velocity of the liquid phase which is equal to $\sqrt{2k}$. For bubbles, ρ_i in the above equation is taken as $0.5\rho_l$. Equation (31) is therefore applicable when the following conditions are satisfied: high-intensity turbulence in the flow, turbulence is isotropic on the scale of colliding particles, particles are nearly spherical, and the particle size is greater than the critical diameter for the solid particle and bubble velocities to be independent. Most of the above conditions were applicable in the present situation for particle–bubble collisions in flotation. The particles (and larger bubbles) however are not spherical and this is an assumption that is made here to ensure the applicability of Equation (31).

In case the solid particle and bubble velocities are correlated (i.e. for low intensity turbulence), the collision rate expression developed in the past by Saffman and Turner (1956) was used (same as Koh and Schwarz (2006)):

$$Z_1 = \sqrt{\frac{8\pi}{15}} \left(\frac{d_s + d_b}{2}\right)^3 \left(\frac{\varepsilon\rho_l}{\mu_l}\right)^{1/2}. \tag{34}$$

The above expression is based on the classical 'gradient collision' model of Smoluchowski (1917), which derives the collision rate of particles moving under uniform shear. This model assumes $d_s + d_b$ to be smaller than the smallest eddies and that the particles move with the fluid (i.e. they have a small inertia).

Bubbles available for attachment

Different approximations have been used to estimate the available bubble concentration in the literature. Bloom and Heindel

(1997) assumed that only one particle can attach to a bubble, whereas Bloom and Heindel (2003) assumed that only the bubbles that have no particle attached to them are available for attachment. Some replaced the number concentration of available bubbles with the total bubble concentration. In this work, the assumption of Koh and Schwarz (2006) of the bubbles being either fully loaded or completely clean was used. The bubble loading parameter β_{bub} was, therefore, defined as:

$$n_b^A = (1 - \beta_{\text{bub}}) n_b^{\text{tot}}, \tag{35}$$

where n_b^{tot} is the total bubble concentration. The bubble loading factor for a particular solid class i was calculated as:

$$\beta_{\text{bub},i} = \left(\frac{n_{a,i}}{n_b^{\text{tot}}}\right)\left(\frac{d_{s,i}}{d_b}\right)^2 0.5, \tag{36}$$

assuming 50% maximum loading. The total bubble concentration n_b^{tot} was calculated using the value of zeroth moment, m_0, of the bubble NDF. Equation (36) assumes that loaded bubbles always contain particles of the same size.

Collision probability

The probability of collision between free particles and bubbles in this work was calculated using the expression derived by Yoon and Luttrell (1989), given as:

$$P_c = \left(\frac{3}{2} + \frac{4}{15} Re_b^{0.72}\right)\left(\frac{d_s}{d_b}\right)^2. \tag{37}$$

This expression is based on an isolated bubble rising in particle suspension in a quiescent flow. The particles are assumed to follow fluid streamlines around the bubble, which is a reasonable assumption if the particle inertia is small. The particles and bubbles are assumed to be spherical. It was theorised by Sutherland (1948) that the particles lying inside the *grazing streamline* are able to collide with bubbles successfully. Using this theory, the probability of collision was defined as the fraction of particles in the bubble path that end up colliding with it, quantified as the ratio of the area inscribed by limiting radius R_0 to the area inscribed by bubble radius R_b, as shown in Figure 2. Yoon and Luttrell (1989) developed an empirical relation for R_0 as a function of the bubble Reynolds number (below 100), through measurements of fluid streamlines. This led to the expression for the collision probability as defined in Equation (37). Equation (37) was also used by Koh and Schwarz (2006) in their pulp phase models. Three other collision mechanisms, namely the gravitational, inertial and turbulent collision are possible (Wang et al., 2018); however, only the interceptional collision mechanism, as described above, was considered in this work.

Adhesion probability

The short-range surface forces start acting once the particle is close enough to the bubble after collision. Sutherland (1948) theorised that for the thermodynamically feasible cases the bubble–particle adhesion occurs when the particle "sliding time" is larger than the "induction time", which is the minimum time required for the liquid film to thin and rupture. For given

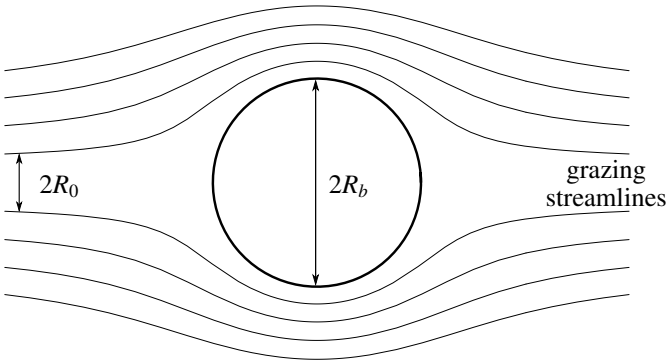

Figure 2: Fluid streamlines around a spherical bubble. Solid particles outside the *grazing streamlines* do not contact the bubble.

particle and bubble sizes, there is a maximum incidence angle that the incoming particle must hit at for the adhesion to be successful. For particles approaching at angles above this maximum angle, the sliding distance will not be long enough for the film thinning to occur in time. Yoon and Luttrell (1989) quantified the adhesion probability as the ratio of the area inscribed by the limiting radius (corresponding to the maximum incidence angle) to the area inscribed by the sum of bubble and particle radii. This adhesion probability is equal to $\sin^2\theta_{\text{inc}}$, θ_{inc} being the maximum incidence angle. Using the empirical relation for fluid streamlines as a function of bubble Reynolds number, Yoon and Luttrell (1989) derived the sliding time in terms of the incidence angle, assuming the particle inertial to be small. Equating the sliding and induction times for the maximum incidence case, the adhesion probability was obtained as:

$$P_a = \sin^2\left(2\arctan\left\{\exp\left[\frac{-(45 + 8Re_b^{0.72})u_{t,b}t_{\text{ind}}}{15d_b(d_b/d_s + 1)}\right]\right\}\right). \tag{38}$$

The following well-known relation for the induction time was used in this work:

$$t_{\text{ind}} = A_{\text{ind}} d_s^{B_{\text{ind}}}, \tag{39}$$

where $A_{\text{ind}} = 75/\theta_{CA}$ (θ_{CA} is the contact angle in degrees) and $B_{\text{ind}} = 0.6$, using the statistical fitting performed by Dai et al. (1999) and Koh and Schwarz (2006). Definition of the fitting parameter A is consistent with the fact that the induction time is short for hydrophobic surfaces (Wills and Finch, 2016). Although the effect of collectors has not been modelled here, they will affect the induction time directly through a change in the contact angle of the mineral surface.

Ideally the adhesion probability should also consider the extent of liberation of the mineral in the crushed ore. It is generally not economical to crush the ore to very fine particle size to liberate all mineral particles. Hence the partially-liberated ore has a lower probability of attaching to the bubbles as compared to a fully-liberated one. Welsby et al. (2010) measured the flotation rate as a function of particle size for different mean liberation values, noticing a clear trend. Jameson (2012) showed that the ratio of the rate constant for a partially liberated particle sample to a fully liberated sample was a unique function of liberation

independent of particle size, called the *liberation function*. Albijanic et al. (2011) saw a clear reduction in the adhesion time as the liberation of the mineral increased, through their experiments. There is currently no study that quantifies this effect of liberation on the adhesion probability and the effect of liberation therefore was not considered in the present model.

Stabilisation probability

Schulze (1993) proposed the stabilisation probability of the particle–bubble aggregates in a flotation pulp as:

$$P_s = 1 - \exp\left(1 - \frac{1}{Bo^*}\right). \tag{40}$$

Here Bo^* is the modified Bond number defined as the ratio of detachment to attachment forces. It is given as:

$$Bo^* = \frac{d_s^2\left[(\rho_s - \rho_l)|\mathbf{g}| + 1.9\rho_s\varepsilon^{2/3}\left(\frac{d_s+d_b}{2}\right)^{-1/3}\right]}{|6\sigma\sin\left(\pi - \frac{\theta_{CA}}{2}\right)\sin\left(\pi + \frac{\theta_{CA}}{2}\right)|} + \frac{1.5d_s\left(\frac{4\sigma}{d_b} - d_b\rho_l|\mathbf{g}|\right)\sin^2\left(\pi - \frac{\theta_{CA}}{2}\right)}{|6\sigma\sin\left(\pi - \frac{\theta_{CA}}{2}\right)\sin\left(\pi + \frac{\theta_{CA}}{2}\right)|},$$

where $\mathbf{g}$ is the acceleration due to gravity vector. In the above expression it is assumed that turbulent eddies of similar size as the bubble–particle aggregate cause detachment. Turbulence and capillary forces can be seen competing with each other in the above expression for the modified Bond number. This expression for stabilisation probability was used in the present flotation modelling framework.

2.3.3. Detachment rate

The particle detachment rate was given by:

$$\psi_d = Z_2 n_b^L P_d, \tag{42}$$

where Z_2 is the detachment frequency $(1/t)$, n_b^L is the concentration of loaded bubbles and P_d is the destabilisation probability. The detachment frequency due to the turbulent eddies was calculated using:

$$Z_2 = \frac{\sqrt{\tilde{C}}\varepsilon^{1/3}}{(d_s + d_b)^{1/3}}, \tag{43}$$

where the constant $\tilde{C}$ was taken to be equal to 2 (Bloom and Heindel, 2002, 2003; Koh and Schwarz, 2006). The concentration of loaded bubbles was calculated using $n_b^L = \beta_{\text{bub}} n_b^{\text{tot}}$. The destabilisation probability was calculated simply as $1 - P_s$.

2.3.4. Settling velocity of solids

Richardson and Zaki (1954) obtained the relation for the settling velocity of a suspension of uniform spherical particles as:

$$\mathbf{u}_{\text{settling}} = \frac{\mathbf{g}(\rho_s - \rho_l)d_s^2}{18\mu_l}\epsilon_s^{4.65}, \tag{44}$$

where the subscripts s and l refer to the solid and liquid, respectively. ϵ_s is the porosity in the solid-liquid mixture that can be written as:

$$\epsilon_s = 1 - n_f V_s. \tag{45}$$

Here, V_s is the volume of a solid particle. Equation (44) was used to calculate the settling velocity of free solids, which was superimposed on the liquid velocity field for getting the advection velocity in the free-solid scalar equation (Equation (29a)). The pulp phase models presented by Koh and Schwarz have also included the effect of the settling velocity of the particles, which can be verified from the settled unattached particles at the bottom of their tanks, as shown clearly in Koh and Schwarz (2008a, 2009). The settling velocity expression used by them, however, was not specified in their works. Neglecting the settling velocity would mean that the larger (and heavier) solid particles will also follow fluid streamlines like the lighter ones, which is physically incorrect. This equation however is only used for the better estimation of the advection term in the free-solid transport equation as no momentum equation for the free solids is solved in the present model.

2.3.5. Viscosity modification of the liquid phase

The collision between the solid particles in liquid phase manifests as an increased viscosity the of liquid. Einstein's equation, which relates the slurry viscosity μ_{slurry} to the solid volume fraction ϕ for spherical particles, is generally applicable to very dilute systems and the equation does not apply to higher solid concentrations. Krieger and Dougherty (1959) proposed an expression for the change in the viscosity of a fluid due to the presence of high concentration of rigid spherical particles as:

$$\mu_{\text{slurry}} = \mu_l\left(1 - \frac{\tilde{\phi}}{\tilde{\phi}_{\max}}\right)^{-[\mu]\tilde{\phi}_{\max}}, \tag{46}$$

where μ_l is the molecular viscosity of the fluid, $\tilde{\phi}$ is the solid volume fraction, $\tilde{\phi}_{\max}$ is the maximum packing fraction that the solid particles can achieve and $[\mu]$ is the intrinsic viscosity. Intrinsic viscosity is the limiting value of $(\mu_{\text{slurry}}/\mu_l - 1)/\tilde{\phi}$, which is equal to 2.5 using Einstein's equation. Merve Genc et al. (2012) used the values 2.5 and 0.74 for $[\mu]$ and $\tilde{\phi}_{\max}$ respectively, in Equation (46) for estimating the pulp viscosity in nickel sulphide flotation. Many other empirical and semi-empirical relations between μ_{slurry} and $\tilde{\phi}$ have been proposed (Shook and Roco, 1991). Equation (46) was used in the present work with the values 2.5 and 0.70 for $[\mu]$ and $\tilde{\phi}_{\max}$, respectively. Maximum solid packing fraction of 0.74 can be considered as a theoretical maximum (corresponding to hexagonally-packed spherical particles) that can be attained; real measured values are much smaller (order of 0.01 due to the gangue fibre mesh). The higher $\tilde{\phi}_{\max}$ value allows for the slurry to attain higher $\tilde{\phi}$ values and still keep flowing. Moreover, the flotation simulations demonstrated in this work are for a batch flotation system containing mineral particles only, therefore allowing higher values of $\tilde{\phi}_{\max}$. The solid volume fraction was calculated as

$\tilde{\phi} = 1 - \epsilon$ using Equation (45). Koh and Schwarz (2008a) have reported the use of modified viscosity in their pulp phase model. They used the Herschel Bulkley non-Newtonian model with the consistency and flow indices fitted for various pulp densities.

Since the viscosity modification is the only way to apply the effect of free solids on the liquid velocity field, this step is necessary. It is independent of the settling velocity modification in Equation (44), which does not impact liquid velocity as the free-solid transport equation does not modify liquid velocity in any way in the approach used in this paper. If a separate momentum equation was being solved for the free solids, viscosity modification of the liquid phase would impact solid velocity field and the Richardson and Zaki settling equation would not be needed. In the present model, the viscosity modification and Richardson and Zaki equation are used to independently apply the effect of free solids on the liquid velocity and the solid velocity, respectively.

Table 2 shows a comparison of the features of the present pulp phase simulation framework with previous studies.

2.4. Numerical discretisation

Fluidity is an open-source code that uses the finite element method (FEM) for solving coupled PDEs. The FEM was chosen over the finite difference method (FDM) as the finite element (FE) discretisation has been shown to naturally go well with the unstructured meshes (Wilson, 2009), which were used in the present work. Implementing higher-order discretisations is not straightforward in the finite volume method (FVM) and the FEM was chosen over it for reason that it provides a convenient way to increase the accuracy through an increase in the degree of the fitting polynomials. Galerkin FEM was used to discretise the pressure and velocity fields in this work. The FE shape functions can be obtained from continuous or discontinuous function spaces. Piecewise-linear discontinuous FE basis functions ($P1_{DG}$) were used to represent velocity in the momentum equation. The continuity equation (for pressure) used piecewise-quadratic continuous FE basis functions (P2). The $P1_{DG}$–P2 velocity–pressure pair ensured the LBB stability criterion (Cotter et al., 2009). See Figure 3 for a comparison between the different discretisations in one and two dimensions.

A node-centred CV discretisation was also used in certain cases (such as for phase volume fraction and PBE scalars) to ensure conservation. Control volume dual mesh was constructed on a P1 parent mesh (as shown in Figure 3) and piecewise-constant CV shape functions were used to discretise fields such as volume fractions, turbulence scalars, DQMOM scalars (in the PBE) and the solids concentrations. Therefore a hybrid FE–CV method was established for the solution of the coupled PDEs for modelling pulp hydrodynamics. See Bhutani et al. (2016) for more details on the description of the discretisation methods.

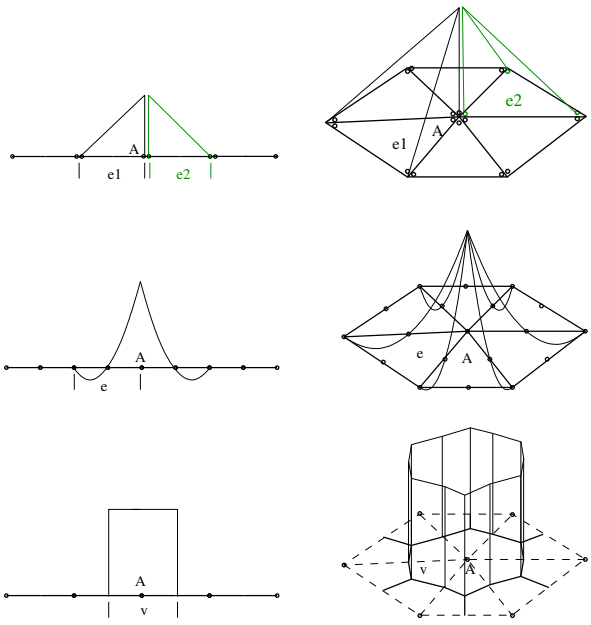

Figure 3: Elements and the corresponding shape functions on 1D (left) and 2D (right) FE meshes. (a) A pair of piecewise-linear discontinuous FE basis functions ($P1_{DG}$) along with the support nodes. (b) Piecewise-quadratic continuous FE basis functions (P2) along with the support nodes. (c) Control volume dual mesh on P1 parent mesh, and piecewise-constant CV shape functions for 1D and 2D are shown. The support for a basis function is the same as the control volume. Figure adapted from Wilson (2009).

Table 2
Comparison of the features of the present pulp phase simulation framework with previous studies.

Model feature	Present work	Koh et al. (2000)	Koh and Schwarz (2003)	Koh and Schwarz (2006)	Koh and Schwarz (2007)	Koh and Schwarz (2008a,b)	Karimi et al. (2014b)	Sarhan et al. (2016, 2018)
E–E model for gas and liquid phases	✓	✓	✓	✓	✓	✓	✓	✓
k–ε turbulence model for liquid phase	✓	✓	✓	✓	✓	✓	✓	✓
Polydisperse bubbles	✓	X	X	X	X	✓	X	✓
Polydisperse solids	✓	X	X	X	X	X	X	X
Settling velocity for free solids	✓	X	✓	✓	✓	✓	X	X
Viscosity modification of liquid phase due to solids	✓	X	X	X	X	✓	X	X
Transport equations for free and attached solids	✓	X	X	✓	✓	✓	✓	✓
Collision rate (bubble–solids)	✓	✓	✓	✓	✓	✓	✓	✓
Collision probability	✓	X	✓	✓	✓	✓	✓	✓
Adhesion probability	✓	X	X	✓	✓	✓	✓	✓
Stabilisation probability	✓	X	X	✓	✓	✓	✓	✓
Detachment rate (bubble–solids)	✓	X	X	✓	✓	✓	✓	✓
Solver	Fluidity	CFX	CFX	CFX	CFX	CFX	ANSYS Fluent	AVL-FIRE
Impeller modelling	X	✓	✓	✓	✓	✓	✓	X

2.5. Mesh adaptivity

Mesh adaptivity is the method of systematic mesh modification in a simulation, based on the physics of the problem, to predict the flow accurately as time progresses. Fluidity can generate fully-unstructured, non-homogeneous, anisotropic meshes adaptively for a given set of optimisation parameters. Considering the many equations that needed to be solved in the model in this work, it was imperative that an optimised mesh be considered for a tractable framework. Mesh adaptivity in Fluidity is a three-step process which starts with metric estimation, followed by mesh generation, and finally the interpolation of all fields on the new mesh.

The mesh metric is a Hessian based error metric which is a function of the curvature of the field to be adapted to and a user-defined interpolation bound. The mesh metric allows for an increase in the mesh resolution in the regions of strongly-varying fields, keeping the mesh in the other parts of the domain coarse. Different mesh metrics can be superposed in case the mesh needs to be adapted to more than one field (Pain et al., 2001). In the next step, the mesh is generated through a sequence of local topological operations (Piggott et al., 2009). Finally, the interpolation of meshes can be achieved using a consistent interpolation method or using a Galerkin projection method. Details on the description of mesh adaptivity and its implementation can be found in the previous work by the authors (Bhutani et al., 2016), the Fluidity manual (AMCG, 2015), Pain et al. (2001), and Piggott et al. (2009). Significant improvements in the solution efficiency have been reported through the use of mesh adaptivity in Fluidity in the past (Hiester et al., 2014; Jacobs et al., 2013)

In the present work the mesh was adapted for the air volume fraction, and the first weight and weighted-abscissa of the NDF. The application of adaptivity to the PBE fields was shown to improve the solution efficiency in the previous work by the authors (Bhutani et al., 2016). Details of the interpolation-error bound values used in this study are discussed in Section 4.

3. Problem description and simulation setup

Turbulence provides the necessary mixing needed in a flotation system to aid in the particle–bubble collision. This turbulence can either be generated using an impeller, such as in a flotation cell, or using gravity resulting in rising buoyant bubbles, such as in a flotation column. In this work a flotation column-like system was modelled using the present Fluidity framework to demonstrate its capabilities.

A rectangular column geometry, as shown in Figure 4, was used for the flotation simulations in this work. This geometry was inspired from the bubble column experiments of Díaz et al. (2008b), which was used as a validation problem in this work. Díaz's 'thin' bubble column measured 20 cm x 45 cm x 4 cm which was approximated with a 20 cm x 45 cm two-dimensional (2D) column in this work. Air was injected into this 2D column through a 2 cm sparger placed symmetrically at the base of the column, as shown in the figure. It was reasonable to approximate Díaz's thin experimental column with a 2D column as the z velocity component is much smaller than the x and y velocity components. The dependence of the fluid flow equations on the z-coordinate can be neglected if one is interested in estimating the flow at the centre z-plane. The acceptability of the above approximation was established through a good match with the bubble column experiments, as shown in Section 4.

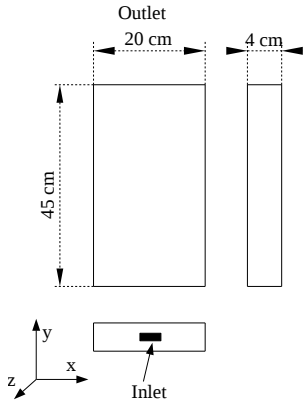

Figure 4: Experimental column of Díaz et al. (2008a) used in this work for model validation. Inlet dimentions are 1.8 cm × 0.6 cm.

Boundary conditions, initial conditions and the numerical and physical parameters used in the simulations are presented next. The values for all fields presented are the same for the bubble column validation problem and the flotation column problem, except for the solids equations which only appear in the flotation simulation.

The Schiller–Naumann (S–N) drag coefficient was used to model the interphase momentum interaction between the gas and liquid phases in this work. Gupta and Roy (2013) compared different drag models for a thin 2D bubble column geometry (similar to the one employed in the present work) with polydisperse bubbles and concluded that the Schiller–Naumann model was good enough to model drag in their bubble column. Although the S–N drag coefficient and similar models were typically developed for rigid single spheres in a dilute laminar flow, the application has been extended to polydisperse bubble population. This drag coefficient (and similar models) has (have) been used extensively over the years to model bubble-water drag successfully (Buwa and Ranade, 2002; Chen et al., 2005; Sanyal et al., 2005; Tabib et al., 2008; Silva et al., 2008; Buffo et al., 2016). The Schiller–Naumann drag coefficient is still popular in the minerals processing literature (Sarhan et al., 2017; Mwandawande et al., 2019; Wang et al., 2019) due to its good match with the standard drag curve (Clift et al., 1978). For the same reason this drag coefficient was employed for the present simulations even though the bubbles under consideration were 5 mm in diameter.

Table 3
BCs for the flow fields. n here denotes the normal coordinate. v denotes the y-component of the velocity.

Flow field	Inlet (sparger)	Walls	Outlet
Continuous phase velocity	v_c=0	no slip (weak)	v_c=0 (weak)
Gas velocity	v_d=0 (weak)	no slip (weak)	v_d=0 (weak)
Pressure	$\frac{\partial p}{\partial n} = 0$	$\frac{\partial p}{\partial n} = 0$	$p = 0$ at coordinate (0,0.45)
Air volume fraction	flux specified	no flux	$\frac{\partial \alpha_d}{\partial n} = 0$ with large absorption
Turbulent kinetic energy	$\frac{\partial k}{\partial n} = 0$	0	$\frac{\partial k}{\partial n} = 0$
Turbulent dissipation	$\frac{\partial \varepsilon}{\partial n} = 0$	$\frac{\partial \varepsilon}{\partial n} = 0$	$\frac{\partial \varepsilon}{\partial n} = 0$

3.1. Boundary conditions

Table 3 shows the boundary conditions for the velocity, pressure, volume fraction and turbulence fields that were used while modelling the bubble column and the flotation column. The superficial gas velocity (SGV) (also known as J_g) was used to calculate the inlet air flux using: gas flux $= \left(\frac{A_{\text{cross-section}}}{A_{\text{sparger}}}\right)$SGV. For the 2D column, $A_{\text{cross-section}}$ and A_{sparger} were equal to 20 cm and 2 cm, respectively. In order to extract the air at the outlet, a special absorption BC was applied for the air volume fraction. A large absorption term in the advection equation for the air volume fraction was implemented as:

$$\frac{\partial \alpha_d}{\partial t} + \nabla \cdot (\alpha_d \mathbf{u}_d) + \sigma_{\text{abs}} \alpha_d = 0, \tag{47}$$

where σ_{abs} is the absorption that was set equal to a very high value close to the outlet and zero otherwise:

$$\sigma_{\text{abs}} = \begin{cases} 10,000 & \text{if } y \geq 0.45, \\ 0 & \text{otherwise.} \end{cases} \tag{48}$$

The large absorption term, in conjunction with a fully-implicit time discretisation for the volume fraction transport equation, ensured that all the air reaching the outlet boundary was removed from the column. It is always tricky to "correctly" specify the outlet BC for the gas phase in a multiphase flow problem (Prosperetti and Tryggvason, 2007) and after trying various options, the above outlet BC was seen to give the expected result for the bubble column in this work. This boundary condition mimics the presence of a large absor ption zone at the outlet, which is more physical than the degassing BC typically employed in commercial codes.

For the PBE, since the number of quadrature points in the DQMOM assumption, N, was taken as 2, there were four unknowns (two weights and two weighted-abscissas) in the DQMOM transport equations. A no-flux BC was applied to the side walls of the column for these four PBE scalars. A homogeneous Neumann BC was applied at the outlet. At the inlet of the column, the incoming bubbles were assumed to be distributed normally with a standard deviation equal to 16% of the mean (Laakkonen et al., 2007; Buffo et al., 2013); this is based on the measurements by Laakkonen et al. (2007). With the definition of the SMD, the relation between the third moment and the bubble volume fraction (for spherical bubbles), and the above two assumptions about the inlet bubble distribution, the four unknown moments, and therefore the DQMOM scalars—w_1, w_2, ς_1 and ς_2—were calculated. The following system of coupled equations was solved for the inlet values of m_0, m_1, m_2 and m_3:

$$m_2 = m_0 \left[m_1^2 + (s.d.)^2\right], \tag{49a}$$

$$m_3 = m_0\, m_1 \left[m_1^2 + 3(s.d.)^2\right], \tag{49b}$$

$$s.d. = 0.16\, d_{32}, \tag{49c}$$

$$\frac{m_3}{m_2} = d_{32} \tag{49d}$$

and

$$m_3 = \alpha_d \left(\frac{6}{\pi}\right), \tag{49e}$$

where d_{32} and α_d are known. The moment inversion product–difference (PD) algorithm (Gordon, 1968) was then applied to obtain the weights and abscissas in the DQMOM approximation. At the inlet, a 5 mm average bubble diameter along with a volume fraction of 0.14 gave the four unknowns as w_1 =1.158 391 $\times 10^6$, w_2 =1.158 391 $\times 10^6$, ς_1 =4.560 935 $\times 10^3$, and ς_2=6.414 361 $\times 10^3$. The inlet volume fraction is a function of the sparger design and was assumed to be 14% gas in this work for the calculation of the PBE scalars. For the walls adjacent to the sparger (the 'lower walls'), a Dirichlet BC was applied for the four PBE scalars corresponding to an average bubble diameter of 1 mm and gas volume fraction of 1.0×10^{-7}, giving w_1 =1.034 281 $\times 10^2$, w_2 =1.034 281 $\times 10^2$, ς_1 =8.144 541 $\times 10^{-2}$, and ς_2=1.145 424 $\times 10^{-1}$. A no-flux BC at the lower walls led to the moment-set getting corrupted causing the scalars to become non-positive. The Dirichlet BC, however, ensured that the PBE scalars remained positive.

A no-flux BC was applied on all the boundaries for the free solids concentration field, whereas the attached solids were allowed to escape from the outlet with the absorption BC applied to them, as discussed in Equation (48).

3.2. Initial conditions

Zero velocity for the two phases was assumed initially with an air volume fraction of 1.0×10^{-7} everywhere. Since the

gas holdup (which is the percentage of gas in the column) increases as the air flows inside the column, the water volume goes down with time, but that decrease was not more than 5% for the maximum gas flow rate in this work. Initial k was taken as 1.0×10^{-7} m^{2}s^{-2} and ε as 1.0×10^{-7} m^{2}s^{-3}. The steady state result for the flow, however, was found to be independent of the initial values of k and ε.

The PBE scalars were calculated from an initial average bubble diameter of 1 mm and a gas volume fraction of 1.0×10^{-7} with the same two assumptions about the bubble number density function as discussed in the BCs. The initial PBE scalar values were therefore identical to the BCs used for the lower walls. The initial condition for the free and attached solids concentration fields are discussed in Section 4.2.

3.3. Physical and numerical parameters

Table 4
Physical parameters used in the simulations.

Physical parameter	**Value**
Continuous phase density ρ_c (kg m^{-3})	998.2
Dispersed phase density ρ_d (kg m^{-3})	1.205
Continuous phase dynamic viscosity μ_c (Pa · s)	0.001
Dispersed phase dynamic viscosity μ_c (Pa · s)	1.254×10^{-5}
Interfacial tension (air–water) σ (N m^{-1})	0.072
Solids density ρ_s (kg m^{-3})	2600
Solids contact angle	75°

The physical parameters chosen in the simulations are presented in Table 4. The constants C_1, C_2 and C_3 in the breakage frequency expression, Equation (24), were 6.0, 0.04 and 0.01, respectively, based on the work of Laakkonen et al. (2007). Buffo et al. (2013) also used the same values for these constants in their rectangular bubble column simulations. Binary breakage was assumed in the present work (same as Laakkonen et al. (2007)) and the value for the parameter C_4 in the daughter distribution function, Equation (25), was therefore taken as 2.0. The value for parameter C_5 in the coalescence frequency relation, Equation (27), was chosen to be 0.88. The value of C_6 in the coalescence efficiency, Equation (26), was 6.0×10^9, based on the work of Laakkonen et al. (2006) and Buffo et al. (2013).

An adaptive time step, with a strict limit on the maximum Courant number of 0.5, was used. Since the simulations were performed using adaptive-mesh simulations, the CFL criterion needed to be satisfied to ensure stability (due to the non-linear nature of the equations). A maximum of two Picard iterations were allowed per time step with a tolerance of 1.0×10^{-12} on the infinity norm of the fields.

The non-linear relaxation parameter θ_{nl} in the turbulence equations was taken to be 1, which allowed for an implicit discretisation of the source terms in the equations for k and ε, and in the expression for μ_T. The non-linear relaxation parameter for the velocities of the two phases was taken as 0.5.

3.4. Discretisations

The first-order upwind scheme was used for discretising the advection terms in all equations due to its conservative and monotonic nature, which ensured stability. The method also ensured that the moment-set obtained in the DQMOM was realisable, as discussed in Section 2.2. The Bassi–Rebay discretisation (Bassi and Rebay, 1997) was applied for the viscous terms in the momentum equations. A fully-implicit time discretisation scheme was used for the transient term in all PDEs. The conservative form of the advection equation was used for the air volume fraction and the PBE scalars to ensure mass conservation, but, as expected, it did not ensure strict boundedness (LeVeque, 2002; Wilson, 2009). Slight artificial diffusion had to be added to the volume fraction equation sometimes to stabilise the scheme.

To maintain positivity and stability, the production term was applied as a source in the k and ε equations whereas the destruction term, which is always negative, was applied as absorption (Patankar, 1980). Numerically it is always effective to have a large absorption coefficient as it supports convergence through under-relaxation. The implementation of the turbulence model was generalised for handling mixed shape functions (discontinuous shape functions for velocity and continuous for turbulence fields) for stability reasons.

The source terms in the PBE were evaluated at the mesh nodes instead of the mesh quadrature points to prevent spatial interpolation errors. These errors were particularly prominent for the current problem due to the discontinuity in the weights and the weighted-abscissas at the inlet at $t = 0$.

4. Results and discussions

In this section, the validation results for Díaz's bubble column (Díaz et al., 2008b) using the present modelling framework are presented first, followed by the flotation simulation results for the same geometry.

Adaptive meshes were used for all simulations in this study. The mesh was adapted to the air volume fraction (α_d), and the first abscissa (ξ_1) and the first weighted-abscissa (ς_1) of the bubble NDF. The corresponding interpolation-error bound values used for the three scalars were: 1.0×10^{-4}, 1.0×10^{-5} m and 100 m, respectively. The mesh was adapted after every 15 time steps. The maximum number of nodes was set to 20000, the minimum and maximum edge lengths being 0.001 m and 0.01 m, respectively. It is evident that the finest mesh was as small as the smallest bubble size in the column. Although it is ideal to have a mesh that allows at least a few dispersed particles per cell, in the present case it is the numerical accuracy that drove the limit on the mesh size. The mesh was adapted 4 times in an adapt cycle for a parallel simulation to compensate

for node locking (AMCG, 2015). The number of initial adapts was set to 6.

The minimum (adaptive) time step size in the highest gas flow rate (SGV=2.0 cm s^{-1}) simulation was 5.2×10^{-4} s. This was due to the CFL criterion with a limit of 0.5 for the maximum Courant number. This is a limitation that is inherent to the adaptive-mesh simulations (Jacobs, 2013). There is always a trade-off between the resolving power of the adaptive simulations and the time step size, as the non-linear fluid flow equations have to be linearised and need an upper bound for the Courant number. A value of the maximum Courant number above 0.6 destabilised the simulation in this case.

4.1. Model validation – bubble column

Bubble columns are two-phase reactors used in the chemical industry for gas–liquid reactions, owing to the high heat and mass transfer rates associated with them. A typical bubble column generally consists of a vertical cylindrical column filled with a liquid, through which the gas is bubbled. The gas bubbles, as they rise due to buoyancy, generate a plume that gets turbulent with height. The mixing caused by this plume-induced turbulence allows for the maximum interphase exchange (of mass, momentum and energy). As the gas flow rate is increased the bubble plume starts oscillating—known as plume oscillation. Bubble columns enjoy many advantages over their counterparts—the stirred reactors—which makes them a suitable candidate as industrial mixers.

The bubble column model in this work was simulated for a range of SGV values between 0.13 cm s^{-1} and 2.0 cm s^{-1}. It was noticed that a steady state was achieved in all simulations. A "cooling tower" flow pattern for water was developed in the column due to the flow of the bubble plume through it, generating the mixing required in such systems. The plume oscillation died as the simulation reached a steady state, and two recirculation zones for water were obtained as a result. This can be seen from the water streamlines plotted in Figure 5.

All bubble column simulation results are presented when the (transient) simulation achieved a steady state. Experiments have reported an oscillating plume (Pfleger et al., 1999; Buwa et al., 2006; Díaz et al., 2008b) and the bubble plume oscillation period (POP) was shown to decrease exponentially with superficial gas velocity. However, in the current simulation using the $k - \varepsilon$ turbulence model, steady state flow was obtained, which was similar to time-averaged flow profiles reported by Díaz et al. (2008a).

Many have claimed to model the unsteadiness in the flow using the $k - \varepsilon$ turbulence model coupled to the Eulerian–Eulerian approach (Díaz et al., 2008a; Pfleger et al., 1999). A similar 2D model was set up in ANSYS Fluent and compared to the present Fluidity model. The turbulent viscosity, which was very small to start with, gradually increased as the simulation progressed and kept increasing until everything became steady. Pfleger et al. (1999) and Sokolichin and Eigenberger (1999)

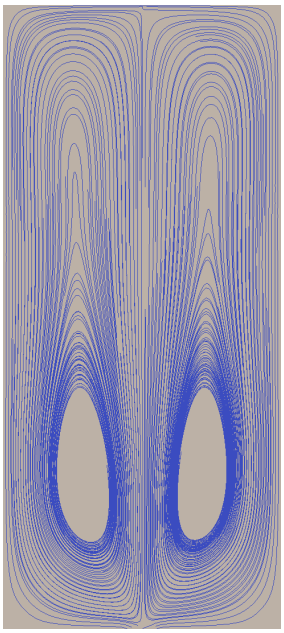

Figure 5: Predicted water streamlines at steady state for a SGV of 0.6 cm s^{-1}.

discussed this effect and concluded that 3D modelling of the columns is necessary to capture the plume oscillations; stating that the 2D models over-predict turbulence to a large extent (5–10 times higher turbulent viscosity) (Pfleger et al., 1999). As per them, the front and back walls in the column dampen the overall TKE allowing the 3D model to show unsteady behaviour. In order to check if the 2D modelling suppressed flow unsteadiness, a 3D column was simulated in Fluent for the exact same physical conditions and it produced similar results with a steady double recirculation zone for water. It was therefore decided to simulate the 2D bubble column as it has been found to model the mean-flow quantities reasonably (Pan et al., 1999) and can be used for model validation. Oey et al. (2003) discussed the effect of the discretisation scheme of the convective terms and suggested that lower-order diffusive schemes, such as the first-order upwind scheme, can cause enough numerical diffusion to suppress the transient terms in the results. However, the QUICK scheme was used with the 3D model in Fluent and as mentioned above, the unsteady plume could not be captured. Table 5 shows a comparison of the present numerical simulations with previous studies from literature in reference to the prediction of flow unsteadiness.

It is believed that an overpredicted eddy viscosity using the k-ε turbulence model could be responsible for suppressing the unsteadiness in the solution. In fact, the time-averaged nature of the RANS turbulence model could be causing the time averaging of the plumes in the flow. Although no plume oscillation was obtained in the numerical simulations in this study, the mean flow quantities obtained in a 2D simulation have been shown to give reasonable match with the experiments (Pan et al., 1999), and the same was used for validation here.

The strong circulation in the interior parts of column for the liquid phase was responsible for providing the shear leading

Table 5
Comparison of the present simulation behaviour with regards to the prediction of the plume oscillation with a few previous studies that used the k-ε model for modelling a rectangular bubble column.

	Model description	Plume oscillation predicted
Present work (Fluidity 2D)	E–E, unstructured mesh, 2D, $\Pi = 0$, $\mu_{T,d} = 0$, drag: Schiller and Naumann (1935), lift: no, VM force: no, Discretisations – FE for space, first-order time, $\Delta t \approx 0.0001$ s, BC – velocity: specified at inlet and outlet, vol frac: flux at inlet and absorption at outlet, walls: no-slip (weak).	no
Present work (Fluent 2D)	E–E, unstructured mesh, 2D, $\Pi = 0$, $\mu_{T,d} = 0$ evaluated from k-ε model for dispersed phase, drag: Schiller and Naumann (1935), lift: no, VM force: no, Discretisations – QUICK for space, first-order time, $\Delta t = 0.01$ s, BC – mass-flow inlet, outlet: degassing, walls: no-slip for liquid and free-slip for gas.	no
Present work (Fluent 3D)	E–E, structured mesh, 3D, $\Pi = 0$, $\mu_{T,d} = 0$ evaluated from k-ε model for dispersed phase, drag: Schiller and Naumann (1935), lift: no, VM force: no, Discretisations – QUICK for space, first-order time, $\Delta t = 0.005$ s, BC – mass-flow inlet, outlet: degassing, walls: no-slip.	no
Díaz et al. (2008a)	E–E, structured mesh, 3D, $\Pi = 0$, $\mu_{T,d}$ specified, drag: Grace et al. (1976), lift: yes, VM force: yes, CFX, Discretisations – second-order upwind for space, first-order time, $\Delta t = 0.025$ s, BC – velocity inlet, outlet: degassing, walls: no-slip for liquid and free-slip for gas.	yes
Buwa and Ranade (2002)	E–E, structured mesh, 3D, $\Pi = 0$, $\mu_{T,d}$ specified, drag: Tsuchiya et al. (1997) and Schiller and Naumann (1935), lift: yes, VM force: yes, Fluent, Discretisations – QUICK + SUPERBEE limiter for space, first-order time, $\Delta t = 0.01$ s, BC – velocity inlet, outlet: velocity specified, walls: no-slip.	yes
Pfleger et al. (1999)	E–E, structured mesh, 3D, $\Pi = 0$, $\mu_{T,d} = 0$, drag: constant, lift: no, VM force: no, CFX, Discretisations – higher-order TVD for space, first-order time, $\Delta t = 0.1$ s, BC – not specified in the paper.	yes

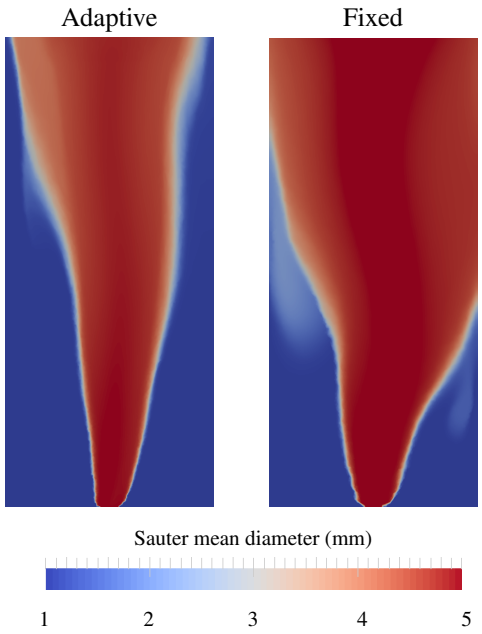

Figure 6: Sauter mean diameter at t = 9.6 s compared for an adaptive-mesh (≈ 19300 nodes) and a fixed-mesh (19347 nodes) for a SGV=0.6 cm s^{-1}.

to turbulence production in the present case. No wall model for turbulence was therefore used in this work as most of the production occurred in the interior of the column.

Figure 6 shows a comparison of the bubble SMD for fixed and adaptive meshes with approximately equal number of nodes for a SGV of 0.6 cm s^{-1}. It can be seen clearly that the adaptive mesh produced better resolved SMD field.

The contour plots of SMD and air volume fraction, and the corresponding adaptive meshes are shown for five time instances: 5 s, 8 s, 11 s, 15 s and 19 s for a SGV of 2.0 cm s^{-1} in Figure 7. It can be seen that the simulations converge to a steady state result and the plume oscillation is only visible in the initial stages. The anisotropy of the mesh is clearly visible with elongated elements close to the boundary of the gas plume. On an 8-core 2.30 GHz Intel Xeon machine, it took 10.5 days to run the SGV=2.0 cm s^{-1} simulation to 63 s. Strong scaling was performed for the bubble column problem and eight cores were found to be the optimum, beyond which the data bandwidth effect started dominating the processing power. Mesh adaptivity and parallelisation can be applied at the same time in Fluidity making it a highly desirable choice for the tractable modelling of multiphase polydisperse flows. The plots for air Sauter mean diameter are presented in Figure 8 at t=19 s . The variation in the bubble diameter is small in the plume for the present case.

To make a comparison of the local field predictions using the current polydisperse flow model, liquid flow field values were compared to the experiments of Pfleger et al. (1999). Their experiments measured the liquid vertical-velocity profile (using laser Doppler velocimetry) at three column heights for a SGV of 0.13 cm s^{-1} for a column of the same dimensions as this work. Simulations for the same SGV were carried out in the present work and the results were compared, as shown in Figure 9. It can be seen that the Fluidity model was able to predict the trend in liquid velocity reasonably. The effect of coalescence and breakage is negligible at such low flow rate and the polydisperse model takes that into account. Díaz et al. (2008a), on the other hand, had to revert to the monodisperse model for low gas flow rates as their polydisperse model was still predicting bubble breakage and coalescence and the results did not agree with the experiments. The agreement in Figure 9 is very good in the lower part of the column as the effect of the absorption outlet condition on the predicted flow parameters fades away in the lower reaches of the column. The under-prediction of the liquid y-velocities in the central zone of the column at h=0.25 m and 0.37 m can be attributed to the outlet boundary condition chosen in the present CFD model, along with the k-ε model potentially adding too much viscosity resulting in the underprediction of liquid velocities. The gas plume flows through the centre of the column and the choice of outlet BC has an effect on the prediction of the plume velocities and therefore the liquid velocities. An exaggerated drag force could also be attributed to the under-predicted liquid velocities in the central zone, however, a decent match close the column edges negates this hypothesis. The agreement can potentially be improved through a the inclusion of non-drag forces and the inclusion of bubble-induced turbulence model. However, since the aim of the present work was to demonstrate a tractable finite-element framework for the modelling of three-phase polydisperse flows, simplified models were chosen.

Gas holdup (or air volume fraction) is a very important global property that is used to characterise the flow regime in a bubble column. A larger gas holdup implies a larger residence time for the gas, implying better mixing. In order to make quantitative comparison of the gas holdup distribution, the experiments of Buwa et al. (2006) were used. They conducted experiments for the same column geometry as Díaz et al. (2008b) for a SGV of 0.73 cm s^{-1} and measured the local gas holdup in the column at a height of 0.37 m. Numerical simulation was carried out for the same SGV in Fluidity and the time-averaged results of Buwa et al. (2006) were compared to the numerical results obtained in the present work, as shown in Figure 10. Bell-shaped curve similar to the experiments are predicted by Fluidity, but the experiments correspond to a slightly more 'diffused' curve. Fluidity over-predicts the gas holdup at the column centre (x=0.1 m) by 20%, under-predicting around the column sides.

To validate the global gas holdup obtained using Fluidity simulations, the experiments of Díaz et al. (2008b) were used for comparisons. Díaz et al. (2008b) used the well-known manometric method to measure the static pressure difference across the column height to obtain the global gas holdup. Figure 11 shows the plot of the gas holdup obtained using the model in Fluidity, compared to the experiments of Díaz et al. (2008b). A good agreement between the experimental values and the numerical predictions can be seen in Figure 11. The expected linear trend in the increase of gas holdup with SGV is also captured to a good extent. At SGV values lower than 0.5 cm s^{-1}

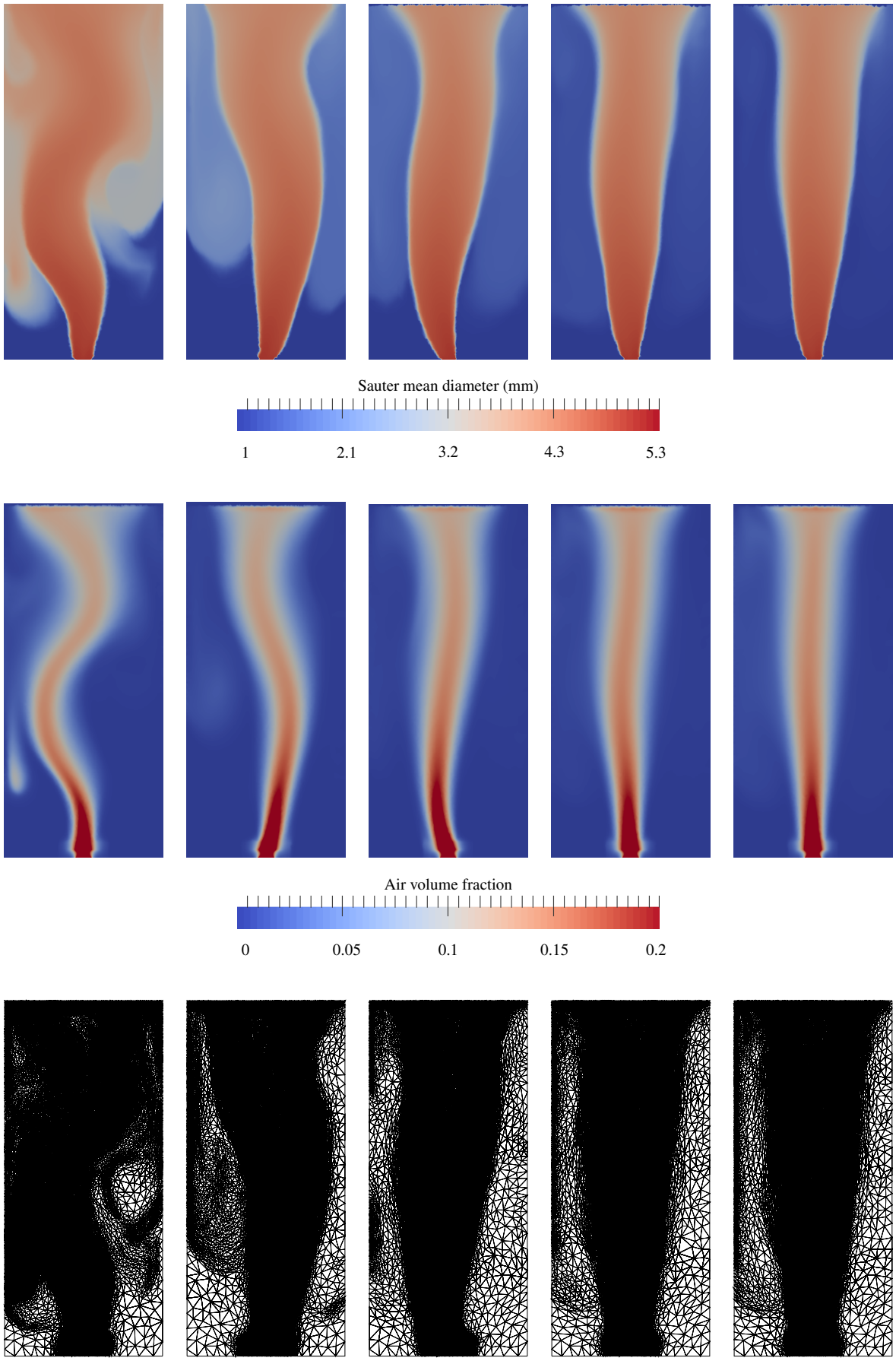

Figure 7: Contours of the bubble SMD and the air volume fraction plotted at five time instances (from left to right: t=5 s, 8 s, 11 s, 15 s and 19 s) for an adaptive-mesh simulation in Fluidity. The SGV was equal to 2.0 cm s^{-1}. Surface meshes are also shown.

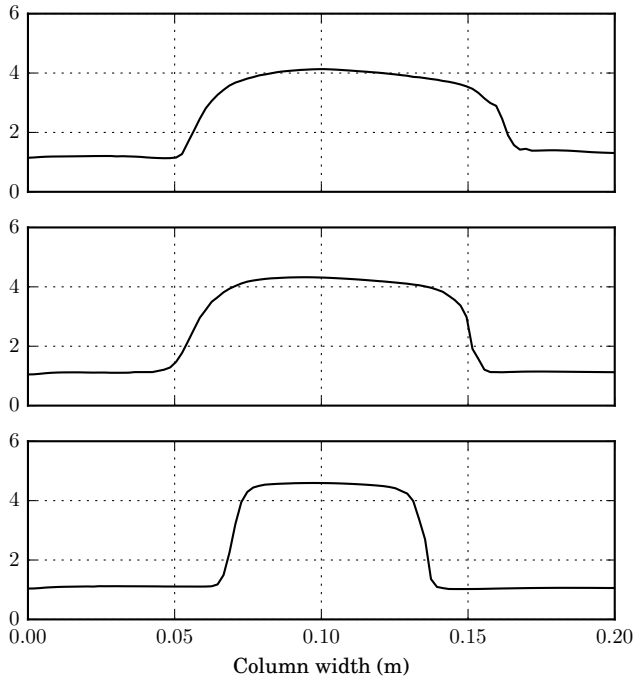

Figure 8: Comparison of the air Sauter mean diameter from Fluidity simulations at three column heights. From bottom to top: h = 0.13 m, 0.25 m and 0.37 m. SGV= 2.0 cm s^{-1}, t=19 s.

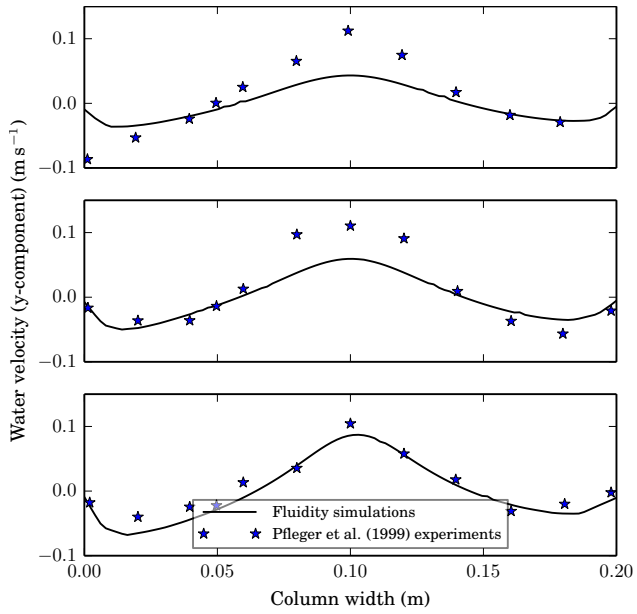

Figure 9: Comparison of the water vertical-velocity profiles between Fluidity simulations and the experiments performed by Pfleger et al. (1999) at three column heights. From bottom to top: h = 0.13 m, 0.25 m and 0.37 m. Steady state simulation results are compared with time-averaged experimental results. SGV= 0.13 cm s^{-1}.

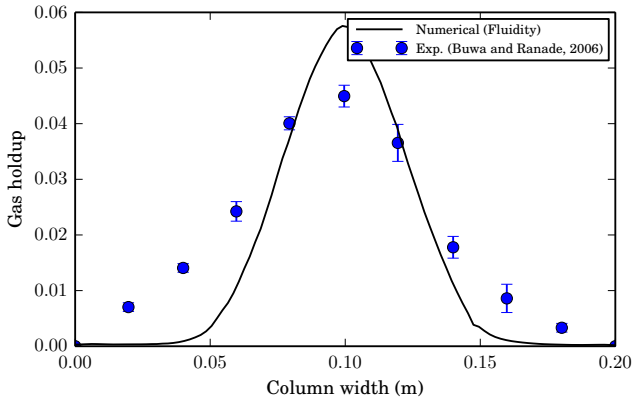

Figure 10: Gas holdup comparisons between the experiments of Buwa et al. (2006) and polydisperse Fluidity simulations. Values are plotted for a SGV of 0.73 cm s^{-1} at a height of 0.37 m in the column.

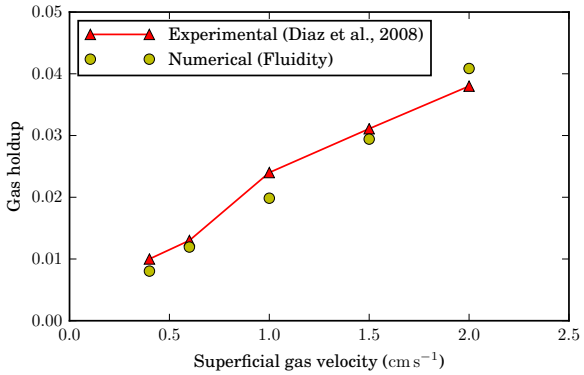

Figure 11: Gas holdup plotted as a function of the superficial gas velocity. The numerical results are compared to the experiments of Díaz et al. (2008b).

there is not much coalescence or breakage that occurs in the column and the model predicts a good gas holdup for these values of SGV. The kernels chosen in this work ensured that they did not predict any false coalescence or breakage at low turbulence values in the column at the lower values of the SGV.

The validation results presented in this section show a reasonable match with the experiments. The chosen models for the interphase drag force term, bubble breakage and coalescence kernels, and the inlet size distribution of bubbles were good enough to extend the bubble column model to a flotation column model through the introduction of solids.

4.2. Flotation column

The two-phase bubble column was allowed to attain a steady state after which the solid particles were introduced into it. Two simulation results are presented in this section, one for monodisperse solids and another for polydisperse solids. Previous pulp phase models by Koh and Schwarz (2007, 2008b) have considered monodisperse particles for simplicity. However, the feed entering the flotation process in reality is in the form of a particle size distribution and the model should be able to consider this polydispersity of the solids for an accurate modelling

of the overall process. For this reason a polydisperse solids simulation was run in this work and the results were compared to a monodisperse simulation to notice if the polydisperse modelling of solids has any effect on the rate of flotation. Both simulations were run for a superficial gas velocity of 1.0 cm s^{-1}. The monodisperse solids simulation consisted of 150 µm spherical solid particles with an initial concentration of 15% by volume (which is equal to 39% solids by mass for the present case). The corresponding initial condition for the free solids, n_f, was 8.25×10^{10} m^{-3}. All the particles were assumed to be free in the beginning and hence the initial concentration for the attached solids was taken as 1.0×10^{-7} m^{-3}. For the polydisperse simulation, three solid sizes were considered—50 µm, 150 µm and 250 µm. Initial concentration for each solid class was 5% by volume, which corresponded to an initial concentration of 7.5×10^{11} m^{-3}, 2.75×10^{10} m^{-3} and 6.0×10^{9} m^{-3} for the free solids of the three size classes, respectively.

4.2.1. Evolution of solid concentration

Figure 12 shows the total number of free particles of 150 µm size as a function of time in the polydisperse simulation. A linear decrease in the free particle population in the column was obtained in the 100 s simulation time. This decrease is due to the particles getting attached to bubbles and the loaded bubbles getting transported out of the batch flotation column. Figure 13 shows the total number of attached particles of 150 µm diameter in the polydisperse column as a function of time. It can be seen that the attached particles attain a steady state value in a very short time. This means that the rate of attachment becomes equal to the rate of transport of the attached particles out of the column. Koh and Schwarz (2006) also reported the number of attached particles becoming constant with time and the bubbles getting loaded very quickly in their pulp phase simulations for an impeller-driven cell. The rate of detachment was negligible for the simulation conditions in this work. Since the overall number of attached particles was constant and the detachment was negligible, the transport rate is what determined the rate of flotation here, similar to the findings of Koh and Schwarz (2006). Figure 14 shows the contours of the attached solids concentration in the column at steady state for the 150 µm particles in the polydisperse solids simulation. It can be seen that the attached particle concentration is higher near the inlet as compared to other sections in the column. The turbulent dissipation, which affects the collision rate, was also found to be high near the inlet of the column and may be the reason behind the increased attached particle concentration in that region.

4.2.2. Effect of polydispersity of solids

The particle volume fraction remaining in the column as a function of time is plotted in Figure 15 for the three solid sizes. Flotation rate, which is proportional to the negative of the slope of the curves, increases with particle size, as shown in the figure. Larger particles have a higher chance to come in contact with a bubble leading to higher collision rate. Although larger

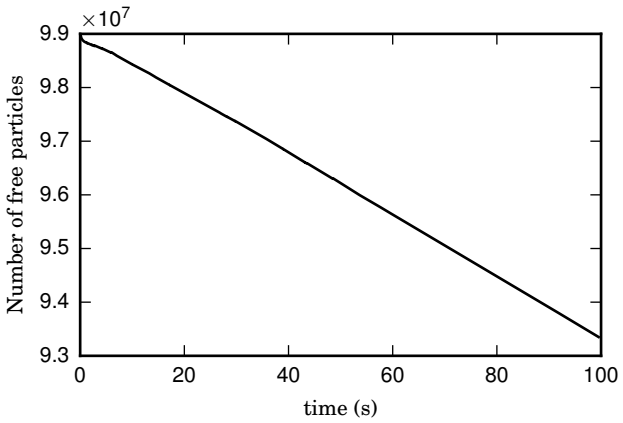

Figure 12: The total number of free particles (of 150 µm diameter) in the column as a function of time for the polydisperse solids simulation.

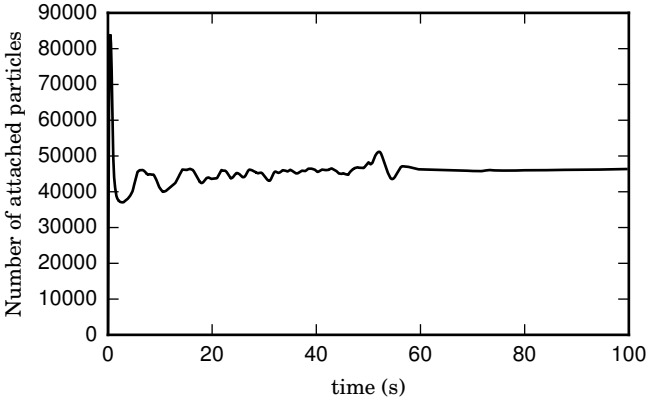

Figure 13: The total number of attached particles (of 150 µm diameter) in the column as a function of time for the polydisperse solids simulation.

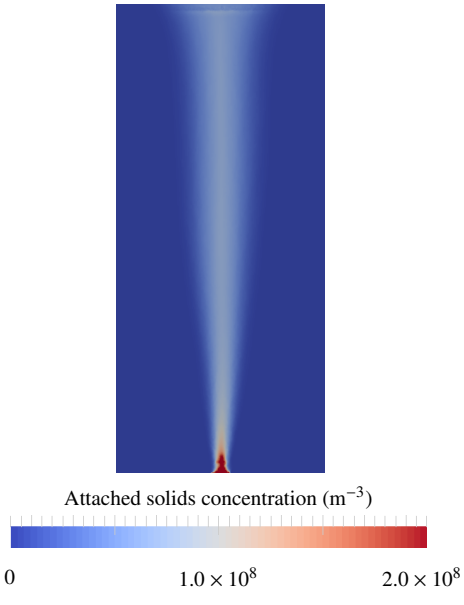

Figure 14: Steady state contours of the attached particles (of 150 µm size) in the polydisperse solids simulation.

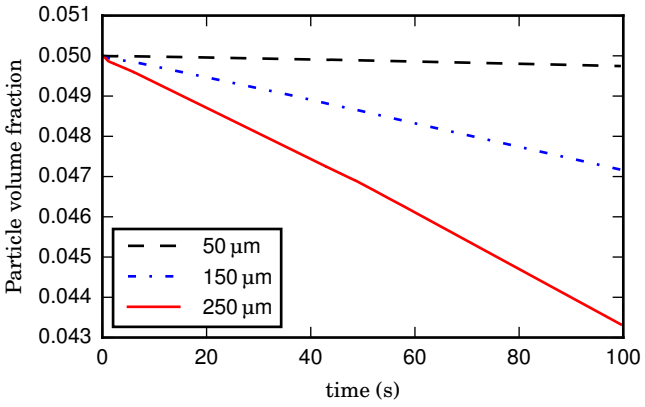

Figure 15: Particle volume fraction remaining in the flotation column plotted as a function of time for polydiperse mineral particles. Three particle diameter classes in the column were simulated with an initial volume fraction for each class equal to 0.05. J_g (or SGV) = 1.0 cm s^{-1}.

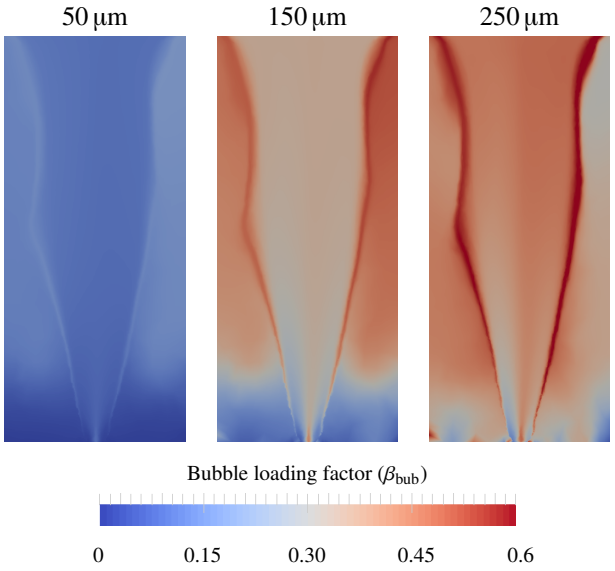

Figure 16: Contours of the bubble loading factor (β_{bub}) for the three solid sizes.

particles have higher destabilisation rates, the current expression for the probability of stabilisation and the current operating conditions resulted in a destabilisation rate close to zero. The bubble loading factor (β_{bub}) for the three solid sizes are compared in Figure 16. For the lower and intermediate particle sizes, the bubble loading is higher outside the central plume owing to the smaller number of bubbles in that region. The lower bubble loading corresponding to the smaller particle sizes supports the fact that attachment is more dominant for larger particles in this case.

Figure 17 shows a comparison of the total volume fraction of particles remaining in the column as a function of time for the monodisperse and the polydisperse simulations. The monodisperse solids simulation over-predicts the flotation rate as compared to the polydisperse simulation. Although the difference is only around 3.5% in the first 100 seconds, the linear trend

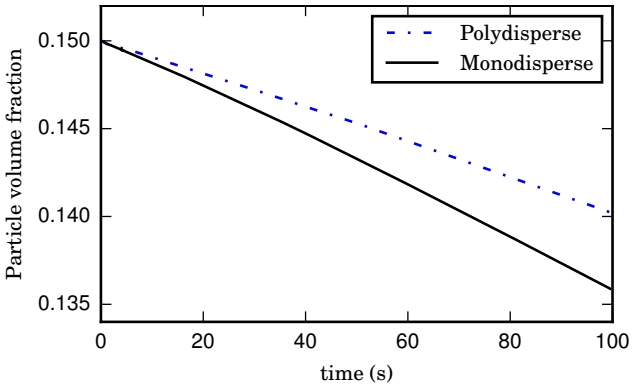

Figure 17: Comparison of the volume fraction of particles remaining in the column with time between monodisperse and polydisperse solids. The results have been compared for all particle sizes with a total initial solid volume fraction of 0.15 and a J_g of 1.0 cm s^{-1}.

could lead to an increasing over-prediction of the flotation rate with time. The overall higher flotation rate prediction in this case was due to the larger particles having a higher flotation rate overpowering the smallest ones. The over/underprediction of flotation rate for polydisperse system may depend on the nature of the flotation rates of the different particle sizes. This may imply that modelling the polydispersity of the solids is important for the correct prediction of flotation rate through CFD simulation of the pulp phase in a flotation column.

5. Conclusions

An efficient numerical framework for the modelling of the polydisperse pulp phase in froth flotation has been developed and presented in this paper. The absence of a comprehensive model for the pulp phase in the literature was the inspiration behind this work. The focus of this research was the modelling of the polydispersity of gas and solid phases and ensuring the tractability of the solution framework. Bubble polydispersity was modelled using the population balance equation that was implemented in Fluidity using DQMOM. Mesh adaptivity and code parallelisation features of Fluidity imparted tractability to the overall solution method. This study validated the polydisperse model solved for the bubbles (using the PBE) in a bubble column for a reasonable prediction of the flow hydrodynamics. Polydispersity of the solids was modelled for the first time by solving different equations for the solid classes. The effect of modelling the polydispersity of solids on the overall flotation rate prediction was also demonstrated.

Incompressible E–E momentum equations were solved for the gas and liquid phases, with a PBE to estimate the change in the bubble size due to breakage and coalescence in the pulp phase in a flotation column. A k-ε turbulence model was solved for the liquid phase, and the solids were modelled using scalar transport equations. The transport equations for free and attached particles were coupled through the attachment and detachment source terms. For the modelling of the pulp phase,

care was taken to modify the liquid viscosity in the momentum equations to account for the presence of free solids, and apply a settling velocity for the heavy particles in the free solids transport equation. The PBE for gas bubbles supplied bubble diameter and bubble concentration for attachment and detachment rate expressions in the solids transport equations. A quadrature-based moment method was used to solve the PBE for bubbles in a flotation system.

The Galerkin FEM was used to discretise the velocity and pressure fields in the momentum and pressure equations, respectively, and the $P1_{DG}$–P2 scheme was found to be the most stable for this purpose. For the other fields (such as PBE scalars, volume fraction, etc.), where conservation was required, a node-centred CV discretisation was employed. Therefore, a hybrid FE–CV method was found to be the most effective for simulating polydisperse multiphase flows. To the best of the authors' knowledge, this is the only framework that is capable of modelling the pulp zone using a hybrid FE–CV method.

The mesh was optimised as the solution progressed by generating fully-unstructured, non-homogeneous, anisotropic meshes adaptively for a given set of optimisation parameters—air volume fraction and PBE scalars. For the bubble column validation problem, adaptivity was shown to resolve the SMD field more accurately when compared to a similar fixed mesh. Mesh adaptivity was used for the first time in the modelling of the pulp phase in this paper. Moreover, Fluidity is the only framework that allows mesh adaptivity in the external coordinates of the PBE for modelling polydisperse flows.

The results from the 2D simulations performed using the polydisperse adaptive-mesh FE framework of Fluidity were compared to bubble column experiments in the literature. Although the steady-state results obtained for the flow profiles using Fluidity were not ideal due to the missing plume oscillations, they still showed a good match with the time-averaged local and global flow properties, as was seen for the validation comparisons for liquid velocity and gas holdup in the experiments by Díaz et al. (2008b), Buwa et al. (2006) and Pfleger et al. (1999).

The pulp phase was modelled for three solids classes and the overall flotation rate was compared to the monodisperse solids simulation. The flotation rate was found to increase with the particle size due to the probability of destabilisation being close to zero for the selected conditions; in reality the probability of destabilisation will play a role for very coarse particles. The monodisperse simulations were found to over-predict the flotation rate as compared to the polydisperse simulations. A difference of 3.5% in flotation recovery was noticed at a simulation time of 100 s for a J_g of $1.0\,\mathrm{cm\,s^{-1}}$. This error from neglecting the polydispersity of solids in the pulp phase is expected to add up in time and possibly lead to significant error in flotation recovery estimations. This research therefore confirmed the importance of modelling the polydispersity of dispersed phases in bubble and flotation columns for an accurate prediction of the flow and the flotation rate, respectively. It was also shown that a hybrid FE–CV framework can be successfully used for modelling such a complex system (the pulp phase), which had only been attempted in the past using the control volume codes (Koh and Schwarz, 2006, 2007, 2008b; Sarhan et al., 2016, 2018).

This modelling framework can be applied to simulate a variety of multiphase polydisperse problems in the process industries other than froth flotation. The framework can be used to test the effect of different physical models for dispersed phase interactions on the system hydrodynamics.

The framework can be enhanced by adding complexity in different fronts, which the authors plan to address in the future. These include the implementation of advanced turbulence models such as LES, interphase interaction models such as lift and virtual mass forces, various drag force correlations relevant to non-spherical bubbles, other improved models for bubble–particle detachment (Wang et al., 2016), the use of multivariate PBE for modelling the solids in the pulp phase (Bhutani and Brito-Parada, 2017), and the integration of the froth phase (Brito-Parada et al., 2012a,b) and pulp phase models.

Acknowledgements

We would like to thank Rio Tinto for funding this research. We would also like to thank the Applied Modelling and Computation Group (AMCG) at Imperial College London for their support with the open-source Fluidity code, as well as the Imperial College High Performance Computing (HPC) facility for providing with the computing resources to carry out this research.

References

Abrahamson, J., 1975. Collision rates of small particles in a vigorously turbulent fluid. Chemical Engineering Science 30 (11), 1371–1379.

Albijanic, B., Amini, E., Wightman, E., Ozdemir, O., Nguyen, A. V., Bradshaw, D. J., 2011. A relationship between the bubble–particle attachment time and the mineralogy of a copper–sulphide ore. Minerals Engineering 24 (12), 1335–1339.

AMCG, April 2015. Fluidity manual v4.1.12. Imperial College London. URL `http://dx.doi.org/10.6084/m9.figshare.1387713`

Andersson, R., Andersson, B., 2006. On the breakup of fluid particles in turbulent flows. AIChE journal 52 (6), 2020–2030.

Bannari, R., Kerdouss, F., Selma, B., Bannari, A., Proulx, P., 2008. Three-dimensional mathematical modeling of dispersed two-phase flow using class method of population balance in bubble columns. Computers and Chemical Engineering 32, 3224–3237.

Basavarajappa, M., Alopaeus, V., Yoon, R.-H., Miskovic, S., 2017. A high-order moment-conserving method of classes (HMMC) based population balance model for mechanical flotation cells. Minerals Engineering 108, 36–52.

Basavarajappa, M., Miskovic, S., 2015. Gas dispersion characteristics in lab-scale flotation cell using coupled CFD-PBM quadrature based moment method. In: 5th International Symposium on Computational Modelling. Falmouth, UK.

Bassi, F., Rebay, S., 1997. A high-order accurate discontinuous finite element method for the numerical solution of the compressible Navier–Stokes equations. Journal of Computational Physics 131 (2), 267–279.

Bhole, M. R., Joshi, J. B., Ramkrishna, D., 2008. CFD simulation of bubble columns incorporating population balance modeling. Chemical Engineering Science 63 (8), 2267–2282.

Bhutani, G., 2016. Numerical modelling of polydispersed flows using an adaptive-mesh finite element method with application to froth flotation. Ph.D. thesis, Imperial College London.

Bhutani, G., Brito-Parada, P. R., 2017. Analytical solution for a three-dimensional non-homogeneous bivariate population balance equation—a special case. International Journal of Multiphase Flow 89, 413–416.

Bhutani, G., Brito-Parada, P. R., Cilliers, J. J., 2016. Polydispersed flow modelling using population balances in an adaptive mesh finite element framework. Computers and Chemical Engineering 87, 208–225.

Bloom, F., Heindel, T. J., 1997. A theoretical model of flotation deinking efficiency. Journal of Colloid and Interface Science 190 (1), 182–197.

Bloom, F., Heindel, T. J., 2002. On the structure of collision and detachment frequencies in flotation models. Chemical Engineering Science 57 (13), 2467–2473.

Bloom, F., Heindel, T. J., 2003. Modeling flotation separation in a semi-batch process. Chemical Engineering Science 58 (2), 353–365.

Brito-Parada, P. R., Kramer, S. C., Wilson, C. R., Pain, C. C., Neethling, S. J., Cilliers, J. J., 2012a. A finite element formulation to model the flow of flotation foams. Chemical Engineering Science 69 (1), 279–286.

Brito-Parada, P. R., Neethling, S. J., Cilliers, J. J., 2012b. The advantages of using mesh adaptivity when modelling the drainage of liquid in froths. Minerals Engineering 33, 80–86.

Buffo, A., Alopaeus, V., 2016. Solution of bivariate population balance equations with high-order moment-conserving method of classes. Computers and Chemical Engineering 87, 111–124.

Buffo, A., Marchisio, D. L., Vanni, M., Renze, P., 2013. Simulation of polydisperse multiphase systems using population balances and example application to bubbly flows. Chemical Engineering Research and Design 91 (10), 1859–1875.

Buffo, A., Vanni, M., Renze, P., Marchisio, D., 2016. Empirical drag closure for polydisperse gas–liquid systems in bubbly flow regime: Bubble swarm and micro-scale turbulence. Chemical Engineering Research and Design 113, 284–303.

Buwa, V. V., Deo, D. S., Ranade, V. V., 2006. Eulerian–Lagrangian simulations of unsteady gas–liquid flows in bubble columns. International Journal of Multiphase Flow 32 (7), 864–885.

Buwa, V. V., Ranade, V. V., 2002. Dynamics of gas–liquid flow in a rectangular bubble column: Experiments and single/multi-group CFD simulations. Chemical Engineering Science 57 (22), 4715–4736.

Chen, P., Sanyal, J., Duduković, M. P., 2004. CFD modeling of bubble columns flows: implementation of population balance. Chemical Engineering Science 59, 5201–5207.

Chen, P., Sanyal, J., Duduković, M. P., 2005. Numerical simulation of bubble columns flows: Effect of different breakup and coalescence closures. Chemical Engineering Science 60 (4), 1085–1101.

Clift, R., Grace, J. R., Weber, M. E., 1978. Bubbles, drops, and particles. Dover Publications, Inc., Mineola, New York.

Cotter, C. J., Ham, D. A., Pain, C. C., 2009. A mixed discontinuous/continuous finite element pair for shallow-water ocean modelling. Ocean Modelling 26 (1), 86–90.

Coulaloglou, C. A., Tavlarides, L. L., 1977. Description of interaction processes in agitated liquid-liquid dispersions. Chemical Engineering Science 32 (11), 1289–1297.

Dai, Z., Fornasiero, D., Ralston, J., 1999. Particle–bubble attachment in mineral flotation. Journal of Colloid and Interface Science 217 (1), 70–76.

Desjardins, O., Fox, R. O., Villedieu, P., 2008. A quadrature-based moment method for dilute fluid-particle flows. Journal of Computational Physics 227 (4), 2514–2539.

Díaz, M. E., Iranzo, A., Cuadra, D., Barbero, R., Montes, F. J., Galán, M. A., 2008a. Numerical simulation of the gas–liquid flow in a laboratory scale bubble column: Influence of bubble size distribution and non-drag forces. Chemical Engineering Journal 139 (2), 363–379.

Díaz, M. E., Montes, F. J., Galán, M. A., 2008b. Experimental study of the transition between unsteady flow regimes in a partially aerated two-dimensional bubble column. Chemical Engineering and Processing: Process Intensification 47 (9), 1867–1876.

Evans, G. M., Doroodchi, E., Lane, G. L., Koh, P. T. L., Schwarz, M. P., 2008. Mixing and gas dispersion in mineral flotation cells. Chemical Engineering Research and Design 86 (12), 1350–1362.

Garcia-Zuñiga, H., 1935. La eficiencia de la flotación es una función exponencial del tiempo. Boletín Minero Sociedad Nacional de Minería 47, 83–86.

Gaudin, A. M., 1932. Flotation. McGraw-Hill, New York.

Gorain, B. K., Franzidis, J.-P., Manlapig, E. V., 1995. Studies on impeller type, impeller speed and air flow rate in an industrial scale flotation cell. Part 1: Effect on bubble size distribution. Minerals Engineering 8 (6), 615–635.

Gordon, R. G., 1968. Error bounds in equilibrium statistical mechanics. Journal of Mathematical Physics 9, 655.

Grace, J. R., Wairegi, T., Nguyen, T. H., 1976. Shapes and velocities of single drops and bubbles moving freely through immiscible liquids. Chemical Engineering Research and Design 54a, 167–173.

Grevskott, S., Sannæs, B. H., Duduković, M. P., Hjarbo, K. W., Svendsen, H. F., 1996. Liquid circulation, bubble size distributions, and solids movement in two- and three-phase bubble columns. Chemical Engineering Science 51 (10), 1703–1713.

Gupta, A., Roy, S., 2013. Euler–Euler simulation of bubbly flow in a rectangular bubble column: Experimental validation with Radioactive Particle Tracking. Chemical Engineering Journal 225, 818–836.

Hiester, H. R., Piggott, M. D., Farrell, P. E., Allison, P. A., 2014. Assessment of spurious mixing in adaptive mesh simulations of the two-dimensional lock-exchange. Ocean Modelling 73, 30–44.

Ishii, M., Hibiki, T., 2010. Thermo-fluid dynamics of two-phase flow, 2nd Edition. Springer, New York.

Jacobs, C. T., 2013. Modelling of multiphase flows on adaptive unstructured meshes with applications to the dynamics of volcanic ash plumes. Ph.D. thesis, Imperial College London.

Jacobs, C. T., Collins, G. S., Piggott, M. D., Kramer, S. C., Wilson, C. R. G., 2013. Multiphase flow modelling of volcanic ash particle settling in water using adaptive unstructured meshes. Geophysical Journal International 192 (2), 647–665.

Jameson, G. J., 2012. The effect of surface liberation and particle size on flotation rate constants. Minerals Engineering 36–38, 132–137.

Jones, W. P., Launder, B. E., 1973. The calculation of low-Reynolds-number phenomena with a two-equation model of turbulence. International Journal of Heat and Mass Transfer 16 (6), 1119–1130.

Karimi, M., Akdogan, G., Bradshaw, S. M., 2014a. A CFD-kinetic model for the flotation rate constant, Part II: Model validation. Minerals Engineering 69, 205–213.

Karimi, M., Akdogan, G., Bradshaw, S. M., 2014b. A computational fluid dynamics model for the flotation rate constant, Part I: Model development. Minerals Engineering 69, 214–222.

Koh, P. T. L., Manickam, M., Schwarz, M. P., 2000. CFD simulation of bubble-particle collisions in mineral flotation cells. Minerals Engineering 13 (14), 1455–1463.

Koh, P. T. L., Schwarz, M. P., 2003. CFD modelling of bubble–particle collision rates and efficiencies in a flotation cell. Minerals Engineering 16 (11), 1055–1059.

Koh, P. T. L., Schwarz, M. P., 2006. CFD modelling of bubble–particle attachments in flotation cells. Minerals Engineering 19 (6), 619–626.

Koh, P. T. L., Schwarz, M. P., 2007. CFD model of a self-aerating flotation cell. International Journal of Mineral Processing 85 (1), 16–24.

Koh, P. T. L., Schwarz, M. P., 2008a. Computational fluid dynamics modelling of slimes flotation at mt keith operations. Metallurgical Plant Design and Operating Strategies, MetPlant.

Koh, P. T. L., Schwarz, M. P., 2008b. Modelling attachment rates of multi-sized bubbles with particles in a flotation cell. Minerals Engineering 21 (12), 989–993.

Koh, P. T. L., Schwarz, M. P., 2009. CFD models of Microcel and Jameson flotation cells. In: Seventh International Conference on CFD in the Minerals and Process Industries. Melbourne, Australia.

Krieger, I. M., Dougherty, T. J., 1959. A mechanism for non-Newtonian flow in suspensions of rigid spheres. Transactions of The Society of Rheology 3, 137–152.

Laakkonen, M., Alopaeus, V., Aittamaa, J., 2006. Validation of bubble breakage, coalescence and mass transfer models for gas–liquid dispersion in agitated vessel. Chemical Engineering Science 61 (1), 218–228.

Laakkonen, M., Moilanen, P., Alopaeus, V., Aittamaa, J., 2007. Modelling local bubble size distributions in agitated vessels. Chemical Engineering Science 62 (3), 721–740.

Launder, B. E., Sharma, B. I., 1974. Application of the energy-dissipation model of turbulence to the calculation of flow near a spinning disc. Letters in Heat and Mass Transfer 1 (2), 131–137.

LeVeque, R. J., 2002. Finite volume methods for hyperbolic problems. Cam-

bridge University Press, Cambridge.
Luo, H., Svendsen, H. F., 1996. Theoretical model for drop and bubble breakup in turbulent dispersions. AIChE Journal 42 (5), 1225–1233.
Marchal, P., David, R., Klein, J. P., Villermaux, J., 1988. Crystallization and precipitation engineering—I. An efficient method for solving population balance in crystallization with agglomeration. Chemical Engineering Science 43 (1), 59–67.
Marchisio, D., Vigil, R., Fox, R., 2003a. Implementation of the quadrature method of moments in CFD codes for aggregation–breakage problems. Chemical Engineering Science 58 (15), 3337–3351.
Marchisio, D. L., Fox, R. O., 2005. Solution of population balance equations using the direct quadrature method of moments. Journal of Aerosol Science 36 (1), 43–73.
Marchisio, D. L., Fox, R. O., 2013. Computational models for polydisperse particulate and multiphase systems. Cambridge University Press, Cambridge.
Marchisio, D. L., Vigil, R. D., Fox, R. O., 2003b. Quadrature method of moments for aggregation–breakage processes. Journal of Colloid and Interface Science 258 (2), 322–334.
Mazzei, L., Marchisio, D. L., Lettieri, P., 2012. New quadrature-based moment method for the mixing of inert polydisperse fluidized powders in commercial CFD codes. AIChE Journal 58 (10), 3054–3069.
McGraw, R., 1997. Description of aerosol dynamics by the quadrature method of moments. Aerosol Science and Technology 27 (2), 255–265.
Merve Genc, A., Kilickaplan, I., Laskowski, J. S., 2012. Effect of pulp rheology on flotation of nickel sulphide ore with fibrous gangue particles. Canadian Metallurgical Quarterly 51 (4), 368–375.
Mwandawande, I., Akdogan, G., Bradshaw, S., Karimi, M., Snyders, N., 2019. Prediction of gas holdup in a column flotation cell using computational fluid dynamics (CFD). Journal of the Southern African Institute of Mining and Metallurgy 119 (1), 81–95.
Oey, R. S., Mudde, R. F., van den Akker, H. E. A., 2003. Sensitivity study on interfacial closure laws in two-fluid bubbly flow simulations. AIChE journal 49 (7), 1621–1636.
Ojima, S., Hayashi, K., Hosokawa, S., Tomiyama, A., 2014. Distributions of void fraction and liquid velocity in air–water bubble column. International Journal of Multiphase Flow 67, 111–121.
Olmos, E., Gentric, C., Midoux, N., 2003. Numerical description of flow regime transitions in bubble column reactors by a multiple gas phase model. Chemical Engineering Science 58 (10), 2113–2121.
Pain, C. C., Umpleby, A. P., de Oliveira, C. R. E., Goddard, A. J. H., 2001. Tetrahedral mesh optimisation and adaptivity for steady-state and transient finite element calculations. Computer Methods in Applied Mechanics and Engineering 190 (29), 3771–3796.
Pan, Y., Dudukovi ć, M. P., Chang, M., 1999. Dynamic simulation of bubbly flow in bubble columns. Chemical Engineering Science 54 (13), 2481–2489.
Patankar, S. V., 1980. Numerical heat transfer and fluid flow. CRC press, Boca Raton, Florida.
Petitti, M., Nasuti, A., Marchisio, D. L., Vanni, M., Baldi, G., Mancini, N., Podenzani, F., 2010. Bubble size distribution modeling in stirred gas–liquid reactors with QMOM augmented by a new correction algorithm. AIChE Journal 56 (1), 36–53.
Pfleger, D., Becker, S., 2001. Modelling and simulation of the dynamic flow behaviour in a bubble column. Chemical Engineering Science 56 (4), 1737–1747.
Pfleger, D., Gomes, S., Gilbert, N., Wagner, H.-G., 1999. Hydrodynamic simulations of laboratory scale bubble columns fundamental studies of the Eulerian–Eulerian modelling approach. Chemical Engineering Science 54 (21), 5091–5099.
Piggott, M. D., Farrell, P. E., Wilson, C. R., Gorman, G. J., Pain, C. C., 2009. Anisotropic mesh adaptivity for multi-scale ocean modelling. Philosophical Transactions of the Royal Society of London A: Mathematical, Physical and Engineering Sciences 367 (1907), 4591–4611.
Prince, M., Blanch, H., 1990. Bubble coalescence and break-up in air-sparged bubble columns. AIChE Journal 36 (10), 1485–1499.
Prosperetti, A., Tryggvason, G., 2007. Computational methods for multiphase flow. Cambridge University Press, Cambridge.
Ramkrishna, D., 2000. Population balances: Theory and applications to particulate systems in engineering. Academic press, San Diego.
Ranade, V. V., 1997. Modelling of turbulent flow in a bubble column reactor. Chemical Engineering Research and Design 75 (1), 14–23.
Richardson, J. F., Zaki, W. N., 1954. The sedimentation of a suspension of uniform spheres under conditions of viscous flow. Chemical Engineering Science 3 (2), 65–73.
Saffman, P. G., Turner, J. S., 1956. On the collision of drops in turbulent clouds. Journal of Fluid Mechanics 1 (1), 16–30.
Sanyal, J., Marchisio, D. L., Fox, R. O., Dhanasekharan, K., 2005. On the comparison between population balance models for CFD simulation of bubble columns. Industrial and Engineering Chemistry Research 44 (14), 5063–5072.
Sarhan, A. R., Naser, J., Brooks, G., 2016. CFD simulation on influence of suspended solid particles on bubbles' coalescence rate in flotation cell. International Journal of Mineral Processing 146, 54–64.
Sarhan, A. R., Naser, J., Brooks, G., 2017. CFD analysis of solid particles properties effect in three-phase flotation column. Separation and Purification Technology 185, 1–9.
Sarhan, A. R., Naser, J., Brooks, G., 2018. CFD model simulation of bubble surface area flux in flotation column reactor in presence of minerals. International Journal of Mining Science and Technology 28, 999–1007.
Sato, Y., Sekoguchi, K., 1975. Liquid velocity distribution in two-phase bubble flow. International Journal of Multiphase Flow 2 (1), 79–95.
Schiller, L., Naumann, Z., 1935. A drag coefficient correlation. Vdi Zeitung 77 (318), 51.
Schulze, H. J., 1993. Flotation as a heterocoagulation process: Possibilities of calculating the probability of flotation. In: Dobíaš, B. (Ed.), Coagulation and Flocculation: Theory and Applications. Vol. 47. Marcel Dekker, Inc., New York, Ch. 7, pp. 321–.
Schwarz, M. P., Koh, P. T. L., Verrelli, D. I., Feng, Y., 2016. Sequential multiscale modelling of mineral processing operations, with application to flotation cells. Minerals Engineering 90, 2–16.
Shook, C. A., Roco, M. C., 1991. Slurry flow: principles and practice. Butterworth-Heinemann, Oxford.
Silva, L. F. L. R., Damian, R. B., Lage, P. L. C., 2008. Implementation and analysis of numerical solution of the population balance equation in CFD packages. Computers and Chemical Engineering 32 (12), 2933–2945.
Smoluchowski, M. V., 1917. Grundriß der koagulationskinetik kolloider lösungen. Colloid and Polymer Science 21 (3), 98–104.
Sokolichin, A., Eigenberger, G., 1999. Applicability of the standard k–ε turbulence model to the dynamic simulation of bubble columns: Part I. Detailed numerical simulations. Chemical Engineering Science 54 (13–14), 2273–2284.
Sutherland, K. L., 1948. Physical chemistry of flotation. XI. Kinetics of the flotation process. The Journal of Physical Chemistry 52 (2), 394–425.
Tabib, M. V., Roy, S. A., Joshi, J. B., 2008. CFD simulation of bubble column—an analysis of interphase forces and turbulence models. Chemical Engineering Journal 139 (3), 589–614.
Tsuchiya, K., Furumoto, A., Fan, L.-S., Zhang, J., 1997. Suspension viscosity and bubble rise velocity in liquid-solid fluidized beds. Chemical Engineering Science 52 (18), 3053–3066.
Wang, G., Ge, L., Mitra, S., Evans, G. M., Joshi, J. B., Chen, S., 2018. A review of CFD modelling studies on the flotation process. Minerals Engineering 127, 153–177.
Wang, G., Nguyen, A. V., Mitra, S., Joshi, J. B., Jameson, G. J., Evans, G. M., 2016. A review of the mechanisms and models of bubble–particle detachment in froth flotation. Separation and Purification Technology 170, 155–172.
Wang, P., Cilliers, J. J., Neethling, S. J., Brito-Parada, P. R., 2019. The behavior of rising bubbles covered by particles. Chemical Engineering Journal 365, 111–120.
Welsby, S. D. D., Vianna, S. M. S. M., Franzidis, J.-P., 2010. Assigning physical significance to floatability components. International Journal of Mineral Processing 97 (1), 59–67.
Wills, B. A., Finch, J. A., 2016. Wills' mineral processing technology: An introduction to the practical aspects of ore treatment and mineral recovery, 8th Edition. Butterworth-Heinemann, Oxford.
Wilson, C., 2009. Modelling multiple-material flows on adaptive unstructured meshes. Ph.D. thesis, Imperial College London.
Yoon, R. H., Luttrell, G. H., 1989. The effect of bubble size on fine particle flotation. Mineral Procesing and Extractive Metallurgy Review 5, 101–122.
Zaruba, A., Krepper, E., Prasser, H.-M., Vanga, B. R., 2005. Experimental study on bubble motion in a rectangular bubble column using high-speed video observations. Flow Measurement and instrumentation 16 (5), 277–287.

- An efficient numerical framework for the modelling of the polydisperse pulp phase in flotation has been presented.
- The framework—Fluidity, an open-source finite-element (FE) framework, uses mesh adaptivity and parallelisation; first FE framework for modelling the pulp phase.
- Bubble polydispersity modelled using population balance equation (PBE), which has been solved using the direct quadrature method of moments (DQMOM).
- Solid polydispersity modelled for the first time in flotation using transport equations for three size classes.
- The presented framework can be used for the simulation of a variety of polydisperse multiphase flow problems in the process industry.

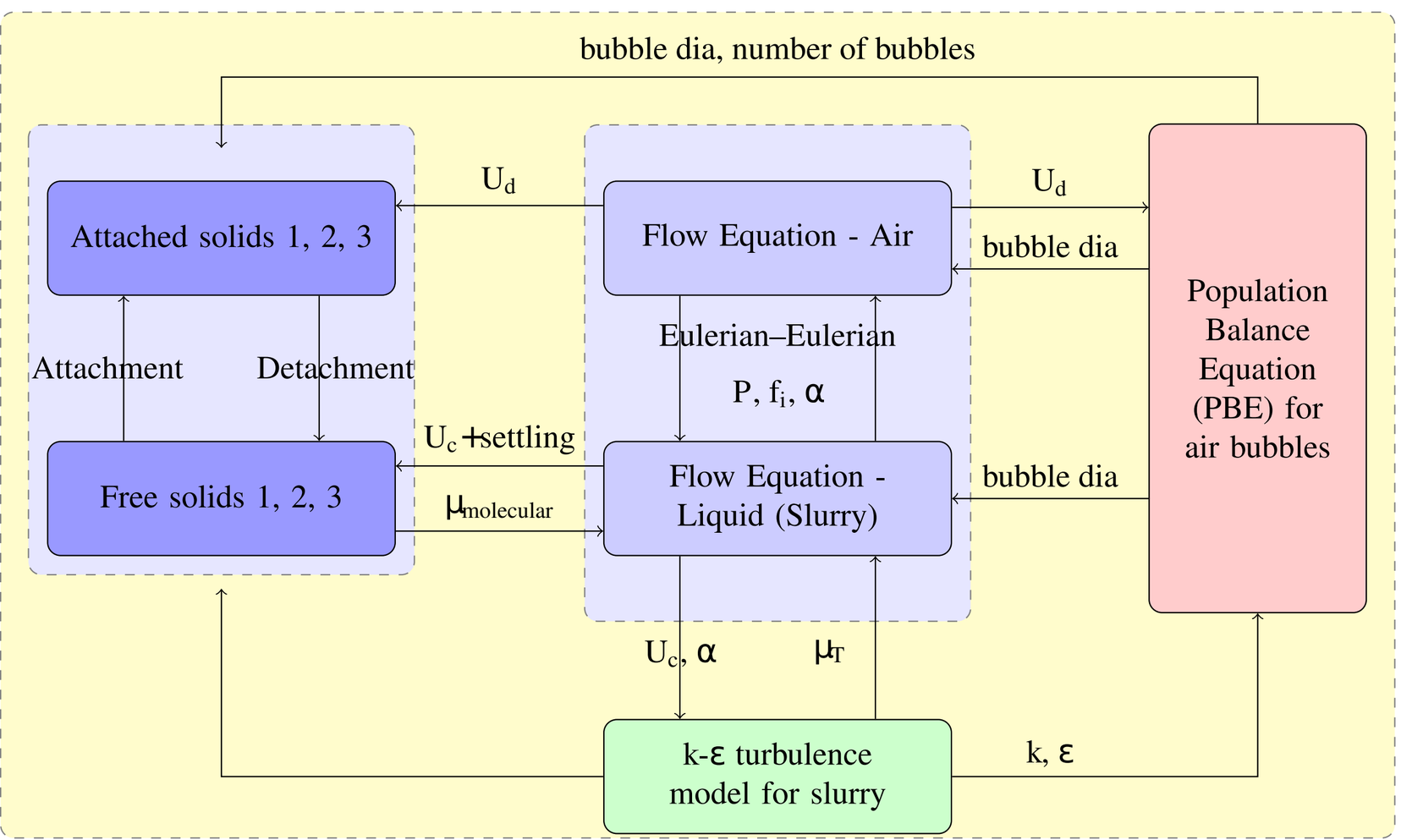
bubble dia, number of bubbles
Attached solids 1, 2, 3
Free solids 1, 2, 3
Attachment
Detachment
U_d
U_c +settling
$\mu_{molecular}$
Flow Equation - Air
Eulerian–Eulerian
P, f_i, α
Flow Equation - Liquid (Slurry)
U_c, α
μ_T
U_d
bubble dia
bubble dia
Population Balance Equation (PBE) for air bubbles
k-ε turbulence model for slurry
k, ε

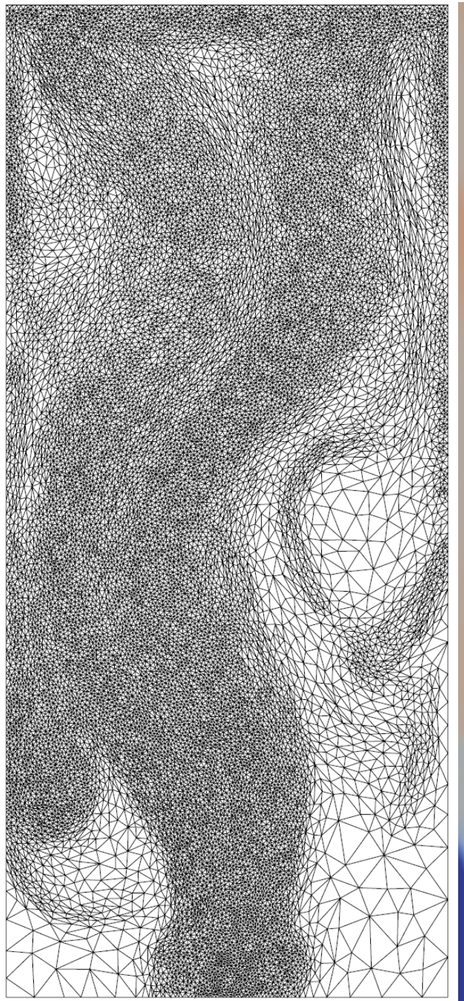

A framework for polydisperse pulp phase modelling in flotation

Gaurav Bhutani[a,b,c,*], Pablo R. Brito-Parada[b,c]

[a]*Multiphase Flow Research Lab, School of Engineering, Indian Institute of Technology Mandi, Kamand 175005, India*
[b]*Advanced Mineral Processing Research Group, Department of Earth Science and Engineering, Imperial College London, South Kensington Campus, London SW7 2AZ, United Kingdom*
[c]*Applied Modelling and Computation Group, Department of Earth Science and Engineering, Imperial College London, South Kensington Campus, London SW7 2AZ, United Kingdom*

Abstract

Froth flotation is one of the most widely-used mineral processing operations. The pulp zone in flotation tanks is polydisperse in general and serves as a medium for the interaction between the solid particles and the gas bubbles in a liquid continuum, leading to particle–bubble attachment/detachment and bubble coalescence/breakage phenomena. To better predict the hydrodynamics and inform the design of efficient flotation equipment, it is therefore important to accurately model and simulate the evolution of the size distribution of the dispersed phases. This has created an urgent need for a framework that can model the pulp phase in an efficient manner, which is not currently available in the literature. The available software products are not efficient enough to allow for a tractable modelling of industrial-scale flotation cells and in some cases they cannot model the polydispersity of the dispersed phase at all. This work presents an efficient numerical framework for the macroscale simulation of the polydisperse pulp phase in froth flotation in an open-source finite element computational fluid dynamics (CFD) code that provides an efficient solution method using mesh adaptivity and code parallelisation. A (hybrid finite element–control volume) finite element framework for modelling the pulp phase has been presented for the first time in this work. An Eulerian–Eulerian turbulent flow model was implemented in this work including a transport equation for attached and free solid particles. Special care was taken to model the settling velocity of the free solids and the modification of the liquid viscosity due to the presence of these particles. Bubble polydispersity was modelled using the population balance equation (PBE), which was solved using the direct quadrature method of moments (DQMOM). Appropriate functions for bubble coalescence and breakage were chosen in the PBE. Mesh adaptivity was applied to the current problem to produce fully-unstructured anisotropic meshes, which improved the solution efficiency, while all simulations were executed on a multicore architecture. The model was validated for 2D simulations of a bubble column against experimental results available in the literature. After successful validation, the model was applied to the simulation of the pulp phase in a flotation column for monodisperse and polydisperse solids. Polydispersity of the solids was modelled for the first time in this work using three separate solid size classes. A clear dependence of the flotation rate on the particle size was noticed and the monodisperse solids simulations were shown to over-predict the flotation rate. Other than flotation, this open-source framework can be used for the simulation of a variety of polydisperse multiphase flow problems in the process industry.

Keywords: CFD, mesh adaptivity, polydisperse flow, population balance modelling, pulp phase

1. Introduction

Froth flotation is one of the most widely used mineral processing operations, used to selectively separate the valuable mineral particles from the unwanted waste particles. Other than mineral processing, flotation is also used for deinking in wastepaper recycling, wastewater treatment, and oil separation applications. Air is injected into a tank containing a slurry of crushed ore; and mixing generated in the pulp zone causes the hydrophobic mineral particles to collide and attach to the air bubbles that rise to the top into the froth zone, which overflows as concentrate. The pulp zone in flotation is a multi-scale, turbulent, three-phase, and polydisperse system that serves as a medium for the interaction between the solid particles and the gas bubbles in a liquid continuum. It is therefore important to accurately model the physics (particularly the hydrodynamics) in the pulp zone for the development of efficient flotation equipment.

Computational fluid dynamics (CFD) has emerged as a popular technique for the numerical modelling and simulation of multiphase flow systems. This can be attributed to continuous improvements in computational power and development of improved numerical algorithms for the modelling of multiphase flows. CFD therefore offers a promising possibility for the modelling of the complex physics occurring in the pulp zone in froth flotation. The pulp physics, however, are considerably challenging compared to the typical multiphase flow systems discussed in the literature, and the available CFD software products either cannot handle all the above complexi-

*Corresponding author
Email addresses: gaurav@iitmandi.ac.in (Gaurav Bhutani), p.brito-parada@imperial.ac.uk (Pablo R. Brito-Parada)

ties or are not tractable enough to allow for the modelling of industrial-scale flotation devices. An efficient CFD framework that can model the hydrodynamics in the pulp phase is therefore needed.

Gaudin (1932) and Garcia-Zuñiga (1935) were the first to study the effect of flow properties on flotation recovery, realising the importance of the hydrodynamics in the pulp zone on flotation. The flotation recovery was found to be sensitive to flow parameters and the need to understand the physics of the processes occurring in the pulp zone was identified. There have been studies that model the hydrodynamics of the pulp phase in froth flotation (Bloom and Heindel, 2002, 2003), however Koh et al. (2000) were the first to simulate the pulp phase in a flotation tank using CFD modelling. Consistently improving their pulp phase models over time (Koh and Schwarz, 2003, 2006, 2007), the above researchers were able to model the fluids (liquid and gas) using two-phase unsteady flow equations and the solids using separate transport equations for free and attached particles. Please note that 'particles' in this paper refers to the solid particles, unless clarified otherwise. The Eulerian–Eulerian (E–E) method coupled to the k-ε turbulence model was used for modelling the fluid phases, and the equations were solved using the CFX-4 code for a fixed bubble size. Karimi et al. (2014a) and Karimi et al. (2014b) solved a similar pulp phase model in ANSYS Fluent.

The importance of including a good estimate for the bubble size distribution (BSD) in the models for pulp hydrodynamcs has been known (Gorain et al., 1995; Grevskott et al., 1996), and Evans et al. (2008) and Koh and Schwarz (2008b) were the first to include the population balance equation (PBE), which models the effects of bubble coalescence and breakage, for modelling the BSD in a flotation pulp. The method of classes (CM) implementation of ANSYS was used to solve the PBE in the CFX software in both studies, and the latter reported a significant effect of modelling the BSD on the flotation rate prediction. Others have also used the CM to model the BSD in flotation systems (Basavarajappa et al., 2017; Sarhan et al., 2017, 2018). Recently, Schwarz et al. (2016) have summarised the importance of the need of more efficient methods—the quadrature-based moment methods (QBMMs)—for solving the PBE in the flotation pulp, since these methods are computationally economical than their counterparts. The use of quadrature method of moments (QMOM), a type of QBMM, to solve the PBE for modelling the BSD in a flotation cell geometry has been reported in the literature recently (Basavarajappa and Miskovic, 2015), however this work considered gas-liquid flows only (without solids).

QBMMs, such as QMOM and direct quadrature method of moments (DQMOM), have proven to be very efficient when coupled to the E–E fluid flow equations for modelling industrial-scale polydisperse multiphase systems (Marchisio et al., 2003b). Although there are a few studies available that model the pulp phase containing a model for the BSD evolution as discussed above, there is a need for a framework that allows for the modelling of the BSD using a QBMM in the pulp phase. Sarhan et al. (2016, 2017, 2018) have recently proposed a CM-based pulp phase modelling framework that models all three phases as Eulerian phases and handles one class of solid particles. Additionally, the solids feed entering the flotation tank is in the form of a particle size distribution and the framework should also be able to consider this polydispersity of the solids for an accurate modelling of the overall process. Current literature is confined to models that deal with monodisperse solids in the pulp and there remains a need for a framework that can model the polydispersity of the solids in the feed, along with the polydispersity of the gas phase. The overall multiphase turbulent CFD model becomes highly complex when the polydispersity of the dispersed phases is considered. The available software products are not efficient enough to allow for a tractable modelling of industrial scale flotation devices, if at all they can model the polydispersity of the dispersed phases.

To address the above limitations, this work presents an efficient numerical framework for the macroscale simulation of the three-phase polydisperse pulp. This framework, known as Fluidity, is an open-source finite element code that provides an efficient solution method through its fully-unstructured mesh adaptivity feature that can produce highly-anisotropic meshes. Moreover, Fluidity is highly-parallelised, which, along with its other features, makes the solution method highly tractable.

This paper is organised as follows: Section 2 discusses the modelling framework that was developed in this work, including details of the multiphase model equations for the three phases in flotation. Brief details of finite element discretisations and adaptive mesh refinement are also presented in this section. Section 3 describes the flotation problem (geometry and operating conditions) that was solved using the present framework. Section 4 presents model validation for a two-phase bubble column, followed by results for a pulp phase simulation in a flotation column-like geometry. Finally the conclusions and the scope for future work are presented in Section 5.

2. Modelling framework

A set of coupled partial differential equations (PDEs) was used to model the polydisperse pulp phase in this study, and these equations were solved using the adaptive-mesh finite element framework—Fluidity. Fluidity permitted the modelling of the polydisperse phases in an efficient way, which is currently missing in the literature.

Figure 1 shows the complete set of equations and the coupling between them that was used to model the pulp phase inside a flotation column. Separate momentum equations were solved for the air and the liquid (or slurry) phases, assuming the flow to be incompressible (due to low Mach flow). The momentum equations for these two Eulerian phases were coupled to each other through a common pressure field, phase volume fractions and the interphase interaction force, as shown in the figure. In addition, a population balance equation for the air bubbles was

solved to predict the change in the bubble size distribution due to coalescence and breakage processes. The bubble diameter field estimated using the PBE was used for the improved prediction of the interphase interaction force, which depends on the bubble size and can sometimes have a significant effect on the hydrodynamics.

A two-equation k-ε Reynolds-averaged Navier–Stokes (RANS) turbulence model was solved for the turbulent liquid phase. The turbulence kinetic energy (per unit mass), k, and the turbulence dissipation rate (per unit mass), ε, calculated in this turbulence model were used as inputs in the other models such as: the time-averaged liquid phase momentum equation for the calculation of the eddy viscosity, the breakage and coalescence functions in the PBE for air bubbles, and the attachment and detachment terms in the model for solids.

The solid scalar transport equations, coupled to each other through the attachment and detachment source terms, are shown on the left in Figure 1. Although more than one solid class was used in this work, only one has been shown in the figure for illustration. The free (or unattached) solids equations are coupled to the liquid phase momentum equation through the mean (or time-averaged) liquid velocity $\mathbf{U}_c$ and the modified liquid viscosity $\mu_{\text{molecular}}$. The attached solids transport equations are coupled to the gas phase momentum equation through the gas phase velocity field. The PBE supplies the bubble diameter and the bubble concentration for the attachment and detachment rate expressions.

In the present model the bubble size distribution is not affected by attached solids. The breakage and coalescence rate expressions for the bubble population balance equation should ideally include the physics of particle attachment affecting stability of bubbles. The present breakage and coalescence terms only include the liquid phase turbulence, which is affected by the free solids concentration only. Similarly, the gas holdup, which gets modified with the change in bubble size distribution, also doesn't get affected by attached solids in this work. There is no work in the literature that presents an empirical relation for the effect of particle attachment on bubble stability. The effects of adding reagents (collectors, frothers, activators and depressants) in the pulp phase have not been modelled in the present work.

This framework is unique allowing a strong coupling between the different phases (as shown in Figure 1). The highly-parallelised nature of Fluidity along with the ability to handle fully-unstructured adaptive meshes makes it specially suitable to simulate industrial scale flotation pulp. At the present stage there is no other commercial or freely available software product that allows this kind of modelling capability. A detailed description of the modelling equations is presented in the subsections that follow.

2.1. Flow equations

An incompressible E–E model was chosen in this work over the other options available—mixture model and Eulerian–Lagrangian model—as it provides a good balance between accuracy and complexity.

As described in Ishii and Hibiki (2010), the RANS equation for the two phases in this work can be written as:

$$\alpha_i\rho_i\frac{\partial \mathbf{U}_i}{\partial t}+\alpha_i\rho_i\mathbf{U}_i\cdot\nabla\mathbf{U}_i = -\alpha_i\nabla P+\alpha_i\rho_i\mathbf{g}+\nabla\cdot[\alpha_i(\bar{\bar{\tau}}_i+\bar{\bar{\tau}}_i^R)]+\mathbf{f}_i, \quad (1)$$

where the subscript i can be c or d, denoting the continuous (liquid) and the dispersed (gas) phases, respectively. In the above equation, α is the phase volume fraction, ρ is the phase density, $\mathbf{U}$ is the mean phase velocity, P is the mean static pressure, $\mathbf{g}$ is the acceleration due to gravity, $\bar{\bar{\tau}}$ is the mean shear stress tensor, $\bar{\bar{\tau}}^R$ represents the Reynolds stress tensor, and $\mathbf{f}_i$ is the sum of all interphase forces acting on the ith phase due to the other phase.

Ishii and Hibiki (2010) derived the above equation using Reynolds time averaging performed at a point location in space, unlike the usual spatial averaging approach. Their approach defines a phase density function M_i which is equal to one for the phase i and zero otherwise; the volume fraction therefore results from the Reynolds time averaging of M_i at a point location. Weight average of a function F, $\langle wF\rangle/\langle w\rangle$, leads to the definition of *phase average* (weight $w = M_i$) and *mass weighted average* ($w = \rho$). In Equation (1), the mean velocity is a mass-weighted average, and mean pressure and shear stress are phase-averaged quantities. This kind of averaging prevents any statistics of the volume fraction from appearing in the mean equations. The fluctuations in the physical quantities were defined with respect to the above definitions of the mean values. In the present work turbulence was only modelled for the continuous phase and the dispersed phase was considered laminar (same as Pfleger and Becker (2001) and Bhole et al. (2008)), due to the gas phase eddy viscosity 2–3 orders smaller than the liquid phase; i.e. $\mathbf{U}_d = \mathbf{u}_d$ and $\bar{\bar{\tau}}_d^R = 0$ in Equation (1), where $\mathbf{u}$ denotes the actual velocity field.

The mean shear stress term in Equation (1) was modelled as $\bar{\bar{\tau}}_i = \mu_d\left(\nabla\mathbf{U}_i + \nabla(\mathbf{U}_i)^T\right) + \mathbb{D}_{\text{interf}}$, which is obtained from the constitutive equation for an isotropic linear viscous fluid with dynamic viscosity μ_d. $\mathbb{D}_{\text{interf}}$ is the interfacial extra deformation tensor ($\sim \nabla\alpha_c$), also known as the bubble-induced turbulence (BIT) term (Ishii and Hibiki, 2010), which contains the contribution of the bubble wake to the turbulence in the liquid phase. There are two major ways to include the contribution of the bubble wake on liquid velocity fluctuations (and hence the liquid viscous shear stress)—through the inclusion of a modified liquid viscosity (Sato and Sekoguchi, 1975) and through the modification of production terms in turbulence kinetic energy and turbulence dissipation rate equations (Pfleger and Becker, 2001; Bannari et al., 2008). The literature contains works comparing the two approaches and there is no consensus on the superiority of one model over the other. While a few prefer the use of modified viscosity (Pfleger et al., 1999; Ojima et al., 2014), many found the use of modified production better (Olmos et al., 2003), and a few simply found the inclusion of BIT

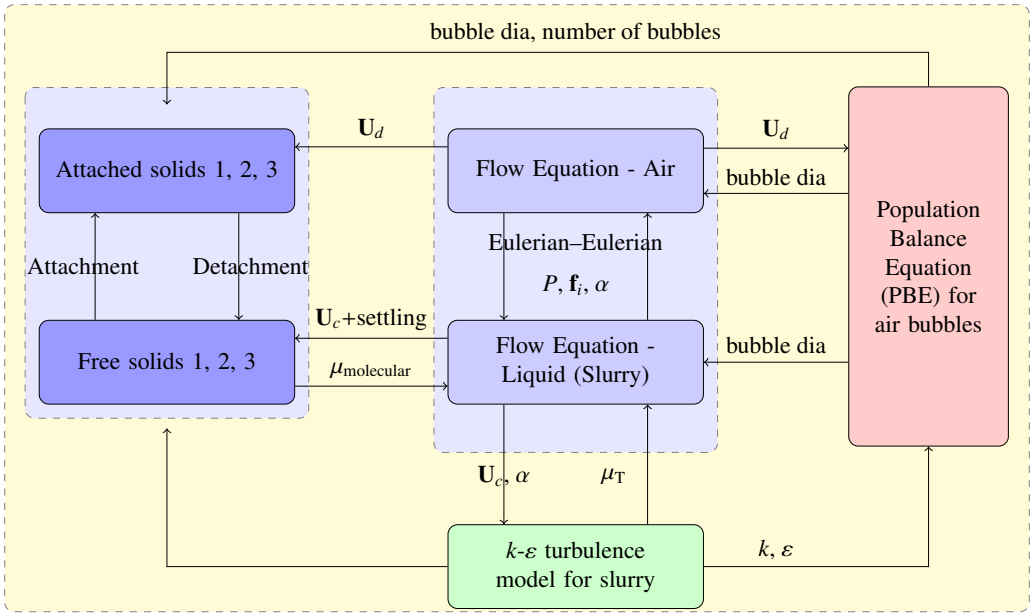

Figure 1: Coupling of the model equations used for modelling the three-phase pulp phase in a flotation column.

model detrimental to validation (Pfleger and Becker, 2001). A study by Zaruba et al. (2005) experimentally showed the contribution of BIT an order or magnitude smaller than the shear-induced turbulence in a thin rectangular bubble column, similar to the geometry employed in the present work. The BIT model was excluded from the present model due to its mixed acceptance in the literature.

A common pressure field was considered for the two Eulerian phases (Bhutani et al., 2016), which required that only one (common) continuity equation had to be solved. The common continuity equation is given as (Ishii and Hibiki, 2010):

$$\nabla \cdot (\alpha_d \mathbf{U}_d) + \nabla \cdot (\alpha_c \mathbf{U}_c) = 0, \tag{2}$$

In polydisperse flow modelling, the interphase interaction force $\mathbf{f}_i$, which includes the drag and non-drag forces, is responsible for coupling the dispersed phase particle size to the model momentum equations. The drag force, which is the most significant of all interphase forces, consists of both the pressure and the viscous drag on the body, and can be written as:

$$\mathbf{f}_i = \pm \frac{3\alpha_c \alpha_d C_D \rho_c (\mathbf{U}_c - \mathbf{U}_d)|\mathbf{U}_c - \mathbf{U}_d|}{4d}, \tag{3}$$

where C_D is the drag coefficient and d is the dispersed phase diameter. In the present work the Schiller–Naumann drag force correlation was used to obtain the drag coefficient (Schiller and Naumann, 1935). This coefficient models the drag well for viscous and Newton's flow regimes (Ishii and Hibiki, 2010), which were prominent in the present situation. Many others have also used the Schiller–Naumann correlation to model drag in bubbly flows (Buwa and Ranade, 2002; Chen et al., 2005). It is given as:

$$C_D = \begin{cases} \dfrac{24}{Re_d}\left(1 + 0.15 {Re_d}^{0.687}\right) & \text{if } Re_d < 1000, \\ 0.44 & \text{otherwise,} \end{cases} \tag{4}$$

where Re_d, the dispersed phase Reynolds number, is defined as:

$$Re_d = \frac{\rho_c d|\mathbf{U}_c - \mathbf{U}_d|}{\mu_c}. \tag{5}$$

Equation (4) clearly shows the two flow regimes—the viscous flow regime with a strong dependence of the drag coefficient on Re_d and the Newton's regime with C_D independent of Re_d. The non-drag force includes the lift and virtual mass forces, plus other forces such as the Basset force, the Brownian force and the thermophoretic force. These forces, however, were neglected in the present model as their effect on the flow is negligible (Chen et al., 2004; Tabib et al., 2008; Díaz et al., 2008a). Reynolds-averaging of the discontinuities in the phases, which results in the interphase interaction force term discussed above, also gives rise to additional terms such as the interfacial pressure term and the interfacial shear stress terms ($\sim \nabla\alpha_i$), both of which were neglected in the present formulation (Bhutani, 2016). The turbulent dispersion force term, which originates from the continuous phase velocity fluctuations and affects bubble motion was neglected in the present model due to its disputed nature (Ishii and Hibiki, 2010).

The dispersed phase volume fraction, α_d, was obtained from the solution to:

$$\frac{\partial \alpha_d}{\partial t} + \nabla \cdot (\alpha_d \mathbf{U}_d) = 0 \tag{6}$$

and the conservation equation

$$\alpha_d + \alpha_c = 1 \tag{7}$$

was used to obtain continuous phase volume fraction α_c.

The Reynolds stress, $\bar{\bar{\tau}}_c^R$, is a result of the Reynolds-averaging of the non-linear convective term in the momentum equation and is responsible for applying the effect of turbulent fluctuations on the mean flow. Since turbulence was only modelled for the continuous phase, the subscript c has been omitted in the subsequent discussion on turbulence modelling. The turbulent viscosity hypothesis introduced by Boussinesq was used to close the Reynolds stress term, given as:

$$\bar{\bar{\tau}}^R = -\rho\langle \mathbf{u}'\mathbf{u}'\rangle = \mu_T\left(\nabla\mathbf{U} + (\nabla\mathbf{U})^T\right) - \frac{2}{3}k\rho\bar{\bar{I}}. \tag{8}$$

In the above equation, $\mathbf{u}'$ is the fluctuating component of the liquid velocity and μ_T is the (isotropic) eddy viscosity. The eddy viscosity in the k-ε model, which is the simplest complete model for turbulence, is defined as:

$$\mu_T = \rho C_\mu \frac{k^2}{\varepsilon}, \tag{9}$$

where C_μ is a model constant. The turbulent kinetic energy, $k = \frac{1}{2}\langle \mathbf{u}' \cdot \mathbf{u}'\rangle$, is the mean kinetic energy per unit mass in the fluctuating velocity, and the turbulent dissipation rate, $\varepsilon = \frac{2\mu}{\rho}\langle \bar{\bar{s}} \cdot \bar{\bar{s}}\rangle$ ($\bar{\bar{s}}$ being the fluctuating rate of deformation tensor), quantifies the dissipation of turbulent kinetic energy at small scales. Standard form of the transport equations for k and ε (Jones and Launder, 1973) were solved; the equations are given as:

$$\alpha\rho\frac{\partial k}{\partial t} + \alpha\rho\mathbf{U}\cdot\nabla k = \nabla\cdot\left(\alpha\left(\mu + \frac{\mu_T}{\sigma_k}\right)\nabla k\right) + \alpha\bar{\bar{\tau}}_R : \nabla\mathbf{U} - \alpha\rho\varepsilon \tag{10}$$

and

$$\alpha\rho\frac{\partial \varepsilon}{\partial t} + \alpha\rho\mathbf{U}\cdot\nabla\varepsilon = \nabla\cdot\left(\left(\alpha\mu + \frac{\mu_T}{\sigma_\varepsilon}\right)\nabla\varepsilon\right) + C_{\varepsilon 1}\left(\frac{\varepsilon_i}{k}\right)\left(\alpha\bar{\bar{\tau}}_R : \nabla\mathbf{U}\right) - C_{\varepsilon 2}\alpha\rho\frac{\varepsilon^2}{k}. \tag{11}$$

The RHS terms in both equations consist of the diffusion, the production from mean shear, and the destruction term. Interphase interaction terms appearing in the k and ε equations were neglected here, as did Ranade (1997) and Buwa and Ranade (2002). Model constants suggested by Launder and Sharma (1974) were used in this study (Table 1). σ is the turbulence Schmidt number here.

Table 1
Model constants in the standard k-ε model given by Launder and Sharma (1974).

C_μ	0.09
$C_{\varepsilon 1}$	1.44
$C_{\varepsilon 2}$	1.92
σ_k	1.0
σ_ε	1.3

Koh and Schwarz (2007) incorporated the effect of attached particles on the gas bubble weight through a body force term in the gas momentum equation. Further, they also presented the effect of modifying the buoyancy term on the prediction of flotation rate. The present model does not include the buoyancy modification term.

2.2. Population balance equation

The population balance equation is a mesoscale integro-differential equation that can be used to model the evolution of the size distribution of polydisperse particles (Ramkrishna, 2000; Marchisio and Fox, 2013). In this study, the PBE was used to model the evolution of the size distribution of the bubbles only. The polydispersity of the solids was modelled using three separate classes, which will be discussed later in Section 3. The moving bubbles in a flotation system coalesce and break, which results in the spatial and temporal evolution of their distribution.

The PBE can be written as:

$$\frac{\partial n(\xi, \mathbf{x}, t)}{\partial t} + \nabla\cdot\left(\langle \mathbf{u}|\xi\rangle\, n\right) = S_\xi(\xi, \mathbf{x}, t), \tag{12}$$

where $n(\xi, \mathbf{x}, t)$ is the dispersed phase number density function (NDF), ξ is the internal coordinate (representing the dispersed phase size), and $\mathbf{x}$ is the external (or spatial) coordinate. $\langle \mathbf{u}|\xi\rangle$ is the mean dispersed phase velocity conditional to the bubble size and is responsible for convecting the bubbles in the physical space. However this dependence on the dispersed phase size was not considered in the present study and the air velocity field computed using Equation (1) was used in the PBE. Only one internal variable—the bubble size—was of interest in this work, however multivariate PBE containing more than one internal variable has also been discussed in the literature (Buffo and Alopaeus, 2016).

S_ξ, the source term in Equation (12), includes all terms containing derivatives or integrals with respect to the dispersed phase size ξ. It can be used to model dispersed phase growth, diffusion in the internal space, and the birth and death functions due to dispersed phase breakage and coalescence. Growth and internal diffusion terms did not arise in the present model and were not included in Equation (12).

As discussed previously, the PBE in this work was used to estimate the bubble size in the flotation system to accurately model the drag force term in momentum equations (Equations (1) and (1)). The PBE was also used to calculate the bubble concentration, which was needed in the bubble–particle attachment and detachment models.

Breakage and coalescence are discontinuous events that lead to the birth and death of bubbles in a very short time. The contribution to the source term S_ξ from birth and death functions due to bubble breakage and coalescence is given as:

$$S_\xi = B_B + B_C - D_B - D_C. \tag{13}$$

The birth and death functions due to breakage are given as:

$$B_B(\xi) = \int_{\xi}^{\infty} \nu(\xi_1) a(\xi_1) b(\xi|\xi_1) n(\xi_1)\, \mathrm{d}\xi_1 \tag{14}$$

and

$$D_B(\xi) = a(\xi) n(\xi), \tag{15}$$

respectively. Here, $\nu(\xi)$, $a(\xi)$ and $b(\xi|\xi_1)$ are the breakage kernels that define the number of bubbles formed after breakage, the breakage frequency, and the daughter distribution function, respectively. Note that the spatial and temporal dependence of the NDF has been suppressed here for compactness.

Coalescence is described in terms of a coalescence frequency $\beta(\xi', \xi)$ for bubbles of sizes ξ' and ξ. If there is no statistical correlation between the colliding bubbles, the bubble pairs can be defined as the product of two individual number densities, and the birth and death functions due to coalescence are given as:

$$B_C = \frac{1}{\tilde{\delta}} \int_0^{\xi} \left(\frac{\xi^2}{\xi'^2} \right) \beta(\xi', \xi_1) n(\xi') n(\xi_1)\, \mathrm{d}\xi_1 \tag{16}$$

and

$$D_C = \int_0^{\infty} \beta(\xi, \xi_1) n(\xi) n(\xi_1)\, \mathrm{d}\xi_1, \tag{17}$$

respectively. $\tilde{\delta}$ in the above equation represents the number of bubbles coalescing to form a larger bubble. In Equation (16), ξ' is given as $\xi'^3 = \xi^3 - \xi_1^3$, i.e. the volume of the resulting bubble class (ξ) is the sum of the volumes from the contributing size classes (ξ' and ξ_1).

The internal coordinate presents the major challenge in the numerical solution of the PBE. Most methods eliminate the internal coordinate from the PBE to bring it in a form that can be solved numerically using established methods. The popular numerical solution methods for the PBE can be grouped into two general categories—the method of classes and the method of moments. The CM discretises the internal coordinate in the NDF, giving rise to various classes (Marchal et al., 1988). The PBE transforms to a set of advection–diffusion equations for the discretised NDF corresponding to each class. A large number of classes are needed for a reasonable accuracy when the PBE is coupled to the multiphase flow equations, which makes the solution of a normal engineering system extremely expensive. For instance, Sarhan et al. (2017) used 10 classes for the bubble NDF in their flotation column model, which equates to solving 10 extra advection–diffusion equations in addition to the multiphase flow equations. The size distribution can change significantly in a very short time due to the discontinuous nature of the breakage and coalescence events, and therefore a large number of classes must be considered to factor this possibility.

The method of moments (MOMs), as the name suggests, solves for the evolution of the moments of the NDF instead; k^{th} moment of the NDF can be written as $m_k = \int_0^{\infty} \xi^k n(\xi)\, \mathrm{d}\xi$. The internal coordinate gets integrated when the moments of the NDF are evaluated in the PBE, but in the process various unclosed terms are generated. The various methods of moments available in the literature are differentiated based on the closure method used. Quadrature-based moment methods are popular as they are simple and robust, and the mathematical closure in the QBMM can be applied to any problem without an understanding of its physics. In this method, the higher-order unclosed moments are written in terms of the lower-order moments, which are transported. QMOM and DQMOM are two popular QBMMs used in the literature. QMOM approximates the integrals in terms of weights and abscissas (McGraw, 1997), whereas DQMOM uses a quadrature approximation for the NDF itself (Marchisio and Fox, 2005), given by:

$$n(\xi, \mathbf{x}, t) = \sum_{j=1}^{N} w_j(\mathbf{x}, t)\, \delta\left[\xi - \langle\xi\rangle_j(\mathbf{x}, t)\right], \tag{18}$$

where δ is the Dirac delta function, N is the total number of quadrature points, and w_j and $\langle\xi\rangle_j$ are the weights and abscissas in the DQMOM approximation, respectively. DQMOM was chosen to solve the PBE in this work because each weight and abscissa can be defined as a function of space, which makes the implementation of the method in a CFD code straightforward. Also, very few abscissas are needed to accurately model the NDF due to the adaptive quadrature approach of DQMOM.

The DQMOM approximation to the NDF when substituted into the PBE (Equation (12)) results in the following set of transport equations (Marchisio and Fox, 2005):

$$\frac{\partial w_j}{\partial t} + \nabla \cdot \left(\mathbf{u}\, w_j\right) = g_j \tag{19}$$

and

$$\frac{\partial \varsigma_j}{\partial t} + \nabla \cdot \left(\mathbf{u}\, \varsigma_j\right) = h_j, \tag{20}$$

where $j = 1, 2, ..., N$. The source terms g_j and h_j are obtained from the solution of the linear system

$$(1-k) \sum_{j=1}^{N} \langle\xi\rangle_j^k g_j + k \sum_{j=1}^{N} \langle\xi\rangle_j^{k-1} h_j = \overline{S}_k^{(N)}, \tag{21}$$

which is obtained by computing the k^{th} moment of the PBE; here $k = 1, 2, ..., 2N$. The above set of equations were solved for the weights w_j and the weighted abscissas ς_j, which were then used to calculate the moments and eventually the Sauter mean diameter ($d_{32} = m_3/m_2$). The bubble surface area flux is an important parameter that is used to characterise flotation and since the Sauter mean diameter (SMD) includes the effect of the total surface area of the bubbles (through m_2) it was used as an estimate for the bubble diameter in this study. $\overline{S}_k^{(N)}$ is the k^{th} moment of the source term in the PBE and the DQMOM approximation to the NDF provides a convenient closure for this source term. It is given as:

$$\begin{aligned} \overline{S}_k^{(N)} = &\sum_{j=1}^{N} \overline{b}_j^{(k)} a_j w_j - \sum_{j=1}^{N} \langle\xi\rangle_j^k a_j w_j \\ &+ \frac{1}{2} \sum_{j=1}^{N} \sum_{i=1}^{N} \left(\langle\xi\rangle_j^3 + \langle\xi\rangle_i^3 \right)^{k/3} \beta_{ji} w_j w_i - \sum_{j=1}^{N} \sum_{i=1}^{N} \langle\xi\rangle_j^k \beta_{ji} w_j w_i, \end{aligned} \tag{22}$$

where the term $\overline{b}_j^{(k)}$ is given as:

$$\overline{b}_j^{(k)} = \int_0^\infty \xi^k b(\xi|\langle\xi\rangle_j)d\xi. \quad (23)$$

In the above equation, $b(\xi|\langle\xi\rangle_j) = 0$ for $\xi > \langle\xi\rangle_j$, which restricts the daughter bubble size to be smaller than the parent. The breakage kernel $\nu(\xi)$ is usually absorbed in the daughter distribution function $b(\xi|\xi_1)$ (Marchisio et al., 2003b,a) and has been omitted from Equation (22).

Compared to the CM, DQMOM requires a fewer number of equations that need to be solved to get a good estimate of the BSD. For instance, Marchisio et al. (2003b) stated that 4–6 equations in DQMOM (i.e., N=2–3) provide similar accuracy as 50–200 classes in the CM. Two quadrature points were used in the DQMOM approximation in this study.

The problem of moment corruption (i.e., the moment-set becoming invalid or unrealisable) has been reported with the use of the MOMs in the literature (Petitti et al., 2010). However, it has been established that the first-order upwind convective scheme in the finite volume discretisation, which was used for the PBE transport equations in this work, always leads to realisable moments for $N \leq 3$ (Desjardins et al., 2008; Mazzei et al., 2012). The details of the implementation of DQMOM in Fluidity and its verification have been presented in a previous publication by the authors (Bhutani et al., 2016).

2.2.1. Kernels

The breakage and coalescence kernels are chosen based on the physics of the problem under consideration. The most widely accepted theory for bubble breakage states that the bubble breakage phenomenon is characterised by a balance between the forces in the liquid trying to deform the bubble (the turbulent fluctuations) and the restoring force due to interfacial tension (Andersson and Andersson, 2006). On the same lines, the breakage rate proposed by Laakkonen et al. (2006) was used for modelling bubble breakage in this work. It is given as:

$$a(\xi) = C_1\varepsilon^{1/3}\mathrm{erfc}\left(\sqrt{C_2\frac{\sigma}{\rho_c\varepsilon^{2/3}\xi^{5/3}} + C_3\frac{\mu_c}{\sqrt{\rho_c\rho_d}\varepsilon^{1/3}\xi^{4/3}}}\right), \quad (24)$$

where σ is the gas–liquid interfacial tension, and C_1, C_2 and C_3 are empirical model constants with C_1 having dimensions of $\mathrm{L}^{-2/3}$. The stabilising effect of viscous stresses was also considered along with the interfacial tension effects in the above breakage rate kernel. Other popular choices for the breakage kernels are the ones proposed by Coulaloglou and Tavlarides (1977), Luo and Svendsen (1996) and Prince and Blanch (1990).

Binary breakage was assumed in this work ($\nu(\xi) = 2$), and the daughter distribution function proposed by Laakkonen et al. (2007) was employed in this study. It is given as:

$$b(\xi_1|\xi_2) = \frac{1}{2}(C_4{+}1)(C_4{+}2)(C_4{+}3)(C_4{+}4)\left(\frac{{\xi_1}^2}{{\xi_2}^3}\right)\left(\frac{{\xi_1}^3}{{\xi_2}^3}\right)^2\left(1-\frac{{\xi_1}^3}{{\xi_2}^3}\right)^{C_4}. \quad (25)$$

The above expression does not take the effect of turbulence or any other parameter, other than the bubble size, into account. It is mathematically well-posed and numerically more stable than the other expressions (Luo and Svendsen, 1996). C_4 is a constant that can be calculated using the normalisation property of daughter distribution function.

Bubble coalescence is considered more complex than breakage because it not only involves the interaction between bubbles and liquid, as in breakage, but also between different bubbles. The coalescence rate kernel is written as a product of the collision frequency and the coalescence efficiency. It is the turbulence in the continuous phase that is responsible for the collision between the bubbles in the pulp zone. The coalescence efficiency is modelled by comparing the film drainage time with the bubble interaction time. Assuming the coalescing bubble interfaces to be immobile, Laakkonen et al. (2006) obtained the following expression for the coalescence efficiency:

$$\eta(\xi_1,\xi_2) = \exp\left[-C_6\frac{\mu_c\rho_c\varepsilon}{\sigma^2}\left(\frac{\xi_1\xi_2}{\xi_1+\xi_2}\right)^4\right]. \quad (26)$$

The coalescence rate was therefore given as:

$$\beta(\xi_1,\xi_2) = C_5\varepsilon^{1/3}\left(\xi_1+\xi_2\right)^2\left({\xi_1}^{2/3}+{\xi_2}^{2/3}\right)^{1/2}\eta(\xi_1,\xi_2), \quad (27)$$

and the same was used in the present study. Binary collision was assumed here ($\tilde{\delta} = 2$). For more details on the theory of bubble breakage and coalescence and the choice of kernels, see Bhutani (2016).

Evans et al. (2008) proposed their own kernels for breakage and coalescence, whereas Koh and Schwarz (2008b) used the breakage and coalescence kernels of Luo and Svendsen (1996) and Prince and Blanch (1990), respectively, to model flotation. Buffo et al. (2013) reported promising results for modelling bubble columns through the use of the breakage and coalescence kernels of Laakkonen et al. (2006); the same kernels were used in this work. Although the coalescence and breakage kernels of Laakkonen et al. (2006, 2007) used in this work have been derived for pure liquid and bubble systems, Koh and Schwarz (2008b) used similar liquid–gas expressions in their flotation simulations reporting a reasonable match with the experiments. However, it will be ideal to include kernels that can account for the the effect of solids and surfactants, which, to the best knowledge of the authors, do not exist in the literature currently.

2.3. Solids

2.3.1. Transport equations for solids

Transport equations for the free and attached solids in the pulp were solved. The total solid concentration inside the column, n_{tot}, can be given as:

$$n_{\mathrm{tot}}(\mathbf{x},t) = n_f(\mathbf{x},t) + n_a(\mathbf{x},t), \quad (28)$$

where n_f and n_a are the concentrations of the free and attached particles, respectively, in number per unit volume ($\#/m^3$).

Transport equations that were solved for $n_f(\mathbf{x}, t)$ and $n_a(\mathbf{x}, t)$ can be written as:

$$\frac{\partial n_f}{\partial t} + (\mathbf{U}_c + \mathbf{u}_{\text{settling}}) \cdot \nabla n_f = -\psi_a + \psi_d, \tag{29a}$$

$$\frac{\partial n_a}{\partial t} + \mathbf{U}_d \cdot \nabla n_a = \psi_a - \psi_d. \tag{29b}$$

Here, ψ_a is the rate of particle–bubble attachment and ψ_d is the rate of detachment. A settling velocity $\mathbf{u}_{\text{settling}}$ was added to the continuous phase velocity to get the advection velocity of the free particles, as seen in Equation (29a). The attached particles advect with the dispersed phase velocity $\mathbf{U}_d$

2.3.2. Attachment rate

The particle attachment rate was modelled as a product of the number of collisions between free particles and available bubbles and the probability of successful attachment. Is is given as:

$$\psi_a = Z_1 n_f n_b^A P_c P_a P_s, \tag{30}$$

where Z_1 is the collision rate factor (m^3s^{-1}), n_b^A is the concentration of bubbles available for attachment, and P_c, P_a and P_s are the probabilities of collision, adhesion and stabilisation, respectively.

Collision rate factor

Abrahamson (1975) was the first to derive the collision rate factor between particles in a highly turbulent fluid. The same expression was later used by Koh et al. (2000) and Bloom and Heindel (2002) to estimate the collision rate between particles and bubbles in flotation. Based on the previous studies the same collision rate factor was used in the present work, given as:

$$Z_1 = 5.0 \left(\frac{d_s + d_b}{2}\right)^2 (u_{t,s}^2 + u_{t,b}^2)^{1/2}, \tag{31}$$

where d_b is the bubble diameter, d_s is the particle diameter, $u_{t,s}$ is the RMS fluctuating velocity for the particles and $u_{t,b}$ is the RMS fluctuating velocity for the bubbles.

For large colliding particles and/or high intensity turbulence the particles do not follow the fluid streamlines and the particle velocities can be assumed to be distributed independently (in magnitude and direction). The particle velocity distribution in the above model is assumed to be Gaussian and the velocity fluctuations are represented in terms of the turbulent dissipation rate as (Koh and Schwarz, 2006; Bloom and Heindel, 2002):

$$u_{t,i} = \frac{0.4\varepsilon^{4/9}\rho_l^{1/3} d_i^{7/9}}{\mu_l^{1/3}} \left(\frac{\rho_i - \rho_l}{\rho_l}\right)^{2/3}, \tag{32}$$

where the subscript i refers to solid and gas (bubble) phases. Colliding species—particles and bubbles—are collectively referred to as 'particles' in this section in the interest of simplicity.

Equation (31) was also used by Koh and Schwarz (2006) in their pulp phase CFD model for uncorrelated solid particle and bubble velocities. The solid particle and bubble velocities remain uncorrelated as long as turbulence in the fluid is isotropic at the scale of colliding particles (which may be true even when the large-scale motion is statistically anisotropic) and the two colliding particles are moving in independent fluid elements. Velocities for the fluid elements close to each other in space will be correlated, but if the particle inertia is sufficiently larger than the drag on the particle due to these correlated elements the independence of particle velocities can be assumed. The above condition is quantified by comparing the particle relaxation time to the characteristic time for velocity fluctuation at a distance over which the fluid velocities are correlated. This results in a critical particle diameter expression, given as:

$$d_{\text{crit}} = \sqrt{\frac{15\mu_l u_{t,l}^2}{\rho_i \varepsilon}}. \tag{33}$$

For a typical flotation situation d_{crit} is 1 mm for air bubbles and 0.5 mm for solid particles (of density $2500\,\text{kgm}^{-3}$). However, the value may change depending the intensity of turbulence at a given location. Since the diameter of the bubbles introduced into the column was 5 mm Abrahamson's collision rate factor was applicable in such cases. Abrahamson's collision rate factor (Equation (31)) is therefore applicable when the solid particle or bubble diameter is greater than the above critical diameter (Koh and Schwarz, 2006). Here, $u_{t,l}$ is the RMS fluctuating velocity of the liquid phase which is equal to $\sqrt{2k}$. For bubbles, ρ_i in the above equation is taken as $0.5\rho_l$. Equation (31) is therefore applicable when the following conditions are satisfied: high-intensity turbulence in the flow, turbulence is isotropic on the scale of colliding particles, particles are nearly spherical, and the particle size is greater than the critical diameter for the solid particle and bubble velocities to be independent. Most of the above conditions were applicable in the present situation for particle–bubble collisions in flotation. The particles (and larger bubbles) however are not spherical and this is an assumption that is made here to ensure the applicability of Equation (31).

In case the solid particle and bubble velocities are correlated (i.e. for low intensity turbulence), the collision rate expression developed in the past by Saffman and Turner (1956) was used (same as Koh and Schwarz (2006)):

$$Z_1 = \sqrt{\frac{8\pi}{15}} \left(\frac{d_s + d_b}{2}\right)^3 \left(\frac{\varepsilon\rho_l}{\mu_l}\right)^{1/2}. \tag{34}$$

The above expression is based on the classical 'gradient collision' model of Smoluchowski (1917), which derives the collision rate of particles moving under uniform shear. This model assumes $d_s + d_b$ to be smaller than the smallest eddies and that the particles move with the fluid (i.e. they have a small inertia).

Bubbles available for attachment

Different approximations have been used to estimate the available bubble concentration in the literature. Bloom and Heindel

(1997) assumed that only one particle can attach to a bubble, whereas Bloom and Heindel (2003) assumed that only the bubbles that have no particle attached to them are available for attachment. Some replaced the number concentration of available bubbles with the total bubble concentration. In this work, the assumption of Koh and Schwarz (2006) of the bubbles being either fully loaded or completely clean was used. The bubble loading parameter β_{bub} was, therefore, defined as:

$$n_b^A = (1 - \beta_{\text{bub}}) n_b^{\text{tot}}, \tag{35}$$

where n_b^{tot} is the total bubble concentration. The bubble loading factor for a particular solid class i was calculated as:

$$\beta_{\text{bub},i} = \left(\frac{n_{a,i}}{n_b^{\text{tot}}}\right)\left(\frac{d_{s,i}}{d_b}\right)^2 0.5, \tag{36}$$

assuming 50% maximum loading. The total bubble concentration n_b^{tot} was calculated using the value of zeroth moment, m_0, of the bubble NDF. Equation (36) assumes that loaded bubbles always contain particles of the same size.

Collision probability

The probability of collision between free particles and bubbles in this work was calculated using the expression derived by Yoon and Luttrell (1989), given as:

$$P_c = \left(\frac{3}{2} + \frac{4}{15} Re_b^{0.72}\right)\left(\frac{d_s}{d_b}\right)^2. \tag{37}$$

This expression is based on an isolated bubble rising in particle suspension in a quiescent flow. The particles are assumed to follow fluid streamlines around the bubble, which is a reasonable assumption if the particle inertia is small. The particles and bubbles are assumed to be spherical. It was theorised by Sutherland (1948) that the particles lying inside the *grazing streamline* are able to collide with bubbles successfully. Using this theory, the probability of collision was defined as the fraction of particles in the bubble path that end up colliding with it, quantified as the ratio of the area inscribed by limiting radius R_0 to the area inscribed by bubble radius R_b, as shown in Figure 2. Yoon and Luttrell (1989) developed an empirical relation for R_0 as a function of the bubble Reynolds number (below 100), through measurements of fluid streamlines. This led to the expression for the collision probability as defined in Equation (37). Equation (37) was also used by Koh and Schwarz (2006) in their pulp phase models. Three other collision mechanisms, namely the gravitational, inertial and turbulent collision are possible (Wang et al., 2018); however, only the interceptional collision mechanism, as described above, was considered in this work.

Adhesion probability

The short-range surface forces start acting once the particle is close enough to the bubble after collision. Sutherland (1948) theorised that for the thermodynamically feasible cases the bubble–particle adhesion occurs when the particle "sliding time" is larger than the "induction time", which is the minimum time required for the liquid film to thin and rupture. For given

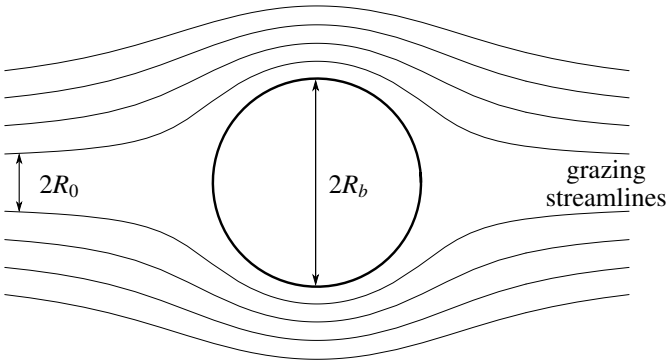

Figure 2: Fluid streamlines around a spherical bubble. Solid particles outside the *grazing streamlines* do not contact the bubble.

particle and bubble sizes, there is a maximum incidence angle that the incoming particle must hit at for the adhesion to be successful. For particles approaching at angles above this maximum angle, the sliding distance will not be long enough for the film thinning to occur in time. Yoon and Luttrell (1989) quantified the adhesion probability as the ratio of the area inscribed by the limiting radius (corresponding to the maximum incidence angle) to the area inscribed by the sum of bubble and particle radii. This adhesion probability is equal to $\sin^2\theta_{\text{inc}}$, θ_{inc} being the maximum incidence angle. Using the empirical relation for fluid streamlines as a function of bubble Reynolds number, Yoon and Luttrell (1989) derived the sliding time in terms of the incidence angle, assuming the particle inertial to be small. Equating the sliding and induction times for the maximum incidence case, the adhesion probability was obtained as:

$$P_a = \sin^2\left(2\arctan\left\{\exp\left[\frac{-(45 + 8Re_b^{0.72})u_{t,b}t_{\text{ind}}}{15d_b(d_b/d_s + 1)}\right]\right\}\right). \tag{38}$$

The following well-known relation for the induction time was used in this work:

$$t_{\text{ind}} = A_{\text{ind}} d_s^{B_{\text{ind}}}, \tag{39}$$

where $A_{\text{ind}} = 75/\theta_{CA}$ (θ_{CA} is the contact angle in degrees) and $B_{\text{ind}} = 0.6$, using the statistical fitting performed by Dai et al. (1999) and Koh and Schwarz (2006). Definition of the fitting parameter A is consistent with the fact that the induction time is short for hydrophobic surfaces (Wills and Finch, 2016). Although the effect of collectors has not been modelled here, they will affect the induction time directly through a change in the contact angle of the mineral surface.

Ideally the adhesion probability should also consider the extent of liberation of the mineral in the crushed ore. It is generally not economical to crush the ore to very fine particle size to liberate all mineral particles. Hence the partially-liberated ore has a lower probability of attaching to the bubbles as compared to a fully-liberated one. Welsby et al. (2010) measured the flotation rate as a function of particle size for different mean liberation values, noticing a clear trend. Jameson (2012) showed that the ratio of the rate constant for a partially liberated particle sample to a fully liberated sample was a unique function of liberation

independent of particle size, called the *liberation function*. Albijanic et al. (2011) saw a clear reduction in the adhesion time as the liberation of the mineral increased, through their experiments. There is currently no study that quantifies this effect of liberation on the adhesion probability and the effect of liberation therefore was not considered in the present model.

Stabilisation probability

Schulze (1993) proposed the stabilisation probability of the particle–bubble aggregates in a flotation pulp as:

$$P_s = 1 - \exp\left(1 - \frac{1}{Bo^*}\right). \tag{40}$$

Here Bo^* is the modified Bond number defined as the ratio of detachment to attachment forces. It is given as:

$$\begin{aligned} Bo^* = &\frac{d_s^2\left[(\rho_s - \rho_l)|\mathbf{g}| + 1.9\rho_s\varepsilon^{2/3}\left(\frac{d_s+d_b}{2}\right)^{-1/3}\right]}{|6\sigma\sin\left(\pi - \frac{\theta_{CA}}{2}\right)\sin\left(\pi + \frac{\theta_{CA}}{2}\right)|} \\ &+ \frac{1.5d_s\left(\frac{4\sigma}{d_b} - d_b\rho_l|\mathbf{g}|\right)\sin^2\left(\pi - \frac{\theta_{CA}}{2}\right)}{|6\sigma\sin\left(\pi - \frac{\theta_{CA}}{2}\right)\sin\left(\pi + \frac{\theta_{CA}}{2}\right)|}, \end{aligned} \tag{41}$$

where $\mathbf{g}$ is the acceleration due to gravity vector. In the above expression it is assumed that turbulent eddies of similar size as the bubble–particle aggregate cause detachment. Turbulence and capillary forces can be seen competing with each other in the above expression for the modified Bond number. This expression for stabilisation probability was used in the present flotation modelling framework.

2.3.3. Detachment rate

The particle detachment rate was given by:

$$\psi_d = Z_2 n_b^L P_d, \tag{42}$$

where Z_2 is the detachment frequency $(1/t)$, n_b^L is the concentration of loaded bubbles and P_d is the destabilisation probability. The detachment frequency due to the turbulent eddies was calculated using:

$$Z_2 = \frac{\sqrt{\tilde{C}}\varepsilon^{1/3}}{(d_s + d_b)^{1/3}}, \tag{43}$$

where the constant $\tilde{C}$ was taken to be equal to 2 (Bloom and Heindel, 2002, 2003; Koh and Schwarz, 2006). The concentration of loaded bubbles was calculated using $n_b^L = \beta_{\text{bub}} n_b^{\text{tot}}$. The destabilisation probability was calculated simply as $1 - P_s$.

2.3.4. Settling velocity of solids

Richardson and Zaki (1954) obtained the relation for the settling velocity of a suspension of uniform spherical particles as:

$$\mathbf{u}_{\text{settling}} = \frac{\mathbf{g}(\rho_s - \rho_l)d_s^2}{18\mu_l}\epsilon_s^{4.65}, \tag{44}$$

where the subscripts s and l refer to the solid and liquid, respectively. ϵ_s is the porosity in the solid-liquid mixture that can be written as:

$$\epsilon_s = 1 - n_f V_s. \tag{45}$$

Here, V_s is the volume of a solid particle. Equation (44) was used to calculate the settling velocity of free solids, which was superimposed on the liquid velocity field for getting the advection velocity in the free-solid scalar equation (Equation (29a)). The pulp phase models presented by Koh and Schwarz have also included the effect of the settling velocity of the particles, which can be verified from the settled unattached particles at the bottom of their tanks, as shown clearly in Koh and Schwarz (2008a, 2009). The settling velocity expression used by them, however, was not specified in their works. Neglecting the settling velocity would mean that the larger (and heavier) solid particles will also follow fluid streamlines like the lighter ones, which is physically incorrect. This equation however is only used for the better estimation of the advection term in the free-solid transport equation as no momentum equation for the free solids is solved in the present model.

2.3.5. Viscosity modification of the liquid phase

The collision between the solid particles in liquid phase manifests as an increased viscosity the of liquid. Einstein's equation, which relates the slurry viscosity μ_{slurry} to the solid volume fraction ϕ for spherical particles, is generally applicable to very dilute systems and the equation does not apply to higher solid concentrations. Krieger and Dougherty (1959) proposed an expression for the change in the viscosity of a fluid due to the presence of high concentration of rigid spherical particles as:

$$\mu_{\text{slurry}} = \mu_l\left(1 - \frac{\tilde{\phi}}{\tilde{\phi}_{\max}}\right)^{-[\mu]\tilde{\phi}_{\max}}, \tag{46}$$

where μ_l is the molecular viscosity of the fluid, $\tilde{\phi}$ is the solid volume fraction, $\tilde{\phi}_{\max}$ is the maximum packing fraction that the solid particles can achieve and $[\mu]$ is the intrinsic viscosity. Intrinsic viscosity is the limiting value of $(\mu_{\text{slurry}}/\mu_l - 1)/\tilde{\phi}$, which is equal to 2.5 using Einstein's equation. Merve Genc et al. (2012) used the values 2.5 and 0.74 for $[\mu]$ and $\tilde{\phi}_{\max}$ respectively, in Equation (46) for estimating the pulp viscosity in nickel sulphide flotation. Many other empirical and semi-empirical relations between μ_{slurry} and $\tilde{\phi}$ have been proposed (Shook and Roco, 1991). Equation (46) was used in the present work with the values 2.5 and 0.70 for $[\mu]$ and $\tilde{\phi}_{\max}$, respectively. Maximum solid packing fraction of 0.74 can be considered as a theoretical maximum (corresponding to hexagonally-packed spherical particles) that can be attained; real measured values are much smaller (order of 0.01 due to the gangue fibre mesh). The higher $\tilde{\phi}_{\max}$ value allows for the slurry to attain higher $\tilde{\phi}$ values and still keep flowing. Moreover, the flotation simulations demonstrated in this work are for a batch flotation system containing mineral particles only, therefore allowing higher values of $\tilde{\phi}_{\max}$. The solid volume fraction was calculated as

$\tilde{\phi} = 1 - \epsilon$ using Equation (45). Koh and Schwarz (2008a) have reported the use of modified viscosity in their pulp phase model. They used the Herschel Bulkley non-Newtonian model with the consistency and flow indices fitted for various pulp densities.

Since the viscosity modification is the only way to apply the effect of free solids on the liquid velocity field, this step is necessary. It is independent of the settling velocity modification in Equation (44), which does not impact liquid velocity as the free-solid transport equation does not modify liquid velocity in any way in the approach used in this paper. If a separate momentum equation was being solved for the free solids, viscosity modification of the liquid phase would impact solid velocity field and the Richardson and Zaki settling equation would not be needed. In the present model, the viscosity modification and Richardson and Zaki equation are used to independently apply the effect of free solids on the liquid velocity and the solid velocity, respectively.

Table 2 shows a comparison of the features of the present pulp phase simulation framework with previous studies.

2.4. Numerical discretisation

Fluidity is an open-source code that uses the finite element method (FEM) for solving coupled PDEs. The FEM was chosen over the finite difference method (FDM) as the finite element (FE) discretisation has been shown to naturally go well with the unstructured meshes (Wilson, 2009), which were used in the present work. Implementing higher-order discretisations is not straightforward in the finite volume method (FVM) and the FEM was chosen over it for reason that it provides a convenient way to increase the accuracy through an increase in the degree of the fitting polynomials. Galerkin FEM was used to discretise the pressure and velocity fields in this work. The FE shape functions can be obtained from continuous or discontinuous function spaces. Piecewise-linear discontinuous FE basis functions ($P1_{DG}$) were used to represent velocity in the momentum equation. The continuity equation (for pressure) used piecewise-quadratic continuous FE basis functions (P2). The $P1_{DG}$–P2 velocity–pressure pair ensured the LBB stability criterion (Cotter et al., 2009). See Figure 3 for a comparison between the different discretisations in one and two dimensions.

A node-centred CV discretisation was also used in certain cases (such as for phase volume fraction and PBE scalars) to ensure conservation. Control volume dual mesh was constructed on a P1 parent mesh (as shown in Figure 3) and piecewise-constant CV shape functions were used to discretise fields such as volume fractions, turbulence scalars, DQMOM scalars (in the PBE) and the solids concentrations. Therefore a hybrid FE–CV method was established for the solution of the coupled PDEs for modelling pulp hydrodynamics. See Bhutani et al. (2016) for more details on the description of the discretisation methods.

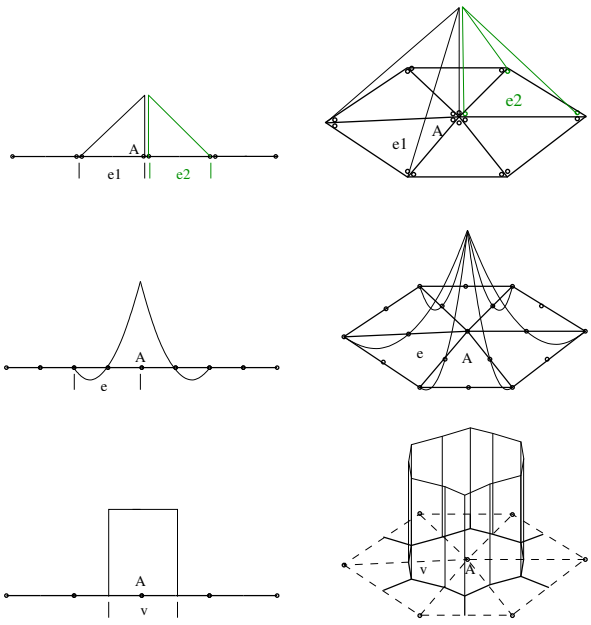

Figure 3: Elements and the corresponding shape functions on 1D (left) and 2D (right) FE meshes. (a) A pair of piecewise-linear discontinuous FE basis functions ($P1_{DG}$) along with the support nodes. (b) Piecewise-quadratic continuous FE basis functions (P2) along with the support nodes. (c) Control volume dual mesh on P1 parent mesh, and piecewise-constant CV shape functions for 1D and 2D are shown. The support for a basis function is the same as the control volume. Figure adapted from Wilson (2009).

Table 2
Comparison of the features of the present pulp phase simulation framework with previous studies.

Model feature	Present work	Koh et al. (2000)	Koh and Schwarz (2003)	Koh and Schwarz (2006)	Koh and Schwarz (2007)	Koh and Schwarz (2008a,b)	Karimi et al. (2014b)	Sarhan et al. (2016, 2018)
E–E model for gas and liquid phases	✓	✓	✓	✓	✓	✓	✓	✓
k–ε turbulence model for liquid phase	✓	✓	✓	✓	✓	✓	✓	✓
Polydisperse bubbles	✓	X	X	X	X	✓	X	✓
Polydisperse solids	✓	X	X	X	X	X	X	X
Settling velocity for free solids	✓	X	✓	✓	✓	✓	X	X
Viscosity modification of liquid phase due to solids	✓	X	X	X	X	✓	X	X
Transport equations for free and attached solids	✓	X	X	✓	✓	✓	✓	✓
Collision rate (bubble–solids)	✓	✓	✓	✓	✓	✓	✓	✓
Collision probability	✓	X	✓	✓	✓	✓	✓	✓
Adhesion probability	✓	X	X	✓	✓	✓	✓	✓
Stabilisation probability	✓	X	X	✓	✓	✓	✓	✓
Detachment rate (bubble–solids)	✓	X	X	✓	✓	✓	✓	✓
Solver	Fluidity	CFX	CFX	CFX	CFX	CFX	ANSYS Fluent	AVL-FIRE
Impeller modelling	X	✓	✓	✓	✓	✓	✓	X

2.5. Mesh adaptivity

Mesh adaptivity is the method of systematic mesh modification in a simulation, based on the physics of the problem, to predict the flow accurately as time progresses. Fluidity can generate fully-unstructured, non-homogeneous, anisotropic meshes adaptively for a given set of optimisation parameters. Considering the many equations that needed to be solved in the model in this work, it was imperative that an optimised mesh be considered for a tractable framework. Mesh adaptivity in Fluidity is a three-step process which starts with metric estimation, followed by mesh generation, and finally the interpolation of all fields on the new mesh.

The mesh metric is a Hessian based error metric which is a function of the curvature of the field to be adapted to and a user-defined interpolation bound. The mesh metric allows for an increase in the mesh resolution in the regions of strongly-varying fields, keeping the mesh in the other parts of the domain coarse. Different mesh metrics can be superposed in case the mesh needs to be adapted to more than one field (Pain et al., 2001). In the next step, the mesh is generated through a sequence of local topological operations (Piggott et al., 2009). Finally, the interpolation of meshes can be achieved using a consistent interpolation method or using a Galerkin projection method. Details on the description of mesh adaptivity and its implementation can be found in the previous work by the authors (Bhutani et al., 2016), the Fluidity manual (AMCG, 2015), Pain et al. (2001), and Piggott et al. (2009). Significant improvements in the solution efficiency have been reported through the use of mesh adaptivity in Fluidity in the past (Hiester et al., 2014; Jacobs et al., 2013)

In the present work the mesh was adapted for the air volume fraction, and the first weight and weighted-abscissa of the NDF. The application of adaptivity to the PBE fields was shown to improve the solution efficiency in the previous work by the authors (Bhutani et al., 2016). Details of the interpolation-error bound values used in this study are discussed in Section 4.

3. Problem description and simulation setup

Turbulence provides the necessary mixing needed in a flotation system to aid in the particle–bubble collision. This turbulence can either be generated using an impeller, such as in a flotation cell, or using gravity resulting in rising buoyant bubbles, such as in a flotation column. In this work a flotation column-like system was modelled using the present Fluidity framework to demonstrate its capabilities.

A rectangular column geometry, as shown in Figure 4, was used for the flotation simulations in this work. This geometry was inspired from the bubble column experiments of Díaz et al. (2008b), which was used as a validation problem in this work. Díaz's 'thin' bubble column measured 20 cm x 45 cm x 4 cm which was approximated with a 20 cm x 45 cm two-dimensional (2D) column in this work. Air was injected into this 2D column through a 2 cm sparger placed symmetrically at the base of the column, as shown in the figure. It was reasonable to approximate Díaz's thin experimental column with a 2D column as the z velocity component is much smaller than the x and y velocity components. The dependence of the fluid flow equations on the z-coordinate can be neglected if one is interested in estimating the flow at the centre z-plane. The acceptability of the above approximation was established through a good match with the bubble column experiments, as shown in Section 4.

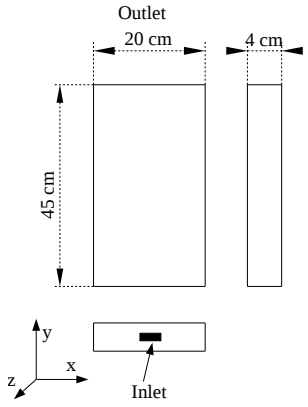

Figure 4: Experimental column of Díaz et al. (2008a) used in this work for model validation. Inlet dimentions are 1.8 cm × 0.6 cm.

Boundary conditions, initial conditions and the numerical and physical parameters used in the simulations are presented next. The values for all fields presented are the same for the bubble column validation problem and the flotation column problem, except for the solids equations which only appear in the flotation simulation.

The Schiller–Naumann (S–N) drag coefficient was used to model the interphase momentum interaction between the gas and liquid phases in this work. Gupta and Roy (2013) compared different drag models for a thin 2D bubble column geometry (similar to the one employed in the present work) with polydisperse bubbles and concluded that the Schiller–Naumann model was good enough to model drag in their bubble column. Although the S–N drag coefficient and similar models were typically developed for rigid single spheres in a dilute laminar flow, the application has been extended to polydisperse bubble population. This drag coefficient (and similar models) has (have) been used extensively over the years to model bubble-water drag successfully (Buwa and Ranade, 2002; Chen et al., 2005; Sanyal et al., 2005; Tabib et al., 2008; Silva et al., 2008; Buffo et al., 2016). The Schiller–Naumann drag coefficient is still popular in the minerals processing literature (Sarhan et al., 2017; Mwandawande et al., 2019; Wang et al., 2019) due to its good match with the standard drag curve (Clift et al., 1978). For the same reason this drag coefficient was employed for the present simulations even though the bubbles under consideration were 5 mm in diameter.

Table 3
BCs for the flow fields. n here denotes the normal coordinate. v denotes the y-component of the velocity.

Flow field	Inlet (sparger)	Walls	Outlet
Continuous phase velocity	v_c=0	no slip (weak)	v_c=0 (weak)
Gas velocity	v_d=0 (weak)	no slip (weak)	v_d=0 (weak)
Pressure	$\frac{\partial p}{\partial n} = 0$	$\frac{\partial p}{\partial n} = 0$	$p = 0$ at coordinate (0,0.45)
Air volume fraction	flux specified	no flux	$\frac{\partial \alpha_d}{\partial n} = 0$ with large absorption
Turbulent kinetic energy	$\frac{\partial k}{\partial n} = 0$	0	$\frac{\partial k}{\partial n} = 0$
Turbulent dissipation	$\frac{\partial \varepsilon}{\partial n} = 0$	$\frac{\partial \varepsilon}{\partial n} = 0$	$\frac{\partial \varepsilon}{\partial n} = 0$

3.1. Boundary conditions

Table 3 shows the boundary conditions for the velocity, pressure, volume fraction and turbulence fields that were used while modelling the bubble column and the flotation column. The superficial gas velocity (SGV) (also known as J_g) was used to calculate the inlet air flux using: gas flux $= \left(\frac{A_{\text{cross-section}}}{A_{\text{sparger}}}\right)$SGV. For the 2D column, $A_{\text{cross-section}}$ and A_{sparger} were equal to 20 cm and 2 cm, respectively. In order to extract the air at the outlet, a special absorption BC was applied for the air volume fraction. A large absorption term in the advection equation for the air volume fraction was implemented as:

$$\frac{\partial \alpha_d}{\partial t} + \nabla \cdot (\alpha_d \mathbf{u}_d) + \sigma_{\text{abs}} \alpha_d = 0, \tag{47}$$

where σ_{abs} is the absorption that was set equal to a very high value close to the outlet and zero otherwise:

$$\sigma_{\text{abs}} = \begin{cases} 10,000 & \text{if } y \geq 0.45, \\ 0 & \text{otherwise.} \end{cases} \tag{48}$$

The large absorption term, in conjunction with a fully-implicit time discretisation for the volume fraction transport equation, ensured that all the air reaching the outlet boundary was removed from the column. It is always tricky to "correctly" specify the outlet BC for the gas phase in a multiphase flow problem (Prosperetti and Tryggvason, 2007) and after trying various options, the above outlet BC was seen to give the expected result for the bubble column in this work. This boundary condition mimics the presence of a large absor ption zone at the outlet, which is more physical than the degassing BC typically employed in commercial codes.

For the PBE, since the number of quadrature points in the DQMOM assumption, N, was taken as 2, there were four unknowns (two weights and two weighted-abscissas) in the DQMOM transport equations. A no-flux BC was applied to the side walls of the column for these four PBE scalars. A homogeneous Neumann BC was applied at the outlet. At the inlet of the column, the incoming bubbles were assumed to be distributed normally with a standard deviation equal to 16% of the mean (Laakkonen et al., 2007; Buffo et al., 2013); this is based on the measurements by Laakkonen et al. (2007). With the definition of the SMD, the relation between the third moment and the bubble volume fraction (for spherical bubbles), and the above two assumptions about the inlet bubble distribution, the four unknown moments, and therefore the DQMOM scalars—w_1, w_2, ς_1 and ς_2—were calculated. The following system of coupled equations was solved for the inlet values of m_0, m_1, m_2 and m_3:

$$m_2 = m_0 \left[m_1^2 + (s.d.)^2\right], \tag{49a}$$

$$m_3 = m_0\, m_1 \left[m_1^2 + 3(s.d.)^2\right], \tag{49b}$$

$$s.d. = 0.16\, d_{32}, \tag{49c}$$

$$\frac{m_3}{m_2} = d_{32} \tag{49d}$$

and

$$m_3 = \alpha_d \left(\frac{6}{\pi}\right), \tag{49e}$$

where d_{32} and α_d are known. The moment inversion product–difference (PD) algorithm (Gordon, 1968) was then applied to obtain the weights and abscissas in the DQMOM approximation. At the inlet, a 5 mm average bubble diameter along with a volume fraction of 0.14 gave the four unknowns as w_1 =1.158 391 $\times 10^6$, w_2 =1.158 391 $\times 10^6$, ς_1 =4.560 935 $\times 10^3$, and ς_2=6.414 361 $\times 10^3$. The inlet volume fraction is a function of the sparger design and was assumed to be 14% gas in this work for the calculation of the PBE scalars. For the walls adjacent to the sparger (the 'lower walls'), a Dirichlet BC was applied for the four PBE scalars corresponding to an average bubble diameter of 1 mm and gas volume fraction of 1.0×10^{-7}, giving w_1 =1.034 281 $\times 10^2$, w_2 =1.034 281 $\times 10^2$, ς_1 =8.144 541 $\times 10^{-2}$, and ς_2=1.145 424 $\times 10^{-1}$. A no-flux BC at the lower walls led to the moment-set getting corrupted causing the scalars to become non-positive. The Dirichlet BC, however, ensured that the PBE scalars remained positive.

A no-flux BC was applied on all the boundaries for the free solids concentration field, whereas the attached solids were allowed to escape from the outlet with the absorption BC applied to them, as discussed in Equation (48).

3.2. Initial conditions

Zero velocity for the two phases was assumed initially with an air volume fraction of 1.0×10^{-7} everywhere. Since the

gas holdup (which is the percentage of gas in the column) increases as the air flows inside the column, the water volume goes down with time, but that decrease was not more than 5% for the maximum gas flow rate in this work. Initial k was taken as 1.0×10^{-7} m^{2}s^{-2} and ε as 1.0×10^{-7} m^{2}s^{-3}. The steady state result for the flow, however, was found to be independent of the initial values of k and ε.

The PBE scalars were calculated from an initial average bubble diameter of 1 mm and a gas volume fraction of 1.0×10^{-7} with the same two assumptions about the bubble number density function as discussed in the BCs. The initial PBE scalar values were therefore identical to the BCs used for the lower walls. The initial condition for the free and attached solids concentration fields are discussed in Section 4.2.

3.3. Physical and numerical parameters

Table 4
Physical parameters used in the simulations.

Physical parameter	**Value**
Continuous phase density ρ_c (kg m^{-3})	998.2
Dispersed phase density ρ_d (kg m^{-3})	1.205
Continuous phase dynamic viscosity μ_c (Pa · s)	0.001
Dispersed phase dynamic viscosity μ_c (Pa · s)	1.254×10^{-5}
Interfacial tension (air–water) σ (N m^{-1})	0.072
Solids density ρ_s (kg m^{-3})	2600
Solids contact angle	75°

The physical parameters chosen in the simulations are presented in Table 4. The constants C_1, C_2 and C_3 in the breakage frequency expression, Equation (24), were 6.0, 0.04 and 0.01, respectively, based on the work of Laakkonen et al. (2007). Buffo et al. (2013) also used the same values for these constants in their rectangular bubble column simulations. Binary breakage was assumed in the present work (same as Laakkonen et al. (2007)) and the value for the parameter C_4 in the daughter distribution function, Equation (25), was therefore taken as 2.0. The value for parameter C_5 in the coalescence frequency relation, Equation (27), was chosen to be 0.88. The value of C_6 in the coalescence efficiency, Equation (26), was 6.0×10^9, based on the work of Laakkonen et al. (2006) and Buffo et al. (2013).

An adaptive time step, with a strict limit on the maximum Courant number of 0.5, was used. Since the simulations were performed using adaptive-mesh simulations, the CFL criterion needed to be satisfied to ensure stability (due to the non-linear nature of the equations). A maximum of two Picard iterations were allowed per time step with a tolerance of 1.0×10^{-12} on the infinity norm of the fields.

The non-linear relaxation parameter θ_{nl} in the turbulence equations was taken to be 1, which allowed for an implicit discretisation of the source terms in the equations for k and ε, and in the expression for μ_T. The non-linear relaxation parameter for the velocities of the two phases was taken as 0.5.

3.4. Discretisations

The first-order upwind scheme was used for discretising the advection terms in all equations due to its conservative and monotonic nature, which ensured stability. The method also ensured that the moment-set obtained in the DQMOM was realisable, as discussed in Section 2.2. The Bassi–Rebay discretisation (Bassi and Rebay, 1997) was applied for the viscous terms in the momentum equations. A fully-implicit time discretisation scheme was used for the transient term in all PDEs. The conservative form of the advection equation was used for the air volume fraction and the PBE scalars to ensure mass conservation, but, as expected, it did not ensure strict boundedness (LeVeque, 2002; Wilson, 2009). Slight artificial diffusion had to be added to the volume fraction equation sometimes to stabilise the scheme.

To maintain positivity and stability, the production term was applied as a source in the k and ε equations whereas the destruction term, which is always negative, was applied as absorption (Patankar, 1980). Numerically it is always effective to have a large absorption coefficient as it supports convergence through under-relaxation. The implementation of the turbulence model was generalised for handling mixed shape functions (discontinuous shape functions for velocity and continuous for turbulence fields) for stability reasons.

The source terms in the PBE were evaluated at the mesh nodes instead of the mesh quadrature points to prevent spatial interpolation errors. These errors were particularly prominent for the current problem due to the discontinuity in the weights and the weighted-abscissas at the inlet at $t = 0$.

4. Results and discussions

In this section, the validation results for Díaz's bubble column (Díaz et al., 2008b) using the present modelling framework are presented first, followed by the flotation simulation results for the same geometry.

Adaptive meshes were used for all simulations in this study. The mesh was adapted to the air volume fraction (α_d), and the first abscissa (ξ_1) and the first weighted-abscissa (ς_1) of the bubble NDF. The corresponding interpolation-error bound values used for the three scalars were: 1.0×10^{-4}, 1.0×10^{-5} m and 100 m, respectively. The mesh was adapted after every 15 time steps. The maximum number of nodes was set to 20000, the minimum and maximum edge lengths being 0.001 m and 0.01 m, respectively. It is evident that the finest mesh was as small as the smallest bubble size in the column. Although it is ideal to have a mesh that allows at least a few dispersed particles per cell, in the present case it is the numerical accuracy that drove the limit on the mesh size. The mesh was adapted 4 times in an adapt cycle for a parallel simulation to compensate

for node locking (AMCG, 2015). The number of initial adapts was set to 6.

The minimum (adaptive) time step size in the highest gas flow rate (SGV=2.0 cm s^{-1}) simulation was 5.2×10^{-4} s. This was due to the CFL criterion with a limit of 0.5 for the maximum Courant number. This is a limitation that is inherent to the adaptive-mesh simulations (Jacobs, 2013). There is always a trade-off between the resolving power of the adaptive simulations and the time step size, as the non-linear fluid flow equations have to be linearised and need an upper bound for the Courant number. A value of the maximum Courant number above 0.6 destabilised the simulation in this case.

4.1. Model validation – bubble column

Bubble columns are two-phase reactors used in the chemical industry for gas–liquid reactions, owing to the high heat and mass transfer rates associated with them. A typical bubble column generally consists of a vertical cylindrical column filled with a liquid, through which the gas is bubbled. The gas bubbles, as they rise due to buoyancy, generate a plume that gets turbulent with height. The mixing caused by this plume-induced turbulence allows for the maximum interphase exchange (of mass, momentum and energy). As the gas flow rate is increased the bubble plume starts oscillating—known as plume oscillation. Bubble columns enjoy many advantages over their counterparts—the stirred reactors—which makes them a suitable candidate as industrial mixers.

The bubble column model in this work was simulated for a range of SGV values between 0.13 cm s^{-1} and 2.0 cm s^{-1}. It was noticed that a steady state was achieved in all simulations. A "cooling tower" flow pattern for water was developed in the column due to the flow of the bubble plume through it, generating the mixing required in such systems. The plume oscillation died as the simulation reached a steady state, and two recirculation zones for water were obtained as a result. This can be seen from the water streamlines plotted in Figure 5.

All bubble column simulation results are presented when the (transient) simulation achieved a steady state. Experiments have reported an oscillating plume (Pfleger et al., 1999; Buwa et al., 2006; Díaz et al., 2008b) and the bubble plume oscillation period (POP) was shown to decrease exponentially with superficial gas velocity. However, in the current simulation using the $k - \varepsilon$ turbulence model, steady state flow was obtained, which was similar to time-averaged flow profiles reported by Díaz et al. (2008a).

Many have claimed to model the unsteadiness in the flow using the $k - \varepsilon$ turbulence model coupled to the Eulerian–Eulerian approach (Díaz et al., 2008a; Pfleger et al., 1999). A similar 2D model was set up in ANSYS Fluent and compared to the present Fluidity model. The turbulent viscosity, which was very small to start with, gradually increased as the simulation progressed and kept increasing until everything became steady. Pfleger et al. (1999) and Sokolichin and Eigenberger (1999)

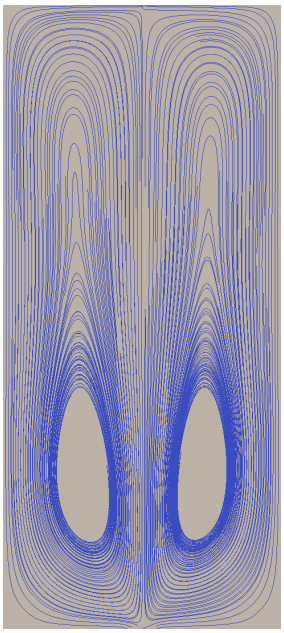

Figure 5: Predicted water streamlines at steady state for a SGV of 0.6 cm s^{-1}.

discussed this effect and concluded that 3D modelling of the columns is necessary to capture the plume oscillations; stating that the 2D models over-predict turbulence to a large extent (5–10 times higher turbulent viscosity) (Pfleger et al., 1999). As per them, the front and back walls in the column dampen the overall TKE allowing the 3D model to show unsteady behaviour. In order to check if the 2D modelling suppressed flow unsteadiness, a 3D column was simulated in Fluent for the exact same physical conditions and it produced similar results with a steady double recirculation zone for water. It was therefore decided to simulate the 2D bubble column as it has been found to model the mean-flow quantities reasonably (Pan et al., 1999) and can be used for model validation. Oey et al. (2003) discussed the effect of the discretisation scheme of the convective terms and suggested that lower-order diffusive schemes, such as the first-order upwind scheme, can cause enough numerical diffusion to suppress the transient terms in the results. However, the QUICK scheme was used with the 3D model in Fluent and as mentioned above, the unsteady plume could not be captured. Table 5 shows a comparison of the present numerical simulations with previous studies from literature in reference to the prediction of flow unsteadiness.

It is believed that an overpredicted eddy viscosity using the k-ε turbulence model could be responsible for suppressing the unsteadiness in the solution. In fact, the time-averaged nature of the RANS turbulence model could be causing the time averaging of the plumes in the flow. Although no plume oscillation was obtained in the numerical simulations in this study, the mean flow quantities obtained in a 2D simulation have been shown to give reasonable match with the experiments (Pan et al., 1999), and the same was used for validation here.

The strong circulation in the interior parts of column for the liquid phase was responsible for providing the shear leading

Table 5
Comparison of the present simulation behaviour with regards to the prediction of the plume oscillation with a few previous studies that used the k-ε model for modelling a rectangular bubble column.

	Model description	Plume oscillation predicted
Present work (Fluidity 2D)	E–E, unstructured mesh, 2D, $\Pi = 0$, $\mu_{T,d} = 0$, drag: Schiller and Naumann (1935), lift: no, VM force: no, Discretisations – FE for space, first-order time, $\Delta t \approx 0.0001$ s, BC – velocity: specified at inlet and outlet, vol frac: flux at inlet and absorption at outlet, walls: no-slip (weak).	no
Present work (Fluent 2D)	E–E, unstructured mesh, 2D, $\Pi = 0$, $\mu_{T,d} = 0$ evaluated from k-ε model for dispersed phase, drag: Schiller and Naumann (1935), lift: no, VM force: no, Discretisations – QUICK for space, first-order time, $\Delta t = 0.01$ s, BC – mass-flow inlet, outlet: degassing, walls: no-slip for liquid and free-slip for gas.	no
Present work (Fluent 3D)	E–E, structured mesh, 3D, $\Pi = 0$, $\mu_{T,d} = 0$ evaluated from k-ε model for dispersed phase, drag: Schiller and Naumann (1935), lift: no, VM force: no, Discretisations – QUICK for space, first-order time, $\Delta t = 0.005$ s, BC – mass-flow inlet, outlet: degassing, walls: no-slip.	no
Díaz et al. (2008a)	E–E, structured mesh, 3D, $\Pi = 0$, $\mu_{T,d}$ specified, drag: Grace et al. (1976), lift: yes, VM force: yes, CFX, Discretisations – second-order upwind for space, first-order time, $\Delta t = 0.025$ s, BC – velocity inlet, outlet: degassing, walls: no-slip for liquid and free-slip for gas.	yes
Buwa and Ranade (2002)	E–E, structured mesh, 3D, $\Pi = 0$, $\mu_{T,d}$ specified, drag: Tsuchiya et al. (1997) and Schiller and Naumann (1935), lift: yes, VM force: yes, Fluent, Discretisations – QUICK + SUPERBEE limiter for space, first-order time, $\Delta t = 0.01$ s, BC – velocity inlet, outlet: velocity specified, walls: no-slip.	yes
Pfleger et al. (1999)	E–E, structured mesh, 3D, $\Pi = 0$, $\mu_{T,d} = 0$, drag: constant, lift: no, VM force: no, CFX, Discretisations – higher-order TVD for space, first-order time, $\Delta t = 0.1$ s, BC – not specified in the paper.	yes

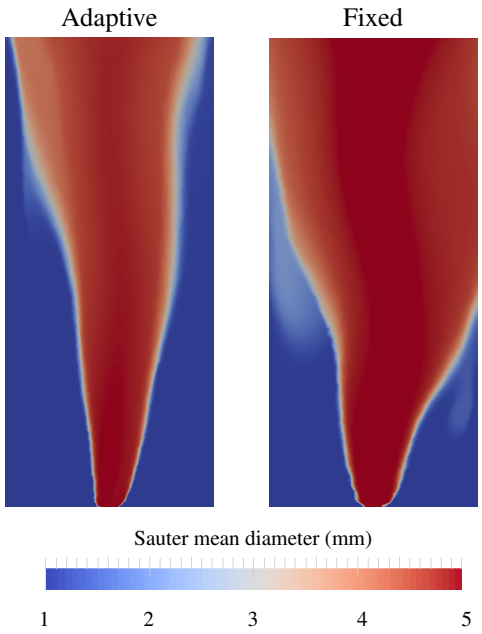

Figure 6: Sauter mean diameter at t = 9.6 s compared for an adaptive-mesh (≈ 19300 nodes) and a fixed-mesh (19347 nodes) for a SGV=0.6 cm s^{-1}.

to turbulence production in the present case. No wall model for turbulence was therefore used in this work as most of the production occurred in the interior of the column.

Figure 6 shows a comparison of the bubble SMD for fixed and adaptive meshes with approximately equal number of nodes for a SGV of 0.6 cm s^{-1}. It can be seen clearly that the adaptive mesh produced better resolved SMD field.

The contour plots of SMD and air volume fraction, and the corresponding adaptive meshes are shown for five time instances: 5 s, 8 s, 11 s, 15 s and 19 s for a SGV of 2.0 cm s^{-1} in Figure 7. It can be seen that the simulations converge to a steady state result and the plume oscillation is only visible in the initial stages. The anisotropy of the mesh is clearly visible with elongated elements close to the boundary of the gas plume. On an 8-core 2.30 GHz Intel Xeon machine, it took 10.5 days to run the SGV=2.0 cm s^{-1} simulation to 63 s. Strong scaling was performed for the bubble column problem and eight cores were found to be the optimum, beyond which the data bandwidth effect started dominating the processing power. Mesh adaptivity and parallelisation can be applied at the same time in Fluidity making it a highly desirable choice for the tractable modelling of multiphase polydisperse flows. The plots for air Sauter mean diameter are presented in Figure 8 at t=19 s . The variation in the bubble diameter is small in the plume for the present case.

To make a comparison of the local field predictions using the current polydisperse flow model, liquid flow field values were compared to the experiments of Pfleger et al. (1999). Their experiments measured the liquid vertical-velocity profile (using laser Doppler velocimetry) at three column heights for a SGV of 0.13 cm s^{-1} for a column of the same dimensions as this work. Simulations for the same SGV were carried out in the present work and the results were compared, as shown in Figure 9. It can be seen that the Fluidity model was able to predict the trend in liquid velocity reasonably. The effect of coalescence and breakage is negligible at such low flow rate and the polydisperse model takes that into account. Díaz et al. (2008a), on the other hand, had to revert to the monodisperse model for low gas flow rates as their polydisperse model was still predicting bubble breakage and coalescence and the results did not agree with the experiments. The agreement in Figure 9 is very good in the lower part of the column as the effect of the absorption outlet condition on the predicted flow parameters fades away in the lower reaches of the column. The under-prediction of the liquid y-velocities in the central zone of the column at h=0.25 m and 0.37 m can be attributed to the outlet boundary condition chosen in the present CFD model, along with the k-ε model potentially adding too much viscosity resulting in the underprediction of liquid velocities. The gas plume flows through the centre of the column and the choice of outlet BC has an effect on the prediction of the plume velocities and therefore the liquid velocities. An exaggerated drag force could also be attributed to the under-predicted liquid velocities in the central zone, however, a decent match close the column edges negates this hypothesis. The agreement can potentially be improved through a the inclusion of non-drag forces and the inclusion of bubble-induced turbulence model. However, since the aim of the present work was to demonstrate a tractable finite-element framework for the modelling of three-phase polydisperse flows, simplified models were chosen.

Gas holdup (or air volume fraction) is a very important global property that is used to characterise the flow regime in a bubble column. A larger gas holdup implies a larger residence time for the gas, implying better mixing. In order to make quantitative comparison of the gas holdup distribution, the experiments of Buwa et al. (2006) were used. They conducted experiments for the same column geometry as Díaz et al. (2008b) for a SGV of 0.73 cm s^{-1} and measured the local gas holdup in the column at a height of 0.37 m. Numerical simulation was carried out for the same SGV in Fluidity and the time-averaged results of Buwa et al. (2006) were compared to the numerical results obtained in the present work, as shown in Figure 10. Bell-shaped curve similar to the experiments are predicted by Fluidity, but the experiments correspond to a slightly more 'diffused' curve. Fluidity over-predicts the gas holdup at the column centre (x=0.1 m) by 20%, under-predicting around the column sides.

To validate the global gas holdup obtained using Fluidity simulations, the experiments of Díaz et al. (2008b) were used for comparisons. Díaz et al. (2008b) used the well-known manometric method to measure the static pressure difference across the column height to obtain the global gas holdup. Figure 11 shows the plot of the gas holdup obtained using the model in Fluidity, compared to the experiments of Díaz et al. (2008b). A good agreement between the experimental values and the numerical predictions can be seen in Figure 11. The expected linear trend in the increase of gas holdup with SGV is also captured to a good extent. At SGV values lower than 0.5 cm s^{-1}

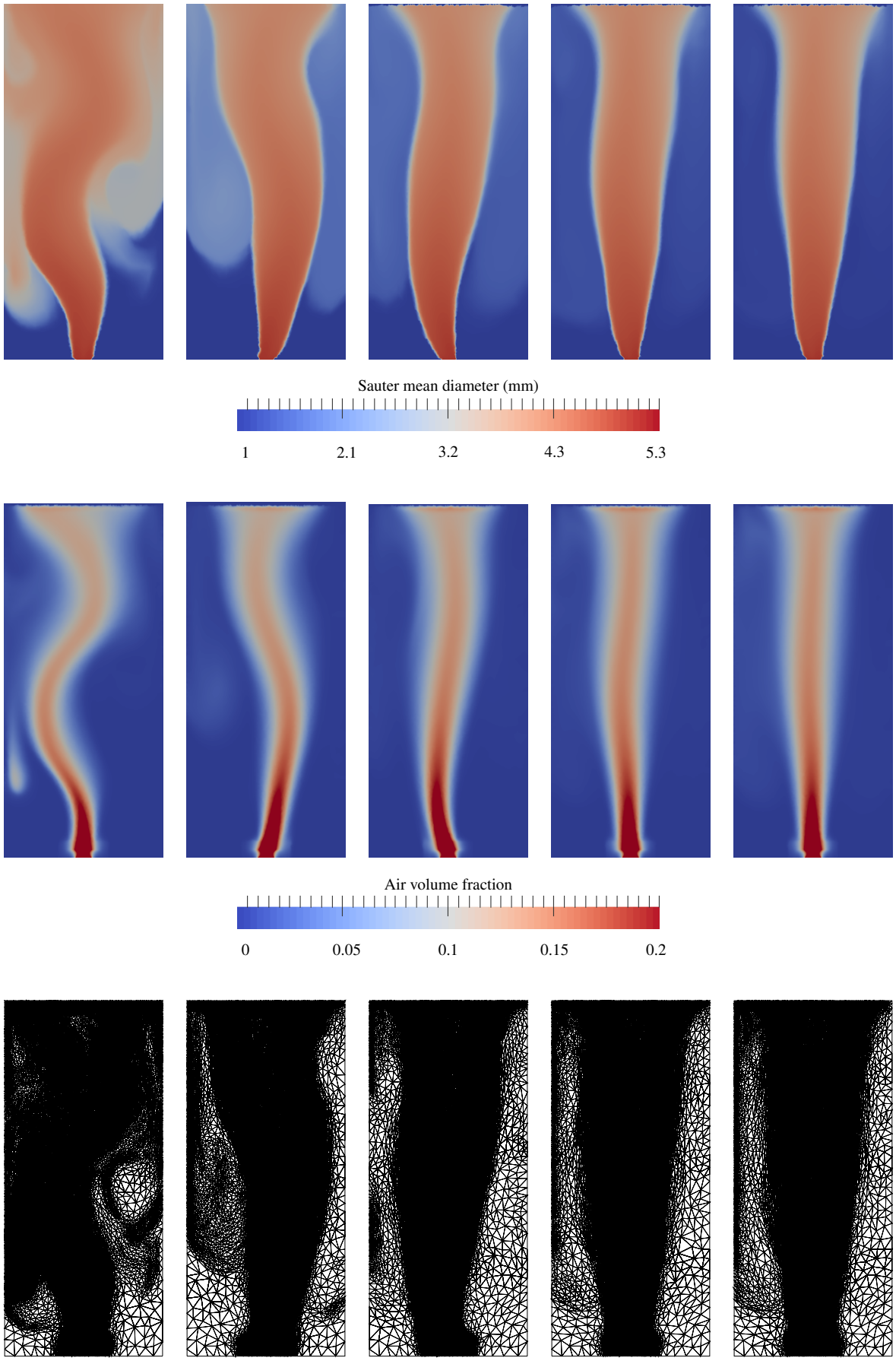

Figure 7: Contours of the bubble SMD and the air volume fraction plotted at five time instances (from left to right: t=5 s, 8 s, 11 s, 15 s and 19 s) for an adaptive-mesh simulation in Fluidity. The SGV was equal to 2.0 cm s^{-1}. Surface meshes are also shown.

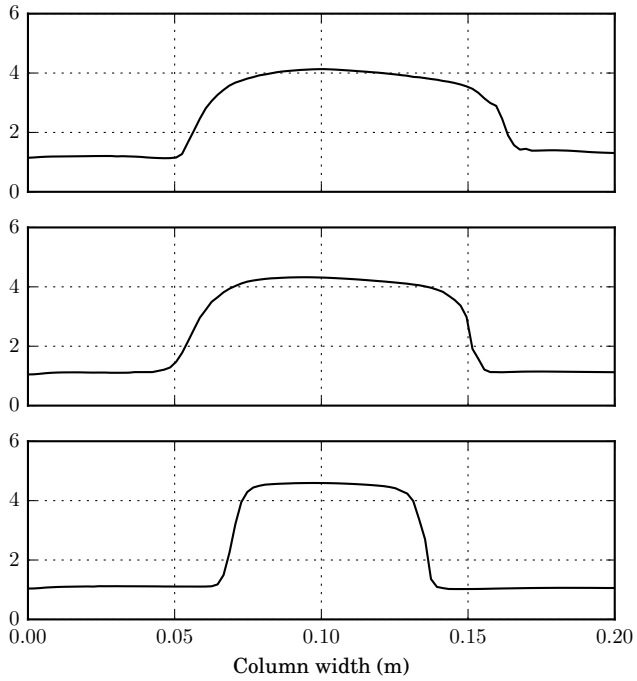

Figure 8: Comparison of the air Sauter mean diameter from Fluidity simulations at three column heights. From bottom to top: h = 0.13 m, 0.25 m and 0.37 m. SGV= 2.0 cm s^{-1}, t=19 s.

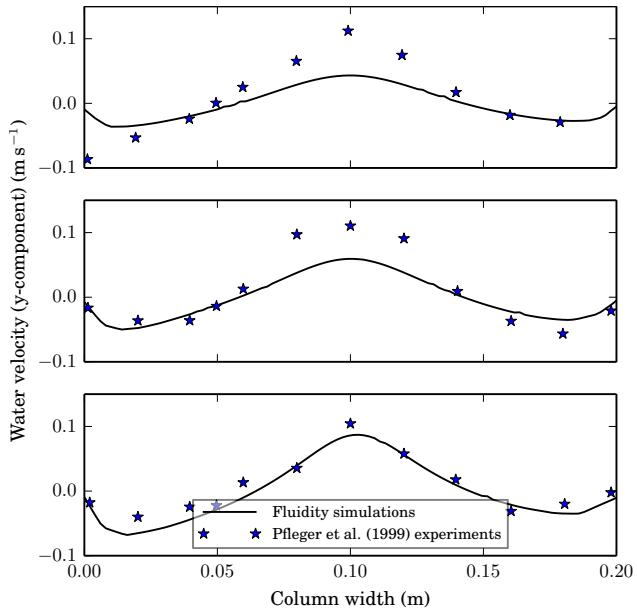

Figure 9: Comparison of the water vertical-velocity profiles between Fluidity simulations and the experiments performed by Pfleger et al. (1999) at three column heights. From bottom to top: h = 0.13 m, 0.25 m and 0.37 m. Steady state simulation results are compared with time-averaged experimental results. SGV= 0.13 cm s^{-1}.

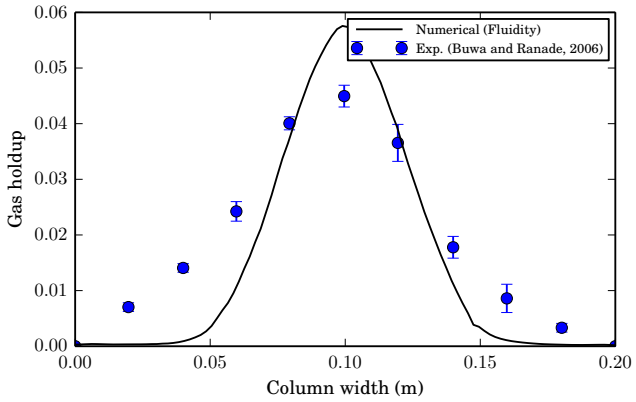

Figure 10: Gas holdup comparisons between the experiments of Buwa et al. (2006) and polydisperse Fluidity simulations. Values are plotted for a SGV of 0.73 cm s^{-1} at a height of 0.37 m in the column.

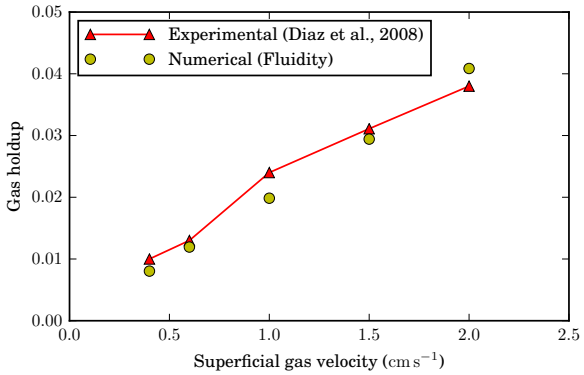

Figure 11: Gas holdup plotted as a function of the superficial gas velocity. The numerical results are compared to the experiments of Díaz et al. (2008b).

there is not much coalescence or breakage that occurs in the column and the model predicts a good gas holdup for these values of SGV. The kernels chosen in this work ensured that they did not predict any false coalescence or breakage at low turbulence values in the column at the lower values of the SGV.

The validation results presented in this section show a reasonable match with the experiments. The chosen models for the interphase drag force term, bubble breakage and coalescence kernels, and the inlet size distribution of bubbles were good enough to extend the bubble column model to a flotation column model through the introduction of solids.

4.2. Flotation column

The two-phase bubble column was allowed to attain a steady state after which the solid particles were introduced into it. Two simulation results are presented in this section, one for monodisperse solids and another for polydisperse solids. Previous pulp phase models by Koh and Schwarz (2007, 2008b) have considered monodisperse particles for simplicity. However, the feed entering the flotation process in reality is in the form of a particle size distribution and the model should be able to consider this polydispersity of the solids for an accurate modelling

of the overall process. For this reason a polydisperse solids simulation was run in this work and the results were compared to a monodisperse simulation to notice if the polydisperse modelling of solids has any effect on the rate of flotation. Both simulations were run for a superficial gas velocity of 1.0 cm s^{-1}. The monodisperse solids simulation consisted of 150 µm spherical solid particles with an initial concentration of 15% by volume (which is equal to 39% solids by mass for the present case). The corresponding initial condition for the free solids, n_f, was 8.25×10^{10} m^{-3}. All the particles were assumed to be free in the beginning and hence the initial concentration for the attached solids was taken as 1.0×10^{-7} m^{-3}. For the polydisperse simulation, three solid sizes were considered—50 µm, 150 µm and 250 µm. Initial concentration for each solid class was 5% by volume, which corresponded to an initial concentration of 7.5×10^{11} m^{-3}, 2.75×10^{10} m^{-3} and 6.0×10^{9} m^{-3} for the free solids of the three size classes, respectively.

4.2.1. Evolution of solid concentration

Figure 12 shows the total number of free particles of 150 µm size as a function of time in the polydisperse simulation. A linear decrease in the free particle population in the column was obtained in the 100 s simulation time. This decrease is due to the particles getting attached to bubbles and the loaded bubbles getting transported out of the batch flotation column. Figure 13 shows the total number of attached particles of 150 µm diameter in the polydisperse column as a function of time. It can be seen that the attached particles attain a steady state value in a very short time. This means that the rate of attachment becomes equal to the rate of transport of the attached particles out of the column. Koh and Schwarz (2006) also reported the number of attached particles becoming constant with time and the bubbles getting loaded very quickly in their pulp phase simulations for an impeller-driven cell. The rate of detachment was negligible for the simulation conditions in this work. Since the overall number of attached particles was constant and the detachment was negligible, the transport rate is what determined the rate of flotation here, similar to the findings of Koh and Schwarz (2006). Figure 14 shows the contours of the attached solids concentration in the column at steady state for the 150 µm particles in the polydisperse solids simulation. It can be seen that the attached particle concentration is higher near the inlet as compared to other sections in the column. The turbulent dissipation, which affects the collision rate, was also found to be high near the inlet of the column and may be the reason behind the increased attached particle concentration in that region.

4.2.2. Effect of polydispersity of solids

The particle volume fraction remaining in the column as a function of time is plotted in Figure 15 for the three solid sizes. Flotation rate, which is proportional to the negative of the slope of the curves, increases with particle size, as shown in the figure. Larger particles have a higher chance to come in contact with a bubble leading to higher collision rate. Although larger

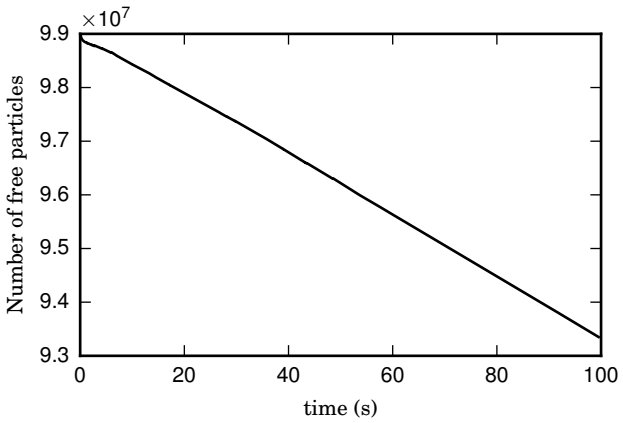

Figure 12: The total number of free particles (of 150 µm diameter) in the column as a function of time for the polydisperse solids simulation.

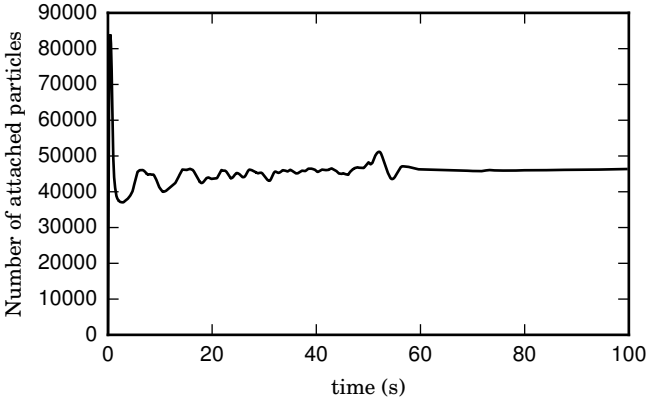

Figure 13: The total number of attached particles (of 150 µm diameter) in the column as a function of time for the polydisperse solids simulation.

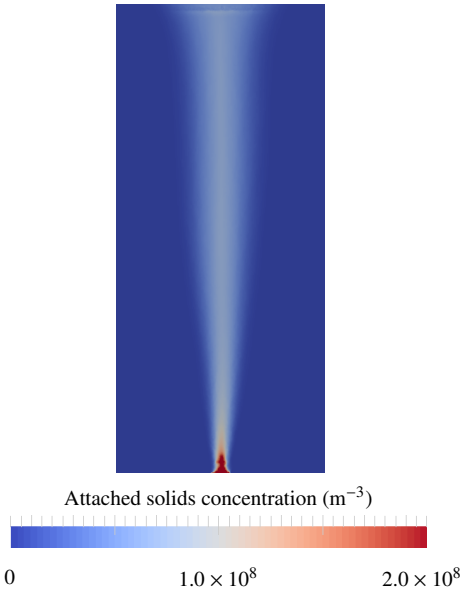

Figure 14: Steady state contours of the attached particles (of 150 µm size) in the polydisperse solids simulation.

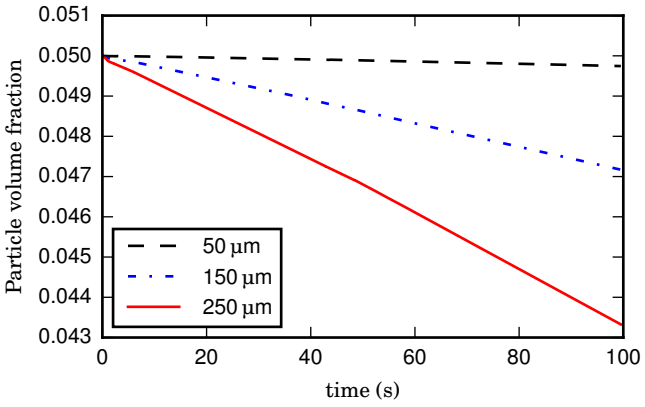

Figure 15: Particle volume fraction remaining in the flotation column plotted as a function of time for polydiperse mineral particles. Three particle diameter classes in the column were simulated with an initial volume fraction for each class equal to 0.05. J_g (or SGV) = 1.0 cm s^{-1}.

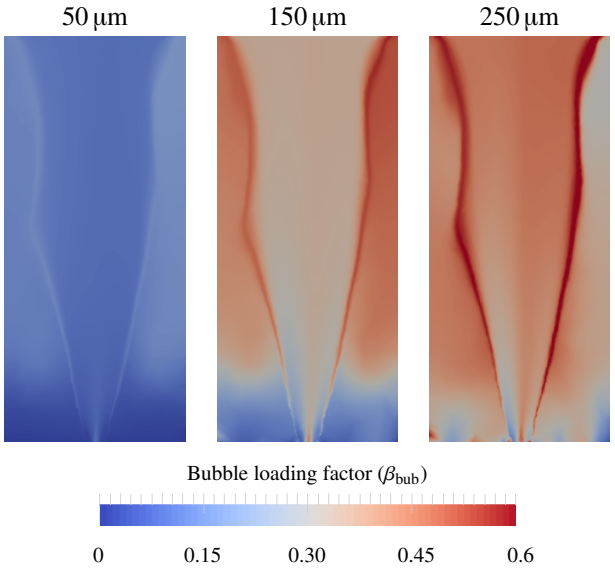

Figure 16: Contours of the bubble loading factor (β_{bub}) for the three solid sizes.

particles have higher destabilisation rates, the current expression for the probability of stabilisation and the current operating conditions resulted in a destabilisation rate close to zero. The bubble loading factor (β_{bub}) for the three solid sizes are compared in Figure 16. For the lower and intermediate particle sizes, the bubble loading is higher outside the central plume owing to the smaller number of bubbles in that region. The lower bubble loading corresponding to the smaller particle sizes supports the fact that attachment is more dominant for larger particles in this case.

Figure 17 shows a comparison of the total volume fraction of particles remaining in the column as a function of time for the monodisperse and the polydisperse simulations. The monodisperse solids simulation over-predicts the flotation rate as compared to the polydisperse simulation. Although the difference is only around 3.5% in the first 100 seconds, the linear trend

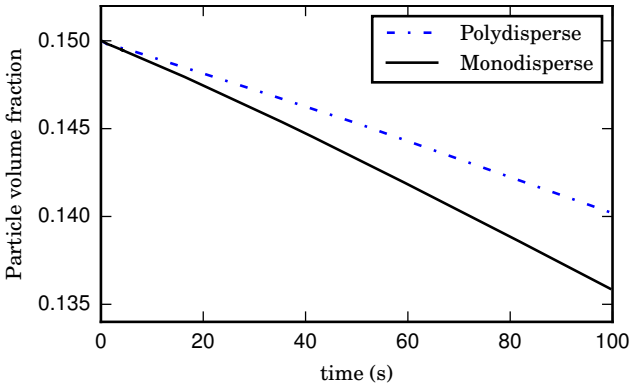

Figure 17: Comparison of the volume fraction of particles remaining in the column with time between monodisperse and polydisperse solids. The results have been compared for all particle sizes with a total initial solid volume fraction of 0.15 and a J_g of 1.0 cm s^{-1}.

could lead to an increasing over-prediction of the flotation rate with time. The overall higher flotation rate prediction in this case was due to the larger particles having a higher flotation rate overpowering the smallest ones. The over/underprediction of flotation rate for polydisperse system may depend on the nature of the flotation rates of the different particle sizes. This may imply that modelling the polydispersity of the solids is important for the correct prediction of flotation rate through CFD simulation of the pulp phase in a flotation column.

5. Conclusions

An efficient numerical framework for the modelling of the polydisperse pulp phase in froth flotation has been developed and presented in this paper. The absence of a comprehensive model for the pulp phase in the literature was the inspiration behind this work. The focus of this research was the modelling of the polydispersity of gas and solid phases and ensuring the tractability of the solution framework. Bubble polydispersity was modelled using the population balance equation that was implemented in Fluidity using DQMOM. Mesh adaptivity and code parallelisation features of Fluidity imparted tractability to the overall solution method. This study validated the polydisperse model solved for the bubbles (using the PBE) in a bubble column for a reasonable prediction of the flow hydrodynamics. Polydispersity of the solids was modelled for the first time by solving different equations for the solid classes. The effect of modelling the polydispersity of solids on the overall flotation rate prediction was also demonstrated.

Incompressible E–E momentum equations were solved for the gas and liquid phases, with a PBE to estimate the change in the bubble size due to breakage and coalescence in the pulp phase in a flotation column. A k-ε turbulence model was solved for the liquid phase, and the solids were modelled using scalar transport equations. The transport equations for free and attached particles were coupled through the attachment and detachment source terms. For the modelling of the pulp phase,

care was taken to modify the liquid viscosity in the momentum equations to account for the presence of free solids, and apply a settling velocity for the heavy particles in the free solids transport equation. The PBE for gas bubbles supplied bubble diameter and bubble concentration for attachment and detachment rate expressions in the solids transport equations. A quadrature-based moment method was used to solve the PBE for bubbles in a flotation system.

The Galerkin FEM was used to discretise the velocity and pressure fields in the momentum and pressure equations, respectively, and the $P1_{DG}$–P2 scheme was found to be the most stable for this purpose. For the other fields (such as PBE scalars, volume fraction, etc.), where conservation was required, a node-centred CV discretisation was employed. Therefore, a hybrid FE–CV method was found to be the most effective for simulating polydisperse multiphase flows. To the best of the authors' knowledge, this is the only framework that is capable of modelling the pulp zone using a hybrid FE–CV method.

The mesh was optimised as the solution progressed by generating fully-unstructured, non-homogeneous, anisotropic meshes adaptively for a given set of optimisation parameters—air volume fraction and PBE scalars. For the bubble column validation problem, adaptivity was shown to resolve the SMD field more accurately when compared to a similar fixed mesh. Mesh adaptivity was used for the first time in the modelling of the pulp phase in this paper. Moreover, Fluidity is the only framework that allows mesh adaptivity in the external coordinates of the PBE for modelling polydisperse flows.

The results from the 2D simulations performed using the polydisperse adaptive-mesh FE framework of Fluidity were compared to bubble column experiments in the literature. Although the steady-state results obtained for the flow profiles using Fluidity were not ideal due to the missing plume oscillations, they still showed a good match with the time-averaged local and global flow properties, as was seen for the validation comparisons for liquid velocity and gas holdup in the experiments by Díaz et al. (2008b), Buwa et al. (2006) and Pfleger et al. (1999).

The pulp phase was modelled for three solids classes and the overall flotation rate was compared to the monodisperse solids simulation. The flotation rate was found to increase with the particle size due to the probability of destabilisation being close to zero for the selected conditions; in reality the probability of destabilisation will play a role for very coarse particles. The monodisperse simulations were found to over-predict the flotation rate as compared to the polydisperse simulations. A difference of 3.5% in flotation recovery was noticed at a simulation time of 100 s for a J_g of $1.0\,\mathrm{cm\,s^{-1}}$. This error from neglecting the polydispersity of solids in the pulp phase is expected to add up in time and possibly lead to significant error in flotation recovery estimations. This research therefore confirmed the importance of modelling the polydispersity of dispersed phases in bubble and flotation columns for an accurate prediction of the flow and the flotation rate, respectively. It was also shown that a hybrid FE–CV framework can be successfully used for modelling such a complex system (the pulp phase), which had only been attempted in the past using the control volume codes (Koh and Schwarz, 2006, 2007, 2008b; Sarhan et al., 2016, 2018).

This modelling framework can be applied to simulate a variety of multiphase polydisperse problems in the process industries other than froth flotation. The framework can be used to test the effect of different physical models for dispersed phase interactions on the system hydrodynamics.

The framework can be enhanced by adding complexity in different fronts, which the authors plan to address in the future. These include the implementation of advanced turbulence models such as LES, interphase interaction models such as lift and virtual mass forces, various drag force correlations relevant to non-spherical bubbles, other improved models for bubble–particle detachment (Wang et al., 2016), the use of multivariate PBE for modelling the solids in the pulp phase (Bhutani and Brito-Parada, 2017), and the integration of the froth phase (Brito-Parada et al., 2012a,b) and pulp phase models.

Acknowledgements

We would like to thank Rio Tinto for funding this research. We would also like to thank the Applied Modelling and Computation Group (AMCG) at Imperial College London for their support with the open-source Fluidity code, as well as the Imperial College High Performance Computing (HPC) facility for providing with the computing resources to carry out this research.

References

Abrahamson, J., 1975. Collision rates of small particles in a vigorously turbulent fluid. Chemical Engineering Science 30 (11), 1371–1379.

Albijanic, B., Amini, E., Wightman, E., Ozdemir, O., Nguyen, A. V., Bradshaw, D. J., 2011. A relationship between the bubble–particle attachment time and the mineralogy of a copper–sulphide ore. Minerals Engineering 24 (12), 1335–1339.

AMCG, April 2015. Fluidity manual v4.1.12. Imperial College London. URL `http://dx.doi.org/10.6084/m9.figshare.1387713`

Andersson, R., Andersson, B., 2006. On the breakup of fluid particles in turbulent flows. AIChE journal 52 (6), 2020–2030.

Bannari, R., Kerdouss, F., Selma, B., Bannari, A., Proulx, P., 2008. Three-dimensional mathematical modeling of dispersed two-phase flow using class method of population balance in bubble columns. Computers and Chemical Engineering 32, 3224–3237.

Basavarajappa, M., Alopaeus, V., Yoon, R.-H., Miskovic, S., 2017. A high-order moment-conserving method of classes (HMMC) based population balance model for mechanical flotation cells. Minerals Engineering 108, 36–52.

Basavarajappa, M., Miskovic, S., 2015. Gas dispersion characteristics in lab-scale flotation cell using coupled CFD-PBM quadrature based moment method. In: 5th International Symposium on Computational Modelling. Falmouth, UK.

Bassi, F., Rebay, S., 1997. A high-order accurate discontinuous finite element method for the numerical solution of the compressible Navier–Stokes equations. Journal of Computational Physics 131 (2), 267–279.

Bhole, M. R., Joshi, J. B., Ramkrishna, D., 2008. CFD simulation of bubble columns incorporating population balance modeling. Chemical Engineering Science 63 (8), 2267–2282.

Bhutani, G., 2016. Numerical modelling of polydispersed flows using an adaptive-mesh finite element method with application to froth flotation. Ph.D. thesis, Imperial College London.

Bhutani, G., Brito-Parada, P. R., 2017. Analytical solution for a three-dimensional non-homogeneous bivariate population balance equation—a special case. International Journal of Multiphase Flow 89, 413–416.

Bhutani, G., Brito-Parada, P. R., Cilliers, J. J., 2016. Polydispersed flow modelling using population balances in an adaptive mesh finite element framework. Computers and Chemical Engineering 87, 208–225.

Bloom, F., Heindel, T. J., 1997. A theoretical model of flotation deinking efficiency. Journal of Colloid and Interface Science 190 (1), 182–197.

Bloom, F., Heindel, T. J., 2002. On the structure of collision and detachment frequencies in flotation models. Chemical Engineering Science 57 (13), 2467–2473.

Bloom, F., Heindel, T. J., 2003. Modeling flotation separation in a semi-batch process. Chemical Engineering Science 58 (2), 353–365.

Brito-Parada, P. R., Kramer, S. C., Wilson, C. R., Pain, C. C., Neethling, S. J., Cilliers, J. J., 2012a. A finite element formulation to model the flow of flotation foams. Chemical Engineering Science 69 (1), 279–286.

Brito-Parada, P. R., Neethling, S. J., Cilliers, J. J., 2012b. The advantages of using mesh adaptivity when modelling the drainage of liquid in froths. Minerals Engineering 33, 80–86.

Buffo, A., Alopaeus, V., 2016. Solution of bivariate population balance equations with high-order moment-conserving method of classes. Computers and Chemical Engineering 87, 111–124.

Buffo, A., Marchisio, D. L., Vanni, M., Renze, P., 2013. Simulation of polydisperse multiphase systems using population balances and example application to bubbly flows. Chemical Engineering Research and Design 91 (10), 1859–1875.

Buffo, A., Vanni, M., Renze, P., Marchisio, D., 2016. Empirical drag closure for polydisperse gas–liquid systems in bubbly flow regime: Bubble swarm and micro-scale turbulence. Chemical Engineering Research and Design 113, 284–303.

Buwa, V. V., Deo, D. S., Ranade, V. V., 2006. Eulerian–Lagrangian simulations of unsteady gas–liquid flows in bubble columns. International Journal of Multiphase Flow 32 (7), 864–885.

Buwa, V. V., Ranade, V. V., 2002. Dynamics of gas–liquid flow in a rectangular bubble column: Experiments and single/multi-group CFD simulations. Chemical Engineering Science 57 (22), 4715–4736.

Chen, P., Sanyal, J., Duduković, M. P., 2004. CFD modeling of bubble columns flows: implementation of population balance. Chemical Engineering Science 59, 5201–5207.

Chen, P., Sanyal, J., Duduković, M. P., 2005. Numerical simulation of bubble columns flows: Effect of different breakup and coalescence closures. Chemical Engineering Science 60 (4), 1085–1101.

Clift, R., Grace, J. R., Weber, M. E., 1978. Bubbles, drops, and particles. Dover Publications, Inc., Mineola, New York.

Cotter, C. J., Ham, D. A., Pain, C. C., 2009. A mixed discontinuous/continuous finite element pair for shallow-water ocean modelling. Ocean Modelling 26 (1), 86–90.

Coulaloglou, C. A., Tavlarides, L. L., 1977. Description of interaction processes in agitated liquid-liquid dispersions. Chemical Engineering Science 32 (11), 1289–1297.

Dai, Z., Fornasiero, D., Ralston, J., 1999. Particle–bubble attachment in mineral flotation. Journal of Colloid and Interface Science 217 (1), 70–76.

Desjardins, O., Fox, R. O., Villedieu, P., 2008. A quadrature-based moment method for dilute fluid-particle flows. Journal of Computational Physics 227 (4), 2514–2539.

Díaz, M. E., Iranzo, A., Cuadra, D., Barbero, R., Montes, F. J., Galán, M. A., 2008a. Numerical simulation of the gas–liquid flow in a laboratory scale bubble column: Influence of bubble size distribution and non-drag forces. Chemical Engineering Journal 139 (2), 363–379.

Díaz, M. E., Montes, F. J., Galán, M. A., 2008b. Experimental study of the transition between unsteady flow regimes in a partially aerated two-dimensional bubble column. Chemical Engineering and Processing: Process Intensification 47 (9), 1867–1876.

Evans, G. M., Doroodchi, E., Lane, G. L., Koh, P. T. L., Schwarz, M. P., 2008. Mixing and gas dispersion in mineral flotation cells. Chemical Engineering Research and Design 86 (12), 1350–1362.

Garcia-Zuñiga, H., 1935. La eficiencia de la flotación es una función exponencial del tiempo. Boletín Minero Sociedad Nacional de Minería 47, 83–86.

Gaudin, A. M., 1932. Flotation. McGraw-Hill, New York.

Gorain, B. K., Franzidis, J.-P., Manlapig, E. V., 1995. Studies on impeller type, impeller speed and air flow rate in an industrial scale flotation cell. Part 1: Effect on bubble size distribution. Minerals Engineering 8 (6), 615–635.

Gordon, R. G., 1968. Error bounds in equilibrium statistical mechanics. Journal of Mathematical Physics 9, 655.

Grace, J. R., Wairegi, T., Nguyen, T. H., 1976. Shapes and velocities of single drops and bubbles moving freely through immiscible liquids. Chemical Engineering Research and Design 54a, 167–173.

Grevskott, S., Sannæs, B. H., Duduković, M. P., Hjarbo, K. W., Svendsen, H. F., 1996. Liquid circulation, bubble size distributions, and solids movement in two- and three-phase bubble columns. Chemical Engineering Science 51 (10), 1703–1713.

Gupta, A., Roy, S., 2013. Euler–Euler simulation of bubbly flow in a rectangular bubble column: Experimental validation with Radioactive Particle Tracking. Chemical Engineering Journal 225, 818–836.

Hiester, H. R., Piggott, M. D., Farrell, P. E., Allison, P. A., 2014. Assessment of spurious mixing in adaptive mesh simulations of the two-dimensional lock-exchange. Ocean Modelling 73, 30–44.

Ishii, M., Hibiki, T., 2010. Thermo-fluid dynamics of two-phase flow, 2nd Edition. Springer, New York.

Jacobs, C. T., 2013. Modelling of multiphase flows on adaptive unstructured meshes with applications to the dynamics of volcanic ash plumes. Ph.D. thesis, Imperial College London.

Jacobs, C. T., Collins, G. S., Piggott, M. D., Kramer, S. C., Wilson, C. R. G., 2013. Multiphase flow modelling of volcanic ash particle settling in water using adaptive unstructured meshes. Geophysical Journal International 192 (2), 647–665.

Jameson, G. J., 2012. The effect of surface liberation and particle size on flotation rate constants. Minerals Engineering 36–38, 132–137.

Jones, W. P., Launder, B. E., 1973. The calculation of low-Reynolds-number phenomena with a two-equation model of turbulence. International Journal of Heat and Mass Transfer 16 (6), 1119–1130.

Karimi, M., Akdogan, G., Bradshaw, S. M., 2014a. A CFD-kinetic model for the flotation rate constant, Part II: Model validation. Minerals Engineering 69, 205–213.

Karimi, M., Akdogan, G., Bradshaw, S. M., 2014b. A computational fluid dynamics model for the flotation rate constant, Part I: Model development. Minerals Engineering 69, 214–222.

Koh, P. T. L., Manickam, M., Schwarz, M. P., 2000. CFD simulation of bubble-particle collisions in mineral flotation cells. Minerals Engineering 13 (14), 1455–1463.

Koh, P. T. L., Schwarz, M. P., 2003. CFD modelling of bubble–particle collision rates and efficiencies in a flotation cell. Minerals Engineering 16 (11), 1055–1059.

Koh, P. T. L., Schwarz, M. P., 2006. CFD modelling of bubble–particle attachments in flotation cells. Minerals Engineering 19 (6), 619–626.

Koh, P. T. L., Schwarz, M. P., 2007. CFD model of a self-aerating flotation cell. International Journal of Mineral Processing 85 (1), 16–24.

Koh, P. T. L., Schwarz, M. P., 2008a. Computational fluid dynamics modelling of slimes flotation at mt keith operations. Metallurgical Plant Design and Operating Strategies, MetPlant.

Koh, P. T. L., Schwarz, M. P., 2008b. Modelling attachment rates of multi-sized bubbles with particles in a flotation cell. Minerals Engineering 21 (12), 989–993.

Koh, P. T. L., Schwarz, M. P., 2009. CFD models of Microcel and Jameson flotation cells. In: Seventh International Conference on CFD in the Minerals and Process Industries. Melbourne, Australia.

Krieger, I. M., Dougherty, T. J., 1959. A mechanism for non-Newtonian flow in suspensions of rigid spheres. Transactions of The Society of Rheology 3, 137–152.

Laakkonen, M., Alopaeus, V., Aittamaa, J., 2006. Validation of bubble breakage, coalescence and mass transfer models for gas–liquid dispersion in agitated vessel. Chemical Engineering Science 61 (1), 218–228.

Laakkonen, M., Moilanen, P., Alopaeus, V., Aittamaa, J., 2007. Modelling local bubble size distributions in agitated vessels. Chemical Engineering Science 62 (3), 721–740.

Launder, B. E., Sharma, B. I., 1974. Application of the energy-dissipation model of turbulence to the calculation of flow near a spinning disc. Letters in Heat and Mass Transfer 1 (2), 131–137.

LeVeque, R. J., 2002. Finite volume methods for hyperbolic problems. Cam-

bridge University Press, Cambridge.
Luo, H., Svendsen, H. F., 1996. Theoretical model for drop and bubble breakup in turbulent dispersions. AIChE Journal 42 (5), 1225–1233.
Marchal, P., David, R., Klein, J. P., Villermaux, J., 1988. Crystallization and precipitation engineering—I. An efficient method for solving population balance in crystallization with agglomeration. Chemical Engineering Science 43 (1), 59–67.
Marchisio, D., Vigil, R., Fox, R., 2003a. Implementation of the quadrature method of moments in CFD codes for aggregation–breakage problems. Chemical Engineering Science 58 (15), 3337–3351.
Marchisio, D. L., Fox, R. O., 2005. Solution of population balance equations using the direct quadrature method of moments. Journal of Aerosol Science 36 (1), 43–73.
Marchisio, D. L., Fox, R. O., 2013. Computational models for polydisperse particulate and multiphase systems. Cambridge University Press, Cambridge.
Marchisio, D. L., Vigil, R. D., Fox, R. O., 2003b. Quadrature method of moments for aggregation–breakage processes. Journal of Colloid and Interface Science 258 (2), 322–334.
Mazzei, L., Marchisio, D. L., Lettieri, P., 2012. New quadrature-based moment method for the mixing of inert polydisperse fluidized powders in commercial CFD codes. AIChE Journal 58 (10), 3054–3069.
McGraw, R., 1997. Description of aerosol dynamics by the quadrature method of moments. Aerosol Science and Technology 27 (2), 255–265.
Merve Genc, A., Kilickaplan, I., Laskowski, J. S., 2012. Effect of pulp rheology on flotation of nickel sulphide ore with fibrous gangue particles. Canadian Metallurgical Quarterly 51 (4), 368–375.
Mwandawande, I., Akdogan, G., Bradshaw, S., Karimi, M., Snyders, N., 2019. Prediction of gas holdup in a column flotation cell using computational fluid dynamics (CFD). Journal of the Southern African Institute of Mining and Metallurgy 119 (1), 81–95.
Oey, R. S., Mudde, R. F., van den Akker, H. E. A., 2003. Sensitivity study on interfacial closure laws in two-fluid bubbly flow simulations. AIChE journal 49 (7), 1621–1636.
Ojima, S., Hayashi, K., Hosokawa, S., Tomiyama, A., 2014. Distributions of void fraction and liquid velocity in air–water bubble column. International Journal of Multiphase Flow 67, 111–121.
Olmos, E., Gentric, C., Midoux, N., 2003. Numerical description of flow regime transitions in bubble column reactors by a multiple gas phase model. Chemical Engineering Science 58 (10), 2113–2121.
Pain, C. C., Umpleby, A. P., de Oliveira, C. R. E., Goddard, A. J. H., 2001. Tetrahedral mesh optimisation and adaptivity for steady-state and transient finite element calculations. Computer Methods in Applied Mechanics and Engineering 190 (29), 3771–3796.
Pan, Y., Dudukovi ć, M. P., Chang, M., 1999. Dynamic simulation of bubbly flow in bubble columns. Chemical Engineering Science 54 (13), 2481–2489.
Patankar, S. V., 1980. Numerical heat transfer and fluid flow. CRC press, Boca Raton, Florida.
Petitti, M., Nasuti, A., Marchisio, D. L., Vanni, M., Baldi, G., Mancini, N., Podenzani, F., 2010. Bubble size distribution modeling in stirred gas–liquid reactors with QMOM augmented by a new correction algorithm. AIChE Journal 56 (1), 36–53.
Pfleger, D., Becker, S., 2001. Modelling and simulation of the dynamic flow behaviour in a bubble column. Chemical Engineering Science 56 (4), 1737–1747.
Pfleger, D., Gomes, S., Gilbert, N., Wagner, H.-G., 1999. Hydrodynamic simulations of laboratory scale bubble columns fundamental studies of the Eulerian–Eulerian modelling approach. Chemical Engineering Science 54 (21), 5091–5099.
Piggott, M. D., Farrell, P. E., Wilson, C. R., Gorman, G. J., Pain, C. C., 2009. Anisotropic mesh adaptivity for multi-scale ocean modelling. Philosophical Transactions of the Royal Society of London A: Mathematical, Physical and Engineering Sciences 367 (1907), 4591–4611.
Prince, M., Blanch, H., 1990. Bubble coalescence and break-up in air-sparged bubble columns. AIChE Journal 36 (10), 1485–1499.
Prosperetti, A., Tryggvason, G., 2007. Computational methods for multiphase flow. Cambridge University Press, Cambridge.
Ramkrishna, D., 2000. Population balances: Theory and applications to particulate systems in engineering. Academic press, San Diego.
Ranade, V. V., 1997. Modelling of turbulent flow in a bubble column reactor. Chemical Engineering Research and Design 75 (1), 14–23.
Richardson, J. F., Zaki, W. N., 1954. The sedimentation of a suspension of uniform spheres under conditions of viscous flow. Chemical Engineering Science 3 (2), 65–73.
Saffman, P. G., Turner, J. S., 1956. On the collision of drops in turbulent clouds. Journal of Fluid Mechanics 1 (1), 16–30.
Sanyal, J., Marchisio, D. L., Fox, R. O., Dhanasekharan, K., 2005. On the comparison between population balance models for CFD simulation of bubble columns. Industrial and Engineering Chemistry Research 44 (14), 5063–5072.
Sarhan, A. R., Naser, J., Brooks, G., 2016. CFD simulation on influence of suspended solid particles on bubbles' coalescence rate in flotation cell. International Journal of Mineral Processing 146, 54–64.
Sarhan, A. R., Naser, J., Brooks, G., 2017. CFD analysis of solid particles properties effect in three-phase flotation column. Separation and Purification Technology 185, 1–9.
Sarhan, A. R., Naser, J., Brooks, G., 2018. CFD model simulation of bubble surface area flux in flotation column reactor in presence of minerals. International Journal of Mining Science and Technology 28, 999–1007.
Sato, Y., Sekoguchi, K., 1975. Liquid velocity distribution in two-phase bubble flow. International Journal of Multiphase Flow 2 (1), 79–95.
Schiller, L., Naumann, Z., 1935. A drag coefficient correlation. Vdi Zeitung 77 (318), 51.
Schulze, H. J., 1993. Flotation as a heterocoagulation process: Possibilities of calculating the probability of flotation. In: Dobíaš, B. (Ed.), Coagulation and Flocculation: Theory and Applications. Vol. 47. Marcel Dekker, Inc., New York, Ch. 7, pp. 321–.
Schwarz, M. P., Koh, P. T. L., Verrelli, D. I., Feng, Y., 2016. Sequential multiscale modelling of mineral processing operations, with application to flotation cells. Minerals Engineering 90, 2–16.
Shook, C. A., Roco, M. C., 1991. Slurry flow: principles and practice. Butterworth-Heinemann, Oxford.
Silva, L. F. L. R., Damian, R. B., Lage, P. L. C., 2008. Implementation and analysis of numerical solution of the population balance equation in CFD packages. Computers and Chemical Engineering 32 (12), 2933–2945.
Smoluchowski, M. V., 1917. Grundriß der koagulationskinetik kolloider lösungen. Colloid and Polymer Science 21 (3), 98–104.
Sokolichin, A., Eigenberger, G., 1999. Applicability of the standard k–ε turbulence model to the dynamic simulation of bubble columns: Part I. Detailed numerical simulations. Chemical Engineering Science 54 (13–14), 2273–2284.
Sutherland, K. L., 1948. Physical chemistry of flotation. XI. Kinetics of the flotation process. The Journal of Physical Chemistry 52 (2), 394–425.
Tabib, M. V., Roy, S. A., Joshi, J. B., 2008. CFD simulation of bubble column—an analysis of interphase forces and turbulence models. Chemical Engineering Journal 139 (3), 589–614.
Tsuchiya, K., Furumoto, A., Fan, L.-S., Zhang, J., 1997. Suspension viscosity and bubble rise velocity in liquid-solid fluidized beds. Chemical Engineering Science 52 (18), 3053–3066.
Wang, G., Ge, L., Mitra, S., Evans, G. M., Joshi, J. B., Chen, S., 2018. A review of CFD modelling studies on the flotation process. Minerals Engineering 127, 153–177.
Wang, G., Nguyen, A. V., Mitra, S., Joshi, J. B., Jameson, G. J., Evans, G. M., 2016. A review of the mechanisms and models of bubble–particle detachment in froth flotation. Separation and Purification Technology 170, 155–172.
Wang, P., Cilliers, J. J., Neethling, S. J., Brito-Parada, P. R., 2019. The behavior of rising bubbles covered by particles. Chemical Engineering Journal 365, 111–120.
Welsby, S. D. D., Vianna, S. M. S. M., Franzidis, J.-P., 2010. Assigning physical significance to floatability components. International Journal of Mineral Processing 97 (1), 59–67.
Wills, B. A., Finch, J. A., 2016. Wills' mineral processing technology: An introduction to the practical aspects of ore treatment and mineral recovery, 8th Edition. Butterworth-Heinemann, Oxford.
Wilson, C., 2009. Modelling multiple-material flows on adaptive unstructured meshes. Ph.D. thesis, Imperial College London.
Yoon, R. H., Luttrell, G. H., 1989. The effect of bubble size on fine particle flotation. Mineral Procesing and Extractive Metallurgy Review 5, 101–122.
Zaruba, A., Krepper, E., Prasser, H.-M., Vanga, B. R., 2005. Experimental study on bubble motion in a rectangular bubble column using high-speed video observations. Flow Measurement and instrumentation 16 (5), 277–287.